The Abdus Salam
International Centre for Theoretical Physics

United Nations
Educational, Scientific and
Cultural Organization

IAEA
International Atomic Energy Agency

2240-25

Advanced School on Scaling Laws in Geophysics: Mechanical and Thermal Processes in Geodynamics

23 May - 3 June, 2011

An Introduction to Coupled Magma/Mantle Dynamics

Richard F. KATZ
University of Oxford, Dept. of Earth Sciences
Oxford
U.K.

Advanced School on Scaling Laws in Geophysics:
Mechanical and Thermal Processes in Geodynamics

Abdus Salam International Centre for Theoretical Physics, Trieste, Italy

An introduction to coupled magma/mantle dynamics

Richard F. Katz, University of Oxford
&
Marc Spiegelman, Columbia University/LDEO

May 30, 2011

Contents

1 Introduction

The mantle of the Earth was once entirely molten: a magma ocean. Over time, it solidified into the solid mantle that we know and love. However, plate-boundary volcanos are evidence of the fact that the mantle continues to melt. Why does this occur? Because the solid mantle convects, bring hotter mantle toward the surface, and colder mantle to depth. But this only explains the existence of melting. How does convection produce the spatial and temporal patterns of volcanism that we observe? How does it lead to the compositions of mid-ocean ridge basalts (MORB), ocean-island basalts (OIB), and subduction-zone lavas? What effect does melting have on the residual mantle, and how is this residual mantle distributed in space? What are the dynamic consequences of magmatism on mantle convection and plate tectonics? How has the extraction of melt affected the composition of the mantle (and the crust) over geological time? All of these questions go beyond the basic theory of mantle convection and require that we consider the physics and chemistry of magmatism.

In pursuit of this goal, we extend the equations governing mantle convection to include magmatism. In these lectures, we'll derive a set of equations that reduce to mantle convection (reviewed below) in the limit of no melting. In general, they also track the mechanics, energetics, and basic petrology of magmatism. As we shall see, they predict surprising behaviours that are not captured by the equations of mantle convection, and they introduce new length and time-scales to the problem at hand. They are physically complex, and challenging to solve, but this only adds to the excitement of their study. Consideration of the key scaling laws associated with the equations of coupled magma/mantle dynamics will be an essential but insufficient component of their analysis.

In the following notes, we move through the derivation of the governing equations, building complexity in increments, with interspersed studies of the scaling and solutions of the equations. This should build your intuition for the fluid mechanics and thermodynamics of of the system, which is essential for the interpretation of solutions to the full system of equations in the context of tectonic-scale models of plate-boundaries. The focus is on theory and models; observations are mentioned to motivate and validate models, but are otherwise not discussed in detail. References to the literature are kept to a minimum within the main body of the notes, and are provided in concentrated bursts at the end of each section. We begin with a very brief review of mantle convection.

1.1 Review of mantle convection

The simplest model for large-scale convection of the mantle is governed by a system of equations that you've already studied, and that are repeated here for reference:

$$\boldsymbol{\nabla} P = \boldsymbol{\nabla} \cdot \eta \left(\boldsymbol{\nabla} \mathbf{v} + \boldsymbol{\nabla} \mathbf{v}^T \right) + \rho \mathbf{g}, \tag{1}$$

$$\boldsymbol{\nabla} \cdot \mathbf{v} = 0, \tag{2}$$

$$\rho c_P \left(\frac{\partial T}{\partial t} + \boldsymbol{\nabla} \cdot \mathbf{v} T \right) = \boldsymbol{\nabla} \cdot k \boldsymbol{\nabla} T + \rho H, \tag{3}$$

plus conservation of composition, constitutive laws, etc.

The first of these is a statement of force-balance, known as Stokes' equation. It states that pressure gradients are balanced by viscous stresses and body forces. P is dynamic pressure, η is viscosity, $\mathbf{v}$ is the flow velocity of the mantle, ρ is the density, c_P is specific heat, T is temperature, k is thermal conductivity, and H is the rate of heat production per unit mass. The primary, dependent variables are $P, \mathbf{v}$, and T, while η, ρ, c_P, k, and H are parameters that may vary with the independent (space, time) or the dependent variables.

With a choice of coordinate system, and initial and boundary conditions, these equations can be solved, and the results can be interpreted in terms of the behaviour of the convecting mantle over the history of the Earth. You have seen this in earlier lectures, and we will not dwell on it here. The obvious deficiency of this model is that it does not account for the transfer of mass from the solid phase to the liquid phase (i.e. magma), and it does not account for the segregation of that liquid, and its ascent to magma chambers beneath volcanos. But these are essential features of the Earth system that we'd like to model!

2 Governing equations: mechanics

The minimal mechanical model for a two-phase system (liquid and solid) must be comprised of statements of conservation of mass and momentum for each of the two phases. Many authors have used different approaches to derive these equations, but the end results have been nearly identical. Here we loosely follow the approach taken by McKenzie [1984], noting modifications where relevant.

Our derivation will be motivated by the understanding that magma is distributed in a connected network of narrow pores between solid grains, as shown in Figure 1a. This is a sensible assumption because we know that the mantle is polymineralic, and that some minerals melt more easily than others. Magma is produced by *partial melting* of mantle rock, and on some length-scale that melting is volumetrically uniform. This length-scale must be much larger than the grain scale, but much smaller than the scale of variability of mantle properties such as temperature and bulk composition.

2.1 The representative volume element

We pose our derivation in terms of the contents of a representative volume element (RVE, Figure 1b), that contains a physical mixture of the two phases. Since we will be averaging physical properties over this element, we require that it contains a sufficient number of mantle grains that the average is "representative," i.e. not dependent on the details of which grains or pores happen to be within it. We also require that the RVE be small enough that mantle properties vary linearly (at most) across it.

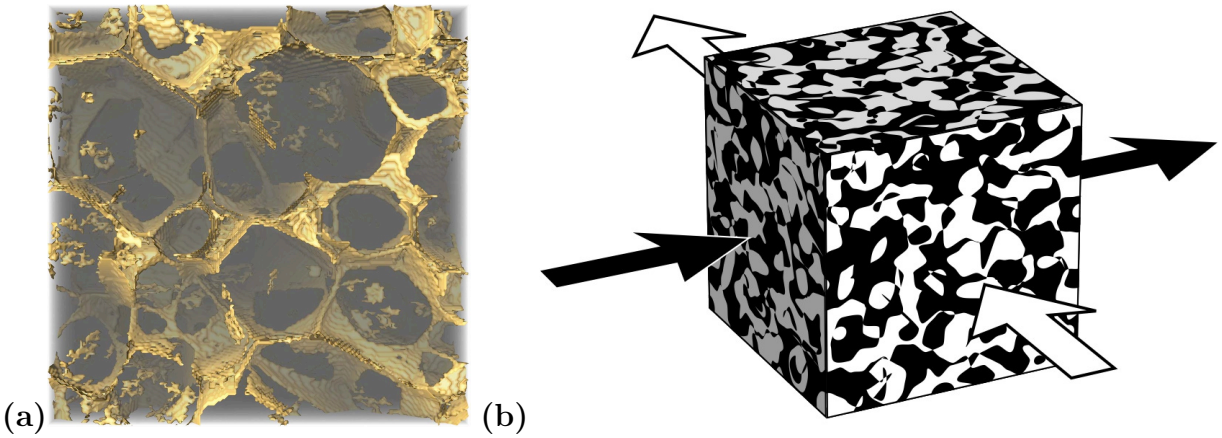

Figure 1: **(a)** 3-dimensional representation of the results of X-ray microtomography of an aggregate of olivine grains (transparent) and their melt-filled pore-space (gold) at a porosity of 20%. Note that the melt on grain triple-junctions forms an interconnected network of pores. (By Wenlu Zhu at the University of Maryland.) **(b)** Schematic representation of a representative volume element with magma $Q = 1$ and matrix $Q = 0$ represented by black and white sub-volumes, respectively. Figure from Bercovici et al. [2001a].

For some scalar property ψ within the RVE, we can write a general conservation equation for that scalar as follows:

$$\frac{\mathrm{d}}{\mathrm{d}t}\int_{\mathrm{RVE}} \psi \,\mathrm{d}V = -\int_{\partial\mathrm{RVE}} \psi \mathbf{v}\cdot\mathbf{dS} + \int_{\mathrm{RVE}} s \,\mathrm{d}V. \tag{4}$$

In this equation, $\int_{\mathrm{RVE}} \mathrm{d}V$ represents an integration over the volume of the RVE, and $\int_{\partial\mathrm{RVE}} \mathbf{dS}$ represents an integration over it's boundary, where $\mathbf{dS}$ is an outward-pointing normal vector of infinitesimal length. The first term in the equation is the rate of change of the amount of ψ in the RVE. It is equal to the rate at which ψ enters the RVE by advection, and the rate at which ψ is produced in the RVE by any possible sources; $\mathbf{v}$ is the material flow that carries ψ and s is the volumetric production rate of ψ.

Since we allow for only two phases, magma (liquid) and mantle (solid), the RVE must contain only those two phases, as shown in Figure 1b. We therefore define an *indicator function* $Q(\mathbf{x})$, which identifies the liquid and the solid phases within the RVE,

$$Q(\mathbf{x}) = \begin{cases} 1 & \text{if there is liquid at } \mathbf{x}, \\ 0 & \text{if there is solid at } \mathbf{x}. \end{cases} \tag{5}$$

This allows us to rigorously define the porosity ϕ as the volume fraction of the liquid phase within the RVE:

$$\phi = \frac{1}{V}\int_{\mathrm{RVE}} Q(\mathbf{x}) \,\mathrm{d}V. \tag{6}$$

This means that $1-\phi$ is the fraction of the solid phase within the RVE. The two must sum to unity.

2.2 Conservation of mass

Let's label the density of the liquid phase ρ_f (subscript f for fluid) and the density of the solid phase ρ_m (subscript m for matrix), and assume that these quantities may be considered constant over the RVE. This means that we can write the liquid mass as $\rho_f\phi$, and that the conservation equation for liquid mass is then written as

$$\frac{\mathrm{d}}{\mathrm{d}t}\int_{\mathrm{RVE}} \rho_f\phi \,\mathrm{d}V = -\int_{\partial\mathrm{RVE}} \rho_f\phi\mathbf{v}_f\cdot\mathbf{dS} + \int_{\mathrm{RVE}} \Gamma \,\mathrm{d}V, \tag{7}$$

where Γ is the melting rate, with units of mass/volume/time. Rearranging and using Gauss' theorem, we can write

$$\int_{\mathrm{RVE}} \left(\frac{\partial(\rho_f\phi)}{\partial t} + \boldsymbol{\nabla}\cdot\rho_f\phi\mathbf{v}_f\right)\mathrm{d}V = \int_{\mathrm{RVE}} \Gamma \,\mathrm{d}V,$$

and since the volume of the RVE is arbitrary (once we have made the appropriate continuum assumptions), we can discard the integrals and take the relationship to hold at any point in the continuum,

$$\boxed{\frac{\partial\rho_f\phi}{\partial t} + \boldsymbol{\nabla}\cdot\rho_f\phi\mathbf{v}_f = \Gamma.} \tag{8}$$

This equation states that changes in the fluid mass at a point are caused by the divergence of the fluid flux and the melting rate, at that point. Following an identical logic, the conservation of mass can be written

$$\boxed{\frac{\partial\rho_m(1-\phi)}{\partial t} + \boldsymbol{\nabla}\cdot\rho_m(1-\phi)\mathbf{v}_m = -\Gamma.} \tag{9}$$

Note that the RHS of the solid mass conservation differs from the fluid mass conservation by only a negative sign. Mass is transferred from the solid phase to the fluid phase during melting. Any physically consistent model of magma/mantle interaction must simultaneously satisfy these conservation of mass equations.

2.3 Conservation of momentum

Our fluid mechanical models requires statements of conservation of momentum which, as was the case with mantle convection, become statements of force balance, because we can neglect inertial terms (the Reynolds number is of order 10^{-8} or smaller).

Unlike mantle convection, however, there are two phases in this problem that can interact via an interphase force. We define the force $\mathbf{I}$ as the force exerted by the fluid phase on the matrix phase. By Newton's third law, the force of the matrix phase on the fluid phase is $-\mathbf{I}$. Using this definition, we can write a force balance equation for the matrix phase within our RVE as

$$\frac{\mathrm{d}}{\mathrm{d}t}\int_{\mathrm{RVE}} \rho_m(1-\phi)\mathbf{v}_m \,\mathrm{d}V + \int_{\partial\mathrm{RVE}} \rho_m(1-\phi)\mathbf{v}_m(1-\phi)\mathbf{v}_m \cdot \mathbf{dS} = \int_{\mathrm{RVE}} \rho_m(1-\phi)\mathbf{g}\,\mathrm{d}V + \int_{\mathrm{RVE}} \mathbf{I}\,\mathrm{d}V + \int_{\partial\mathrm{RVE}} (1-\phi)\boldsymbol{\sigma}^m \cdot \mathbf{dS}, \quad (10)$$

where $\mathbf{g}$ is the gravity vector and $\boldsymbol{\sigma}^m$ is the stress tensor within the solid phase. Neglecting the inertial terms on the LHS, applying Gauss' theorem, dropping integrals, and switching to indicial notation gives

$$-(1-\phi)\rho_m g\delta_{i3} + I_i + \frac{\partial}{\partial x_j}[(1-\phi)\sigma^m_{ij}] = 0, \quad (11)$$

where i is an index with values of 1, 2, and 3; δ_{ij} is the Kronecker delta, and the Einstein summation convention is implied. We have taken the z-direction to be parallel to the gravity vector, and pointing in the opposite direction such that $\mathbf{g}\cdot\hat{\mathbf{k}} = -g$.

Equation (11) is actually three equations, one for each Cartesian direction. For example, when $i = 1$ we are considering the x-direction; $\delta_{13} = 0$ so the first term drops out; the repeated j in the last term expands to a summation and we have

$$I_1 + \frac{\partial}{\partial x_1}[(1-\phi)\sigma^m_{11}] + \frac{\partial}{\partial x_2}[(1-\phi)\sigma^m_{12}] + \frac{\partial}{\partial x_3}[(1-\phi)\sigma^m_{13}] = 0.$$

The equation analogous to (11) for the magma is

$$-\phi\rho_f g\delta_{i3} - I_i + \frac{\partial}{\partial x_j}(\phi\sigma^f_{ij}) = 0, \quad (12)$$

where σ^f_{ij} is the stress tensor within the fluid phase. Note that the interaction force has the opposite sign from that in the equation for force balance in the solid.

For the force balance equations (11) and (12) to be useful, they must be expressed in terms of the matrix and magma velocities. To achieve this, we need to provide definitions of the interphase force and the stress tensors.

The interphase force $\mathbf{I}$ must be invariant to changes in inertial reference frame (i.e. it must be *Galilean invariant*). A variety of functions satisfy this relationship, but the simplest one is the *relative velocity* of the magma with respect to the matrix, $\mathbf{v}_f - \mathbf{v}_m$. Furthermore, it can be shown that $\mathbf{I}$ must include a term due to the pressure in the fluid, to take account for the

force which arises from a gradient in porosity. Incorporating these arguments, the interphase force can be written as

$$\mathbf{I} = C_1(\mathbf{v}_f - \mathbf{v}_m) - P_f \boldsymbol{\nabla}\phi, \tag{13}$$

where C_1 is a constant and P_f is the pressure in the magma. Some authors have included other terms in this equation (such as forces arising from surface tension), but these are of second-order importance in most physical contexts, and are not included here for simplicity. Inspired by Darcy's law of porous flow, we can choose

$$C_1 = \mu\phi^2/K, \tag{14}$$

where μ is the dynamic viscosity of the magma, and K is the permeability of the mantle matrix. Both of these can vary as a function of other problem variables; we will consider μ to be a constant, and K to be a function of porosity.

In deriving stress tensors, we will treat the magma as an incompressible fluid. The usual form for the stress tensor within an incompressible fluid is

$$\sigma_{ij} = -p\delta_{ij} + \mu\left(\frac{\partial v_i}{\partial x_j} + \frac{\partial v_j}{\partial x_i}\right). \tag{15}$$

Since we are averaging over a RVE that contains many magma-filled pores, and since those pores are oriented randomly between grains, we can assume that this averaging process leads to self-cancellation of the second-term on the RHS of equation (15) for the magma. We can then take $p = P_f$ and combine (15) with (13), (14), and (12) to obtain our force balance equation for the fluid,

$$\boxed{\phi(\mathbf{v}_f - \mathbf{v}_m) = -\frac{K}{\mu}\boldsymbol{\nabla}(P_f + \rho_f g z).} \tag{16}$$

When $\mathbf{v}_m = 0$, this equation reduces to Darcy's law. This equation states that segregation of magma from the mantle matrix is driven by pressure gradients and body forces in the fluid, and is modulated by permeability and magma viscosity.

The stress within the matrix phase requires a more complicated expression than (15). We expect that the grains of the matrix can compact to expel magma from the pores, or dilate to allow magma in. The rate at which this compaction occurs must be related to the difference in pressure between the matrix and the magma. We can represent the rate of compaction in terms of a continuum compressibility of the matrix phase with the understanding that when porosity is zero, the matrix phase must cease to be compressible. Hence we can write

$$P_f - P_m = \zeta \boldsymbol{\nabla}\cdot \mathbf{v}_m, \tag{17}$$

where ζ is a bulk viscosity that quantifies the resistance to compaction and dilation. ζ can be a function of temperature, porosity, or other problem variables and parameters.

The general form for the stress tensor of a compressible fluid is

$$\sigma_{ij} = -p\delta_{ij} + \zeta\delta_{ij}\frac{\partial v_k}{\partial x_k} + \eta\left(\frac{\partial v_i}{\partial x_j} + \frac{\partial v_j}{\partial x_i} - \frac{2}{3}\delta_{ij}\frac{\partial v_k}{\partial x_k}\right). \tag{18}$$

Substituting $p = P_f$ and $\mathbf{v} = \mathbf{v}_m$ into this equation gives the stress tensor for the matrix,

$$\sigma^m_{ij} = -P_f\delta_{ij} + \zeta\delta_{ij}\frac{\partial v^m_k}{\partial x_k} + \eta\left(\frac{\partial v^m_i}{\partial x_j} + \frac{\partial v^m_j}{\partial x_i} - \frac{2}{3}\delta_{ij}\frac{\partial v^m_k}{\partial x_k}\right). \tag{19}$$

To see that equation (19) is consistent with (17), we can compute the matrix pressure according to the formula $P = -\mathrm{Tr}(\boldsymbol{\sigma})/3$, where Tr indicates the trace of the tensor. Applying this to

(19) gives

$$\begin{aligned} P_m &= -\frac{1}{3}\left[-3P_f + 3\zeta\frac{\partial v_k^m}{\partial x_k} + \eta\left(2\frac{\partial v_i^m}{\partial x_i} - 2\frac{\partial v_k^m}{\partial x_k}\right)\right], \\ &= P_f - \zeta\boldsymbol{\nabla}\cdot\mathbf{v}_m. \end{aligned}$$

This shows that choosing (19) as the stress tensor for the matrix gives the compaction behaviour that we expect on physical grounds. It is important to note, however, that the matrix pressure includes a component of active deformation, and thus is not strictly an equilibrium (thermodynamic) pressure. Since the pressure difference between fluid and solid is generally small relative to the lithostatic pressure, this need not concern us. It is also important to note that this tensor represents stresses on the continuum, and thus cannot be used to compute the stresses within any single grain.

Combining equations (11), (13), (14), and (19) gives a force balance equation for the matrix in terms of flow velocities,

$$\begin{aligned} -(1-\phi)\rho_m g\delta_{i3} + \frac{\mu\phi^2}{K}(v_i^f - v_i^m) - P_f\frac{\partial\phi}{\partial x_i} \\ + \frac{\partial}{\partial x_i}\left\{(1-\phi)\left[-P_f\delta_{ij} + \zeta\delta_{ij}\frac{\partial v_k^m}{\partial x_k} + \eta\left(\frac{\partial v_i^m}{\partial x_j} + \frac{\partial v_j^m}{\partial x_i} - \frac{2}{3}\delta_{ij}\frac{\partial v_k^m}{\partial x_k}\right)\right]\right\} = 0. \end{aligned}$$

This equation can be simplified by substituting (16), expanding and combining pressure terms, and absorbing a factor of $(1-\phi)$ into ζ and η to give

$$\boxed{\boldsymbol{\nabla}P_f = \boldsymbol{\nabla}\cdot\eta\left(\boldsymbol{\nabla}\mathbf{v}_m + \boldsymbol{\nabla}\mathbf{v}_m^T\right) + \boldsymbol{\nabla}\left[\left(\zeta - \frac{2}{3}\eta\right)\boldsymbol{\nabla}\cdot\mathbf{v}_m\right] - \overline{\rho}g\hat{\mathbf{k}},} \tag{20}$$

where $\overline{\rho} = \rho_f\phi + \rho_m(1-\phi)$ is the phase-averaged density. This equation states that gradients in magma pressure are balanced by viscous shear stresses in the matrix, viscous compaction stresses in the matrix, and body forces on the phase-averaged density. It is closely related to Stokes' equation, except that being for a compressible (actually compactible) fluid, it contains compaction stresses.

For constant viscosity η and ζ, it can be shown that equation (20) reduces to

$$\boldsymbol{\nabla}P_f = -\eta\boldsymbol{\nabla}\times\boldsymbol{\nabla}\times\mathbf{v}_m + \left(\zeta + \frac{4}{3}\eta\right)\boldsymbol{\nabla}(\boldsymbol{\nabla}\cdot\mathbf{v}_m) - \overline{\rho}g\hat{\mathbf{k}}, \tag{21}$$

using the vector identity

$$\nabla^2\mathbf{V} = \boldsymbol{\nabla}(\boldsymbol{\nabla}\cdot\mathbf{V}) - \boldsymbol{\nabla}\times\boldsymbol{\nabla}\times\mathbf{V},$$

for any vector $\mathbf{V}$.

2.4 The Boussinesq approximation and a more convenient form

Equations (8), (9), (16), and (20) are a set of $2 + 2N_D$ equations in the same number of unknowns (N_D is the number of spatial dimensions). The principle unknowns are ϕ, P_f, $\mathbf{v}_m$, and $\mathbf{v}_f$. The equations are coupled (through the fluid pressure and the porosity) and non-linear (the permeability is typically taken as $K \propto \phi^n$ for small values of ϕ). They contain secondary variables ρ_m, ρ_f, Γ, μ, K, ζ, and η that must be specified using constitutive equations. It should be noted that equation (16) is an algebraic expression for $\mathbf{v}_f$ in terms of the other primary variables. With a solution for $\mathbf{v}_m$, P_f, and ϕ, equation (16) can be immediately applied to determine $\mathbf{v}_f$.

To put the governing equations into a form that is amenable to solution using analytical or numerical methods, it is helpful to make some simplifications. The first of these is the Boussinesq approximation, also used for mantle convection, which states that the phase densities may be approximated as being constant, except in buoyancy terms, where they are multiplied by g. We can also decompose the magma pressure into three parts as follows

$$P_f = P_L + \mathcal{P} + P, \tag{22}$$

where $P_L = -\rho_m g z$ is the lithostatic pressure (for z positive upward),

$$\mathcal{P} = (\zeta - 2\eta/3)\boldsymbol{\nabla}\cdot\mathbf{v}_m \tag{23}$$

is the compaction pressure, and P is the remaining, "dynamic" pressure. Substituting equation (22) and (23) into (20) gives

$$\boxed{\boldsymbol{\nabla}P = \boldsymbol{\nabla}\cdot\eta\left(\boldsymbol{\nabla}\mathbf{v}_m + \boldsymbol{\nabla}\mathbf{v}_m^T\right) + \phi\Delta\rho g\hat{\mathbf{k}},} \tag{24}$$

where $\Delta\rho = \rho_m - \rho_f$. This is the Stokes' equation and governs the large-scale shear flow of the mantle matrix.

To derive an equation that governs the small-scale compaction flow of the mantle matrix we apply the Boussinesq approximation and take the sum of equations (8) and (9) to obtain

$$\boldsymbol{\nabla}\cdot\phi(\mathbf{v}_f - \mathbf{v}_m) + \boldsymbol{\nabla}\cdot\mathbf{v}_m = \frac{\Delta\rho}{\rho_m\rho_f}\Gamma. \tag{25}$$

Then we take the divergence of (16) and substitute (25), (22), and (23) to obtain

$$\boxed{-\boldsymbol{\nabla}\cdot\frac{K}{\mu}\boldsymbol{\nabla}\mathcal{P} + \frac{\mathcal{P}}{\xi} = \boldsymbol{\nabla}\cdot\frac{K}{\mu}\boldsymbol{\nabla}(P - \Delta\rho g z) + \frac{\Delta\rho}{\rho_m\rho_f}\Gamma,} \tag{26}$$

where $\xi = \zeta - 2\eta/3$ is the compaction viscosity.

2.5 Relevant limits

There are two limits to these equations that help us to understand their nature. First, consider the limit of no porosity $\phi = 0$ and no melting $\Gamma = 0$. In that case, the conservation of mass for the solid (9) becomes the familiar continuity equation for an incompressible fluid

$$\frac{\partial\rho_m}{\partial t} + \boldsymbol{\nabla}\cdot\rho_m\mathbf{v}_m = 0;$$

the conservation of mass and momentum equations for the liquid phase disappear, because there is no liquid phase present, and the conservation of momentum equation for the solid phase becomes

$$\boldsymbol{\nabla}P_m = \boldsymbol{\nabla}\cdot\eta\left(\boldsymbol{\nabla}\mathbf{v}_m + \boldsymbol{\nabla}\mathbf{v}_m^T\right) - \rho_m\hat{\mathbf{k}}.$$

With the Boussinesq assumption, this system of two equations is exactly what we have used as a model for mantle convection (equations (1) and (2)). So in the limit of zero porosity, coupled magma/mantle dynamics reduces to just mantle dynamics!

The other limit to consider is when the mantle is partially molten, but entirely rigid, with porosity that is constant in space and time (and hence no melting). Then $\mathbf{v}_m = \mathbf{0}$, $\Gamma = 0$, and the conservation of mass equations become

$$\frac{\partial\rho_f}{\partial t} + \boldsymbol{\nabla}\cdot\rho_f\mathbf{v}_f = 0;$$

The conservation of mass and momentum equations for the solid phase are solved trivally if the solid density is constant, and the conservation of momentum for the liquid is

$$\phi \mathbf{v}_f = -\frac{K}{\mu}\left(\boldsymbol{\nabla} P_f + \rho_f g \hat{\mathbf{k}}\right).$$

This is simply porous flow in a uniform, saturated medium!

2.6 Constitutive equations

To close the system of mechanical equations, we require constitutive equations for ρ_m, ρ_f, μ, K, Γ, ζ, and η. Depending on the problem that we wish to solve, or the physics that we wish to capture with our model, these relations can take a variety of forms. In this section, we encounter a typical set of choices. As with mantle convection, however, some interesting research lies in generalising these constitutive relations to capture a more detailed model of the physical system.

In most applications of magma dynamics, the Boussinesq approximation is extended to assume that the phase densities are both equal to a mean density ρ, and that the density difference $\Delta\rho$ is neglected, except in buoyancy terms, where it is considered to be constant. This means that the last term in the compaction equation, representing volume change due to melting, is neglected.

Furthermore, all published works on magma dynamics take the magma viscosity μ to be a constant, although in reality it must vary with temperature and composition, at the least. We will consider μ a constant throughout these notes.

Variation of permeability with porosity is an essential aspect of magma dynamics. The ease of segregation must depend on the mean pore-size, and this must vary with several factors. In the limit of small porosity ($\phi \ll 1$), the permeability is typically written as

$$K(\phi) = \frac{d^2}{c}\phi^n, \tag{27}$$

where d is the grain size, and c and n are dimensionless constants that depend on the microscopic geometry of grains and pores. Inspection of equation (16) indicates that to ensure that the segregation velocity increases with increasing porosity, we require that $n > 1$. A simple geometric model of flow through tubes at the edges of a lattice of cubic grains predicts that $n = 2$; flow in sheets parallel to the faces of cubic grains predicts $n = 3$; experimental studies have typically obtained values of n between these limits. Since the mechanical models we have developed so far contain no rule for the evolution of grain-size, we will prescribe it as a constant below.

The melting rate Γ is another key parameter in the equations; underlying it is the entire field of mantle petrology, which includes thermodynamic theories of enormous complexity (and that is just to describe the *equilibrium* thermodynamics). For the applications considered here, we will look for simple parameterisations of the petrology that capture the essential features[1], but neglect most of the details. For example, to describe adiabatic melting, we could prescribe a closure of the form

$$\Gamma = -(\mathbf{v}_m \cdot \hat{\mathbf{g}}) \left.\frac{\mathrm{d}F}{\mathrm{d}z}\right|_S, \tag{28}$$

where F is the melt fraction, $\hat{\mathbf{g}}$ is a unit vector pointing in the direction of gravity, and $\mathrm{d}F/\mathrm{d}z|_S$ is the adiabatic productivity of decompression melting. As it turns out, this is not a bad

[1] We will definite "essential" on a case-by-case basis, depending on the physics and phenomena that we seek to model.

approximation for decompression melting, but it misses other forms of melting, as well as any melting or freezing due to changes in temperature. It is sometimes useful to take $\Gamma = 0$ and examine the behaviour of solutions with a fixed total porosity.

The bulk ζ and shear η viscosities of the two-phase aggregate are also essential parameters and play an important role in solutions of various problems. In general, they vary with other variables including temperature, composition, porosity, and strain-rate. Much can be learned about the governing equations by assuming that the viscosities are constant, however. In the notes below, we will introduce the form of the closure relations for bulk and shear viscosity as we develop applications and solutions of the governing equations.

2.7 Non-dimensionalisation and scaling

The last step, before we begin to examine solutions to the equations of mass and momentum conservation, is to choose appropriate scales to non-dimensionalise them. There are a variety of approaches to this task, and different physical problems might motivate us to take choose among these. Here we consider a standard choice that brings out some interesting aspects of the physics.

We have several aims in non-dimensionalising the equations. The first is to reduce the number of independent parameters to the minimum set, so that we can clearly see the controls on the solution; non-dimensionalising the equations will result in a set of non-dimensional parameters (such as the Reynolds number). The second aim is to better understand what terms in the equations (and hence what physics) is important in different physical contexts. This is similar to searching for scaling laws: we seek information about what terms represent the dominant balance in solutions to the equations. The third aim is to renormalise the variables in the problem so that they are all of order unity. This aids in developing accurate numerical solvers for the governing equations.

To non-dimensionalise, we take the approach of guessing approximate scales for some variables, based on our physical intuition and/or published observations, and then using these guesses to derive characteristic scales for other variables. To start, let's assume a characteristic value for the porosity of a partially molten region of the mantle, $\phi_0 \ll 1$. We can renormalise the porosity[2]

$$\phi = \phi_0 \phi', \tag{29}$$

where ϕ' is a rescaled porosity variable that equals one when $\phi = \phi_0$. This motivates us to scale the permeability as

$$K = \frac{d^2 \phi_0^n}{c} \phi'^n = K_0 \phi'^n, \tag{30}$$

where $K_0 = d^2 \phi_0^n / c$ is the characteristic permeability. Examining equation (16) and guessing that $\mathbf{v}_m$ and P_f are small relative to $\mathbf{v}_f$ and $\Delta\rho g$, we can guess that magmatic segregation is mainly driven by the body-force difference between the magma and the solid, and propose a scaling for velocity as follows

$$\mathbf{v}_f = \frac{K_0 \Delta\rho g}{\mu \phi_0} \mathbf{v}_f' = w_0 \mathbf{v}_f', \tag{31}$$

where $\mathbf{v}_f'$ is our rescaled, dimensionless fluid velocity. The matrix velocity will scale with the product $\phi_0 w_0$ since we expect it to be much smaller than the magmatic velocity.

It is clear that we also need to choose a characteristic length-scale and time-scale for our non-dimensionalisation. Instead of guessing at an appropriate length-scale, we'll represent it as δ and determine a value for δ later. The characteristic time-scale τ can then be taken as

[2]Since the porosity is already dimensionless, this is not "non-dimensionalisation" *per se*, but has the same intent and effect.

the time for magma travelling at speed w_0 to travel a distance δ. The characteristic scale for viscosity can be taken as $\zeta_0 + 4\eta_0/3$, motivated by equation (21). Lacking good information on the melting rate, we'll scale it by Γ_0. The pressure will scale with $P_0 = \Delta\rho g\delta$, which is motivated by our choice of buoyancy as the key driving force for magmatic segregation. To summarise, we have agreed that

$$[\phi] \sim \phi_0, \qquad [K] \sim K_0, \qquad [\mathbf{v}_f, \mathbf{v}_m] \sim w_0, \qquad [\mathbf{x}] \sim \delta, \tag{32a}$$

$$[t] \sim \delta/w_0, \qquad [P, \mathcal{P}] \sim \Delta\rho g\delta, \qquad [\eta, \zeta, \xi] \sim \zeta_0 + \frac{4}{3}\eta_0 \qquad [\Gamma] \sim \Gamma_0. \tag{32b}$$

Each of these states that the quantity in brackets has the characteristic scale given on the RHS.

Applying the extension of the Boussinesq approximation to equation (26), substituting appropriate scales from (32), and immediately dropping primes from non-dimensional variables gives

$$-\boldsymbol{\nabla}\cdot(\phi^n\boldsymbol{\nabla}\mathcal{P}) + \frac{\delta^2\mu}{(\zeta_0 + 4\eta_0/3)K_0}\frac{\mathcal{P}}{\xi} = \boldsymbol{\nabla}\cdot\left[\phi^n(\boldsymbol{\nabla}P - \hat{\mathbf{k}})\right], \tag{33}$$

where we can immediately recognise the dimensionless group $\delta^2\mu/[(\zeta_0+4\eta_0/3)K_0]$. This suggests that we choose

$$\delta = \sqrt{\frac{(\zeta_0 + 4\eta_0/3)K_0}{\mu}}, \tag{34}$$

which is a length that we shall call the *compaction length*. In the notes below, we shall see that the compaction length is a natural length-scale in the physics of magma/mantle interaction, and has importance for understanding many phenomena.

In non-dimensional form, the governing equations equations (9), (23), (24), and (26) for dimensionless variables $\mathbf{v}_m$, P, $\mathcal{P}$, and ϕ can be written

$$\frac{\partial\phi}{\partial t} - \phi_0^{-1}\boldsymbol{\nabla}\cdot(1-\phi_0\phi)\mathbf{v}_m = \Gamma, \tag{35}$$

$$\boldsymbol{\nabla}\cdot\mathbf{v}_m = \phi_0\frac{\mathcal{P}}{\xi}, \tag{36}$$

$$-\boldsymbol{\nabla}\cdot(\phi^n\boldsymbol{\nabla}\mathcal{P}) + \frac{\mathcal{P}}{\xi} = \boldsymbol{\nabla}\cdot\left[\phi^n(\boldsymbol{\nabla}P - \hat{\mathbf{k}})\right], \tag{37}$$

$$\boldsymbol{\nabla}P = \boldsymbol{\nabla}\cdot\eta\left(\boldsymbol{\nabla}\mathbf{v}_m + \boldsymbol{\nabla}\mathbf{v}_m^T\right) + \phi_0\phi\hat{\mathbf{k}}. \tag{38}$$

In non-dimensionalising (35) we have found it convenient to choose $\Gamma_0 = \rho\phi_0 w_0/\delta$.

Furthermore, to determine the dimensionless magma velocity we have the algebraic relation

$$\phi(\mathbf{v}_f - \mathbf{v}_m) = -\phi^n\left(\boldsymbol{\nabla}\mathcal{P} + \boldsymbol{\nabla}P - \hat{\mathbf{k}}\right). \tag{39}$$

This set of dimensionless equations will be the basis for exploring solutions in the following sections.

Further reading Most of the activity surrounding the derivation of the governing equations that are considered here took place in the eighties. Turcotte and Ahern [1978] and Ahern and Turcotte [1979] developed an influential precursor model, but McKenzie [1984] was the first to write the equations in their current form (and provides references for earlier workers). He was rapidly followed by Fowler [1985], Ribe [1985b], and Scott and Stevenson [1986]. Each of these three papers derived very similar systems of equations. A good summary and review of this early work is given by Stevenson and Scott [1991]. Bercovici et al. [2001a,b] and revisited the problem within a more general mathematical framework and sought to incorporate more

physics (including surface-energy driven flow and damage). Another recent treatments of the derivation by Simpson et al. [2010] used a homogenisation approach and obtained a new term in the equations that was not previously known, with uncertain meaning. In the limit of a large viscosity contrast between the matrix and the liquid phases with small porosity, all of these derivations produce equations that are close or identical to that of McKenzie [1984]. The pressure decomposition used above was proposed by Katz et al. [2007]. Forces derived from surface energy have sometimes been included in the stress-balance equations [Ricard et al., 2001, Hier-Majumder et al., 2006, Takei and Hier-Majumder, 2009], and have a basis in experiments [Riley and Kohlstedt, 1991].

3 Compaction stresses and magmatic flow

Compaction stresses are a new concept for people familiar with mantle convection. They are volumetric stresses, and hence are captured by the compaction pressure $\mathcal{P}$, which is the difference between the fluid pressure and the solid pressure. When the compaction pressure is positive, the magma is pushing the grains apart; when it is negative, it is pulling the grains together. The effects of compaction stresses should become more clear through the concepts in this section.

3.1 The compaction length

To understand the meaning of the compaction length, it is helpful to work in one spatial dimension, with a simplified set of governing equations. In particular, we neglect melting, body forces on the mantle matrix, shear deformations (which are not defined in 1D), and all variations in material properties except permeability. Taking $\xi = 1$, $(1 - \phi_0\phi) \approx 1$, and $\mathbf{v}_m \cdot \hat{\mathbf{k}} = W$, we have the system

$$W_z/\phi_0 = -\left[\phi(w - W)\right]_z \tag{40}$$

$$-\left[\phi^n \mathcal{P}_z\right]_z + \mathcal{P} = -\left[\phi^n\right]_z, \tag{41}$$

where subscript z indicates differentiation with respect to z; variables w and W represent the magmatic and matrix upwelling rates, respectively. Equation (40) represents conservation of mass and is derived by summing the non-dimensional conservation of mass equations; equation (41) is the compaction equation. To simplify things further, we consider only a single instant in time, prescribe the distribution of porosity at that time, and seek a solution of equation (41) for the compaction pressure. The porosity distribution is

$$\phi(z) = \begin{cases} 1 & \text{for } -\infty < z \leq 0 \\ \phi_1 & \text{for } 0 < z < \infty \end{cases}, \tag{42}$$

where ϕ_1 is some dimensionless porosity that not equal to unity. This represents a step-change in porosity at $z = 0$ (recall that gravity points in the $-z$ direction). Since the porosity is piece-wise constant, we can rewrite (41) as

$$\mathcal{P} = \phi^n \mathcal{P}_{zz},$$

which has the general solution

$$\mathcal{P}(z) = A \exp\left(z\phi^{-n/2}\right) + B \exp\left(-z\phi^{-n/2}\right).$$

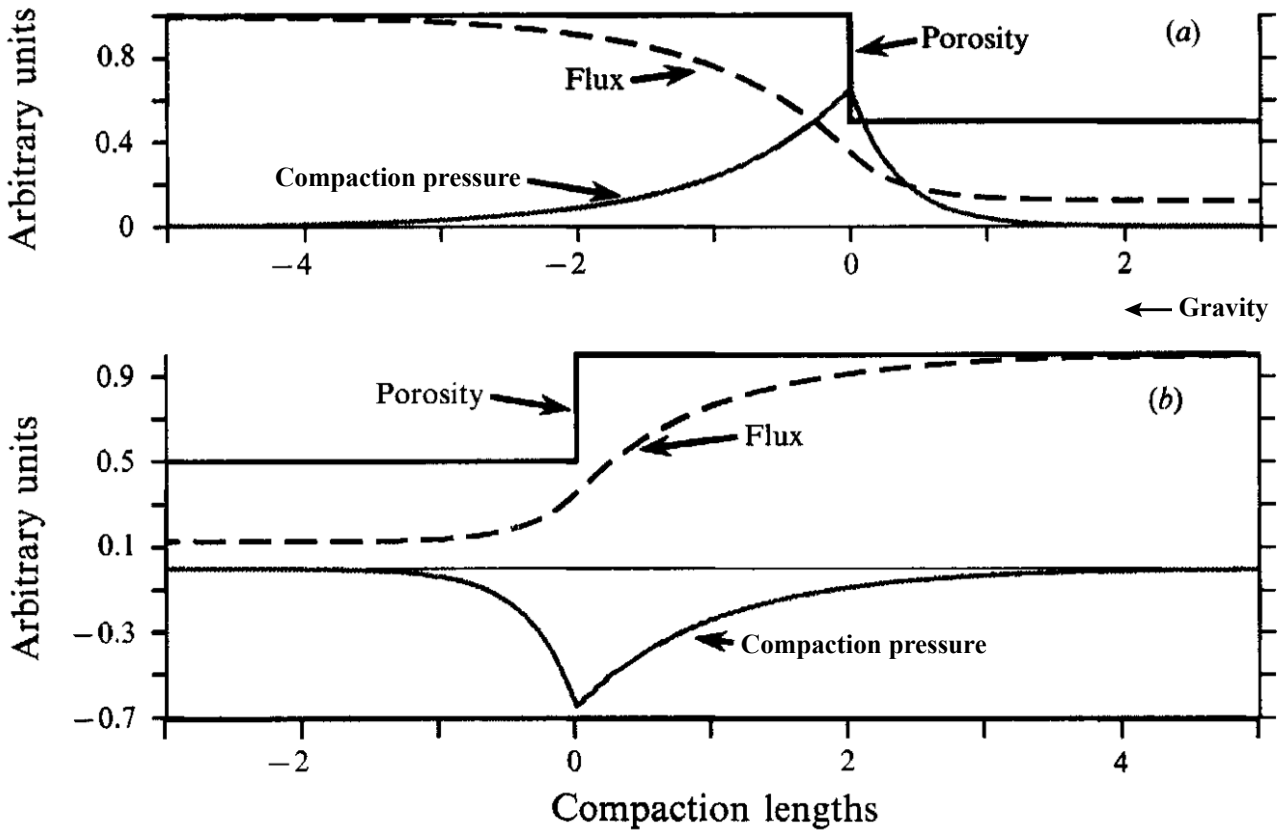

Figure 2: Compaction pressure response to a step-change in porosity. Note that units of the x-axis are *compaction lengths*. **(a)** Negative step-change leads to a decreasing magmatic flux in z and to a positive compaction pressure, which causes the porosity to grow at the interface. **(b)** Positive step-change leads to an increasing magmatic flux in z and a negative compaction pressure, which causes the porosity to shrink at the interface. Adapted from Spiegelman [1993b].

At a large distance from $z = 0$ we expect the compaction pressure and its derivative to decay to zero, while at the interface between the two regions, we expect that the compaction pressure $\mathcal{P}$ is continuous. We have

$$\mathcal{P} = 0, \quad z \to \pm\infty, \tag{43a}$$
$$\mathcal{P}_z = 0, \quad z \to \pm\infty, \tag{43b}$$
$$[\mathcal{P}]_{0-}^{0+} = 0, \quad z = 0, \tag{43c}$$

Applying these conditions allows us to determine the particular solution as

$$\mathcal{P}(z) = \begin{cases} \mathcal{P}_{\max} \exp\left(-z\phi_1^{-n/2}\right), & z > 0, \\ \mathcal{P}_{\max} \exp\left(z\right), & z < 0. \end{cases} \tag{44}$$

To compute the maximum compaction rate, we recall that $\mathcal{P} = W_z/\phi_0$ and then integrate (40) over the real line to obtain

$$\begin{aligned} \int_{-\infty}^{\infty} \mathcal{P}\,\mathrm{d}z &= -\int_{-\infty}^{\infty} \frac{\partial}{\partial z}\phi(w - W)\mathrm{d}z \\ &= -[\phi(w - W)]_{-\infty}^{\infty}, \\ &= 1 - \phi_1^n. \end{aligned} \tag{45}$$

To obtain the last line, we have used Darcy's law applied at $\pm\infty$ where $\mathcal{P}_z = 0$ giving $\phi(w - W) = \phi^n$.

This equation states that the integral of the compaction rate over the whole real line must be equal to the difference between the incoming and the outgoing magmatic flux. Substituting (44) into the LHS and performing the integration gives

$$\mathcal{P}_{\max} = \frac{1-\phi_1^n}{1+\phi_1^{-n/2}}.$$

Solutions for a positive and a negative step-change in porosity are plotted in Figure 2. The key point here is that the change in porosity causes a disturbance to the compaction pressure, and that *this disturbance decays back to the background compaction pressure on a length-scale that is approximately equal to the compaction length*. On the side of $z = 0$ where porosity (and hence permeability) is larger, the compaction length is larger and the pressure-decay occurs over a greater distance.

Hence we can identify the compaction length as the length-scale over which compaction pressure transmits information about physical disturbances in the medium. Two disturbances that are distant by many compaction lengths cannot "feel" each other; two disturbances that are distant by $\mathcal{O}(1)$ compaction length or less will interact through the compaction pressure. The compaction length is thus an inherent length-scale for variations in compaction pressure in this system.

3.2 Solitary wave solutions: magmons

How does the porosity step modelled above evolve with time? To investigate this, we require an additional equation that incorporates the time-dependence. This comes from equation (35), which we simplify by taking $\Gamma = 0$ and $\phi_0 \ll 1$ to obtain

$$\phi_t = W_z/\phi_0. \tag{46}$$

This equation states that the change in time of porosity at a point in z is given by the compaction rate at that point.

Figure 3 shows the evolution of a downward step in porosity according to a numerical solution of equations (41) and (46) (the initial porosity-steps have been smoothed for numerical convergence at $t = 0$). Three step-sizes are shown, corresponding to $\phi_1 = 0.2, 0.5, 0.8$. Panel b of Figure 3 shows the compaction rate at $t = 0$ and $t = 80$. The curve for $t = 0$ has a single, positive excursion at the step, showing that the positive compaction pressure is causing the matrix to dilate there, and porosity to increase, as seen in Figure 2a. With time, this creates a positive porosity excursion. The trailing edge of this excursion acts as an increasing porosity step, as modelled in Figure 2b, and experiences a negative compaction rate, leading to a negative porosity excursion. The process recurses in the $-z$-direction, giving rise to a train of magmatic porosity-waves (known as solitary waves, solitons, or *magmons*). The amplitude of these waves is controlled by the amplitude of the initial step in porosity; their wavelength is determined by the compaction length.

Larger step sizes $(1-\phi_1)$ represent a larger barrier to magmatic ascent, and hence give rise to magmatic waves of larger amplitude. The train of waves grows in the $-z$-direction faster for waves of larger amplitude. Figure 3 also shows that the train of solitary waves propagates in the $+z$-direction under the force of buoyancy. The rate of propagation appears to be constant with time, and increases with ϕ_1 (note the different scales on the z-axes in each column of the figure).

To better understand the characteristics of magmons, it is helpful to consider a detailed analysis of a single wave. We therefore seek a travelling-wave solution to the governing equations

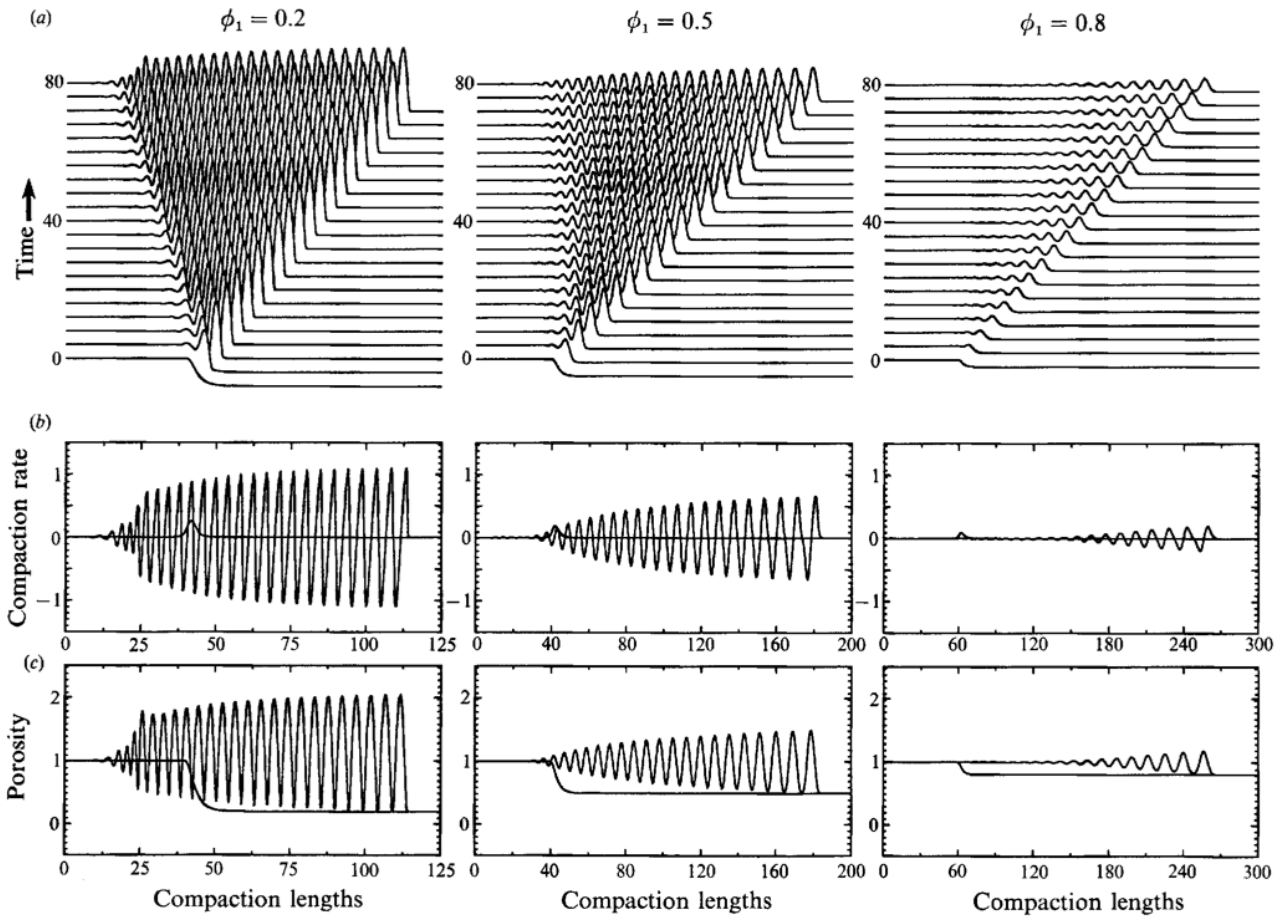

Figure 3: Solitary waves of compaction and porosity arising from three different (smoothed) steps in porosity, given by the three values of ϕ_1. In all cases we have taken $m = 3$. **(a)** Evolution of porosity. The step disperses into a train of solitary waves. **(b)** The compaction rate $W_z = \mathcal{P}$ plotted for $t = 0$ and $t = 80$. **(c)** Comparison of the porosity for each porosity step-size at $t = 0$ and $t = 80$. Adapted from Spiegelman [1993b].

$$\phi_t = \mathcal{P}, \tag{47a}$$

$$-[\phi^n \mathcal{P}_z]_z + \mathcal{P} = -[\phi^n]_z \tag{47b}$$

of the form $\phi = f(\zeta) = f(z - ct)$. Combining (47a) and (47b) and using

$$\frac{\partial}{\partial t} = \frac{\partial}{\partial \zeta}\frac{\partial \zeta}{\partial t} = -c\frac{\partial}{\partial \zeta}, \qquad \frac{\partial}{\partial z} = \frac{\partial}{\partial \zeta}\frac{\partial \zeta}{\partial z} = \frac{\partial}{\partial \zeta},$$

we obtain a third-order equation for f as

$$c\left[f^n f_{\zeta\zeta}\right]_\zeta - c f_\zeta = -\left[f^n\right]_\zeta . \tag{48}$$

Integrating once in ζ and using the boundary condition

$$f = 1 \text{ and } f_{\zeta\zeta} = 0 \text{ as } \zeta \to \infty$$

gives

$$c f^n f_{\zeta\zeta} - c f = -f^n + 1 - c.$$

Substituting $\mathcal{P} = -c f_\zeta$ we find that

$$\mathcal{P}_\zeta = 1 + (c-1) f^{-n} - c f^{1-n}.$$

Now we perform a trick in order to obtain an integrable equation for f; we write the ratio $\mathcal{P}_\zeta/f_\zeta$ as

$$\frac{\mathrm{d}\mathcal{P}}{\mathrm{d}f} = \left(-\frac{c}{\mathcal{P}}\right)\left[1 + (c-1)f^{-n} - cf^{1-n}\right].$$

This can be rearranged and integrated to give

$$\mathcal{P}^2 = -\frac{2c}{f^{n-1}}\left[f^n - \frac{n^2-2n+c}{(n-1)(n-2)}f^{n-1} + \frac{c}{n-2}f + \frac{1-c}{n-1}\right]. \tag{49}$$

Defining A as the maximum porosity of the travelling wave, the dispersion relation (to be determined) is given by $c(A)$. By requiring that $\mathcal{P}(A) = 0$ we can find that

$$c(A) = \begin{cases} (A-1)^2/[A\ln A - (A-1)] & \text{for } n = 2 \\ 2A+1 & \text{for } n = 3. \end{cases} \tag{50}$$

A general solution for $n \geq 3$ exists but is more complicated and not particularly relevant for our purposes.

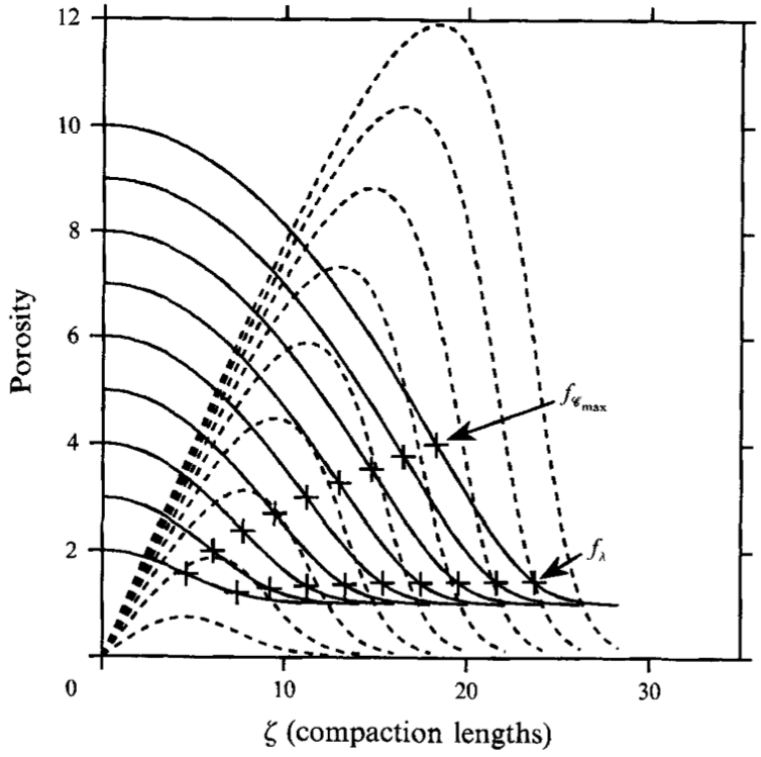

Figure 4: Porosity (solid) and compaction rate (dashed) profiles for $n = 3$ and various values of A that are given by the y-intercept. The porosity is symmetric and the compaction rate is antisymmetric around $\zeta = 0$. The crosses are critical points, discussed in detail by Spiegelman [1993b]. Adapted from Spiegelman [1993b].

The waveform $f(\zeta)$ of our solitary travelling wave is given implicitly by integrating $f_\zeta = -\mathcal{P}/c$ as follows:

$$\zeta(f) = -c\int_A^f \mathcal{P}^{-1}\mathrm{d}f. \tag{51}$$

Using equation (49) and choosing $n = 3$, integration of equation (51) yields

$$\zeta = (A+1/2)^{1/2}\left[-2(A-f)^{1/2} + \frac{1}{(A-1)^{1/2}}\ln\left(\frac{(A-1)^{1/2} - (A-f)^{1/2}}{(A-1)^{1/2} + (A-f)^{1/2}}\right)\right]. \tag{52}$$

This is an implicit formula for the profile of a solitary porosity wave that has maximum porosity A. Profiles for a range of values of A are plotted in Figure 4. We would expect this wave to propagate over a background porosity without changing shape.

Further reading The compaction length has been discussed by nearly every author who has written about the governing equations, but the approach to illustrating its effect that was used in this section was developed by Spiegelman [1993b].

Nonlinear magmatic waves, a type of solitary wave, were among the early solutions to the governing equations to receive significant attention. The pioneering work was done by Richter et al. [1984], Scott and Stevenson [1984], Scott and Stevenson [1986], Barcilon and Richter [1986], and Barcilon and Lovera [1989]. Spiegelman [1993a,b] extended and clarified some of the earlier analysis, and added numerical solutions that illuminated a broader set of problems. Wiggins and Spiegelman [1995] developed three-dimensional numerical solutions. For the mathematically inclined, Simpson et al. [2007] performed formal analysis of the governing equations, and proved stuff about existence and uniqueness.

4 Porosity-band emergence under deformation

In the preceding examples, we considered only a one-dimensional system, with no large-scale matrix deformation, only compaction. Furthermore, although we learned about a behaviour of the governing equations, we were not able to compare model predictions with natural observations or the results of laboratory experiments. In this section we consider experiments on partially molten mantle rocks that are deformed in simple shear at uniform, high pressure and temperature in the laboratory. The samples have an initially uniform porosity of about 4%; after sufficient deformation, they are observed to have developed a pattern of porosity as shown in Figure 5, with high porosity bands ($\sim$10%) oriented at an angle of about 20° to the shear plane, between compacted, low-porosity lenses. The matrix is composed of micron-scale olivine grains, with chromite added to reduce the background compaction length to approximately the thickness of the sample. For details of the experiments, see references provided below. Here we adapt the governing equations of magma dynamics to model these experiments.

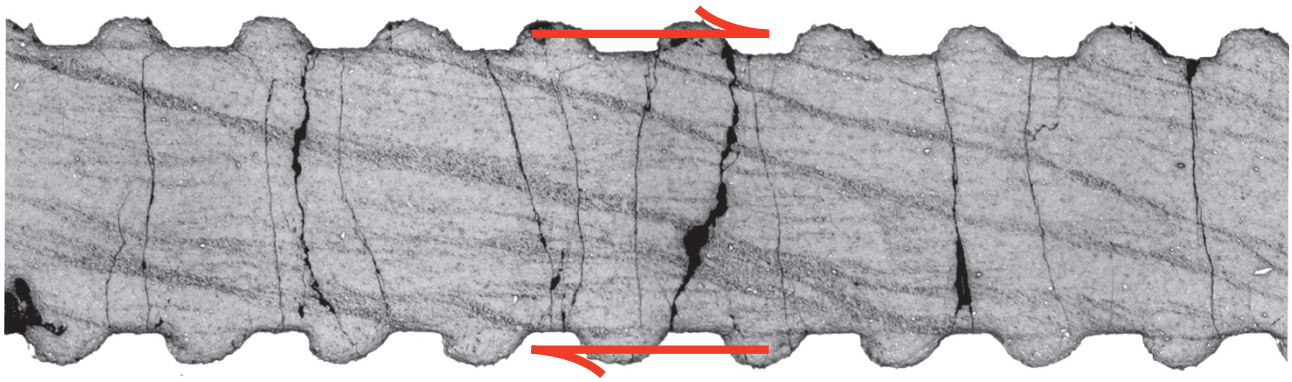

Figure 5: Cross-section of a quenched experiment. Vertical extent is 0.5 mm. Arrows show the imposed simple-shear deformation. Dark bands have a larger fraction of quenched melt; lighter regions are compacted and contain little melt. The initial composition is 4 vol.% MORB evenly distributed in the pores of a matrix composed of 80% olivine and 20% chromite. Total shear strain is $\gamma = 3.4$. Vertical black marks are cracks formed during quench of the experiment and should be ignored. Adapted from Holtzman et al. [2003].

4.1 Governing equations

The system of equations that we need in the present context can be obtained by simplification and manipulation of the dimensional governing equations. In particular, because the sample size is so small, the variation in gravitational potential across it is negligible. We can therefore

discard all buoyancy terms. Also, since there is no conversion of olivine or chromite to melt in the experiments, we can take $\Gamma = 0$. We choose to model the system in two dimensions, as this is the simplest treatment that allows for formation of melt bands. Accordingly we have the dimensional system

$$\frac{\partial \phi}{\partial t} + \mathbf{v}_m \cdot \boldsymbol{\nabla}\phi = (1-\phi)\mathcal{C}, \tag{53a}$$

$$\mathcal{C} = \boldsymbol{\nabla}\cdot \frac{K}{\mu}\left[\boldsymbol{\nabla}\cdot \eta\left(\boldsymbol{\nabla}\mathbf{v}_m + \boldsymbol{\nabla}\mathbf{v}_m^T\right) + \boldsymbol{\nabla}\left(\zeta - \frac{2\eta}{3}\right)\mathcal{C}\right], \tag{53b}$$

$$0 = \boldsymbol{\nabla}\times\boldsymbol{\nabla}\cdot \eta\left(\boldsymbol{\nabla}\mathbf{v}_m + \boldsymbol{\nabla}\mathbf{v}_m^T\right), \tag{53c}$$

where $\mathcal{C} = \boldsymbol{\nabla}\cdot\mathbf{v}_m$ is the compaction rate. The first of this system is an expression of conservation of mass for the solid phase, and states that changes in porosity are due to advection of porosity by the matrix flow, and by compaction. The second equation is the compaction equation, where we have eliminated pressure by substitution of the momentum-balance equation (24); it states that compaction is driven by viscous shear and volumetric stresses associated. The third equation is the momenum-balance equation, after the curl-operator has been applied to eliminate the pressure gradient.

The initial condition for this problem is an idealisation of the experiment: uniform initial porosity ϕ_0 and uniform initial strain-rate $\dot{\gamma}$, such that the initial velocity is given by

$$\mathbf{v}_m = \dot{\gamma} y \hat{\mathbf{i}}, \tag{54}$$

where $\hat{\mathbf{i}}$ is a unit vector in the x-direction, which is also the shear-plane. This equation states that to leading order, matrix flow is in the direction of the shear plane, increases with distance from $y = 0$, and is divergence-free (hence there is no compaction initially). Since the porosity is uniform initially, we can also assume uniform initial permeability K_0 and uniform initial viscosity η_0 and ζ_0. We can consider any deviations from this state to be *perturbations* to the initial condition (also called the *basic state*). We'll assume that the perturbations are small relative to the initial state, and hence they will be scaled with a small constant ε. In particular,

$$\phi = \phi_0 + \varepsilon\phi_1 \tag{55a}$$

$$\mathcal{C} = 0 + \varepsilon\mathcal{C}_1 \tag{55b}$$

$$\begin{aligned}\mathbf{v}_m &= \mathbf{v}_{m,0} + \varepsilon\mathbf{v}_{m,1} \\ &= \dot{\gamma} y\hat{\mathbf{i}} + \varepsilon(\boldsymbol{\nabla}\times\psi_1\hat{\mathbf{k}} + \boldsymbol{\nabla}\mathcal{U}_1)\end{aligned} \tag{55c}$$

$$K = K_0 + \varepsilon K_1 \tag{55d}$$

$$\eta = \eta_0 + \varepsilon\eta_1. \tag{55e}$$

Here we have decomposed the perturbation of the matrix velocity $\mathbf{v}_{m,1}$ into two parts using a *Helmholtz decomposition*. By writing it as the sum of the curl of vector potential ψ_1 plus the gradient of a scalar potential $\mathcal{U}_1$, we have separated the divergence-free (shear) component and the shear-free (compaction) component. It is left as an exercise for the reader to confirm this by showing

$$\boldsymbol{\nabla}\cdot(\boldsymbol{\nabla}\times q\hat{\mathbf{k}}) = 0 \text{ and } \boldsymbol{\nabla}\times\boldsymbol{\nabla}r = 0 \tag{56}$$

for all two-dimensional scalar functions q and r.

We'd like to solve for the unknown perturbation $\phi_1, \mathcal{C}_1, \psi_1, \mathcal{U}_1$. We start by substituting equations (55) into equations (53). We then assume that leading-order terms (those multiplied by $\varepsilon^0 = 1$) balance each other, and that second-order terms (those multiplied by ε^2) are very

small and can be dropped. This leaves only the first-order terms (ε^1), and gives us a set of equations for the perturbations

$$\frac{\partial \phi_1}{\partial t} + \dot{\gamma} y \frac{\partial \phi_1}{\partial x} = (1-\phi_0)\mathcal{C}_1, \tag{57a}$$

$$-\delta^2 \nabla^2 \mathcal{C}_1 + \mathcal{C}_1 = 2\dot{\gamma} \frac{\delta^2}{(\zeta_0 + 4\eta_0/3)} \frac{\partial^2 \eta_1}{\partial x \partial y}, \tag{57b}$$

$$\nabla^2 \mathcal{U}_1 = \mathcal{C}_1, \tag{57c}$$

$$\nabla^2(\nabla^2 \psi_1) = \frac{\dot{\gamma}}{\eta_0}\left(\frac{\partial^2 \eta_1}{\partial x^2} - \frac{\partial^2 \eta_1}{\partial y^2}\right), \tag{57d}$$

where $\delta = (k_0(\zeta_0 + 4\eta_0/3)/\mu)^{1/2}$ is the leading-order compaction length. Equation (57a) is a linearised conservation of mass equation, equation (57b) is the linearised compaction equation, (57c) is the linearised definition of the perturbation compaction rate, and (57d) is a linearised version of the momentum balance governing shear-deformation of the matrix. (57b) states that compaction is driven by simple-shear deformation acting on gradients in the viscosity of the two-phase aggregate. The mixed derivative $\partial^2\eta/(\partial x \partial y)$ indicates that weak bands oriented at 45° to the shear plane would give the absolute largest driving force for compaction.

Equations (57) can be closed by specifying a constitutive equation for the shear viscosity, η (the perturbation to the bulk viscosity does not appear in (57) and hence a constitutive equation for ζ is not required). A basic form for shear viscosity of the two-phase medium can be written as

$$\eta(\phi) = \eta_0 \exp[-\lambda(\phi - \phi_0)], \tag{58}$$

where the constant η_0 accommodates the amplitude of the viscosity and the exponential accommodates the weakening of the material with porosity; λ is a positive constant, empirically determined to be ∼30. As we shall see, this weakening is essential to the formation of high-porosity bands. The viscosity law can be linearised with a Taylor-series expansion of the exponential as

$$\eta \approx \eta_0(1 - \varepsilon\lambda\phi_1). \tag{59}$$

Equations (57) are non-dimensionalised using

$$t = \dot{\gamma}^{-1} t', \qquad \mathbf{x} = \delta \mathbf{x}',$$
$$\mathcal{C}_1 = \dot{\gamma}\mathcal{C}_1', \qquad (\psi_1, \mathcal{U}_1) = \dot{\gamma}\delta^2(\psi_1', \mathcal{U}_1').$$

Substituting these scalings and the equation $\eta_1 = -\eta_0\lambda\phi_1$, and dropping primes on dimensionless variables gives

$$\frac{\partial \phi_1}{\partial t} + y \frac{\partial \phi_1}{\partial x} = (1-\phi_0)\mathcal{C}_1, \tag{60a}$$

$$-\nabla^2 \mathcal{C}_1 + \mathcal{C}_1 = -2\lambda\xi \frac{\partial^2 \phi_1}{\partial x \partial y}, \tag{60b}$$

$$\nabla^2 \mathcal{U}_1 = \mathcal{C}_1, \tag{60c}$$

$$\nabla^4 \psi_1 = -\lambda\left(\frac{\partial^2 \phi_1}{\partial x^2} - \frac{\partial^2 \phi_1}{\partial y^2}\right). \tag{60d}$$

We now seek solutions to these equations on an infinite domain, in two different limits.

4.2 Solution for constant viscosity

For a constant viscosity, time-dependent flow, the perturbations $\mathcal{C}_1$, ψ_1, and $\mathcal{U}_1$ are all zero, and hence there is no perturbation-compaction or perturbation-shear. The perturbation in porosity

obeys the equation

$$\frac{\partial \phi_1}{\partial t} + y\frac{\partial \phi_1}{\partial x} = 0, \tag{61}$$

which states that the initial porosity field is *advected* by the simple-shear flow. This equation has the solution

$$\phi_1(x, y, t) = f(x - yt, y), \tag{62}$$

where f is an arbitrary function that specifies the initial condition $\phi_1(x, y, 0) = f(x_0, y_0)$. For the analysis in the next section, it is convenient to define the perturbation porosity to be a plane-wave with initial wave-vector $\boldsymbol{\kappa}_0 = \kappa_x^0\hat{\mathbf{i}} + \kappa_y^0\hat{\mathbf{j}}$, such that the initial condition is $\phi_1(\mathbf{x}, 0) = \exp(i\boldsymbol{\kappa} \cdot \mathbf{x})$. This initial condition evolves according to

$$\begin{aligned}\phi_1(\mathbf{x}, t) &= \exp\left[i\left(\kappa_x^0(x - yt) + \kappa_y^0 y\right)\right] \\ &= \exp(i\boldsymbol{\kappa}(t) \cdot \mathbf{x}),\end{aligned} \tag{63}$$

where

$$\boldsymbol{\kappa}(t) = \kappa_x^0\hat{\mathbf{i}} + (\kappa_y^0 - \kappa_x^0 t)\hat{\mathbf{j}} \tag{64}$$

is a time-dependent wave-vector that rotates with the flow and changes length. A perturbation oriented like the melt bands in Figure 5 has $\kappa_y^0 > \kappa_x^0 > 0$.

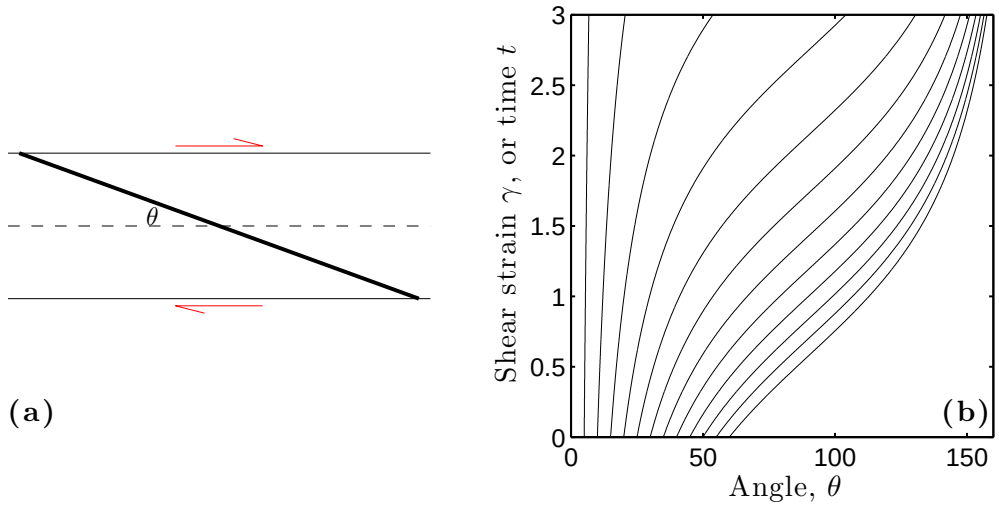

Figure 6: **(a)** Schematic diagram of simple shear with a single band oriented at an angle θ to the shear plane, which is indicated by a dashed line. **(b)** Evolution of the angle of bands that are passively advected by the simple-shear flow. These lines are called *passive advection trajectories*.

The angle of a wavefront to the shear plane is given by $\theta(t) = \tan^{-1}[\kappa_x^0/\kappa_y(t)]$ (as shown in Figure 6a). These trajectories are shown for a variety of initial angles in Figure 6b; note that simple-shear deformation does not rotate bands uniformly, rather the rotation rate is largest for bands near 45°.

4.3 Solution for variable viscosity

When viscosity is allowed to vary with porosity, the bands of higher porosity will be weaker than the bands of lower porosity. We expect this to lead to growth in the porosity difference between the two. We also expect that the porosity perturbations will be rotated according the wave-vector defined in (64). Since the governing equations are linear, we expect exponential

solutions and write the perturbations as

$$\phi_1 = \exp\left[i\boldsymbol{\kappa}(t)\cdot\mathbf{x} + s(t)\right], \tag{65a}$$
$$\mathcal{C}_1 = \mathcal{C}^*(t)\exp\left[i\boldsymbol{\kappa}(t)\cdot\mathbf{x} + s(t)\right], \tag{65b}$$
$$\mathcal{U}_1 = \mathcal{U}^*(t)\exp\left[i\boldsymbol{\kappa}(t)\cdot\mathbf{x} + s(t)\right], \tag{65c}$$
$$\psi_1 = \psi^*(t)\exp\left[i\boldsymbol{\kappa}(t)\cdot\mathbf{x} + s(t)\right]. \tag{65d}$$

Here $s(t)$ is the growth rate of the perturbations and $\mathcal{C}^*(t), \mathcal{U}^*(t), \psi^*(t)$ are time-dependent amplitude coefficients, to be determined. Substitution of equations (65) into (60) followed by laborious algebraic manipulations gives a set of equations for the time-dependent amplitudes; only one of these is important for the present discussion

$$\frac{\mathrm{d}s}{\mathrm{d}t} = 2\lambda\xi(1-\phi_0)\frac{\kappa_x\kappa_y}{\kappa^2+1}, \tag{66}$$

where $\kappa^2 = \boldsymbol{\kappa}\cdot\boldsymbol{\kappa} = |\boldsymbol{\kappa}|^2$.

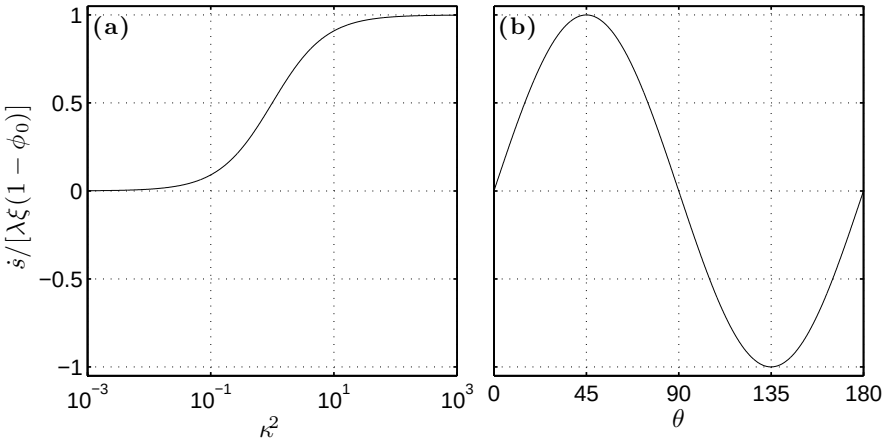

Figure 7: Normalised growth rate of porosity perturbations, $\mathrm{d}s/\mathrm{d}t$. **(a)** Growth rate for a perturbation oriented at 45° to the shear plane, as a function of the squared amplitude of the wave-vector $\boldsymbol{\kappa}$. **(b)** Growth rate as a function of perturbation angle θ for $\kappa^2 \gg 1$.

Equation (66) is an equation for the growth-rate of porosity perturbations. Using $\kappa_x = |\boldsymbol{\kappa}|\sin\theta$, $\kappa_y = |\boldsymbol{\kappa}|\cos\theta$, and $2\sin 2\theta = \sin\theta\cos\theta$, we can rewrite it as

$$\dot{s} = \lambda\xi(1-\phi_0)\frac{\kappa^2\sin 2\theta}{\kappa^2+1}. \tag{67}$$

This equation shows two important things. First, if $|\boldsymbol{\kappa}|^2 \ll 1$ then the growth rate $\dot{s}$ is very small. This corresponds to perturbations with wavelength much greater than the compaction length. Based on what we know about the compaction length, this makes sense: if the perturbations are spaced widely relative to the compaction length, they do not "feel" each other through the compaction pressure, and hence there is no segregation flow of magma. For $|\boldsymbol{\kappa}|^2 \gg 1$, the growth rate is $\dot{s} = \lambda\xi(1-\phi_0)\sin 2\theta$, which reveals the second important result: the growth rate is at a maximum for bands oriented at $\theta = 45°$. Figure 7 shows both of these relationships in more detail.

Although we have determined the growth rate of perturbations, we have not really yet solved the problem, because the perturbations grow *and rotate*. To capture both effects, we

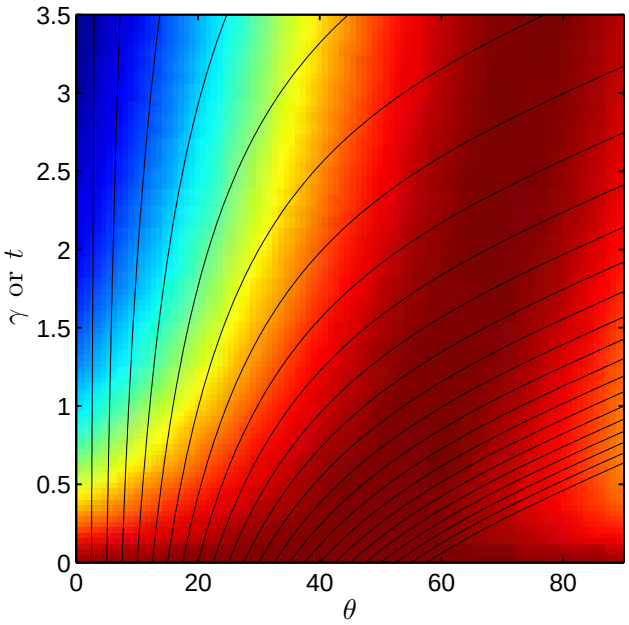

Figure 8: Porosity-perturbation amplitude $\exp[s(t)]$ as a function of perturbation band angle and time, computed with (68). The angular distribution of amplitude has been normalised at each time by the maximum amplitude at that time. Black lines are passive advection trajectories.

must integrate the growth rate (66) over time,

$$\begin{aligned} s(t) &= 2\lambda\xi(1-\phi_0)\int_0^t \frac{\kappa_x^0(\kappa_y^0-\kappa_x^0\tau)}{(\kappa_x^0)^2+(\kappa_y^0+\kappa_x^0\tau)^2+1}\mathrm{d}\tau, \\ &= \lambda\xi(1-\phi_0)\ln\left[\frac{\kappa(0)^2+1}{\kappa(t)^2+1}\right], \end{aligned} \tag{68}$$

where we have used τ as a dummy-variable of integration. Amplitude of the perturbation is then given by

$$|\phi_1| = \exp[s(t)] = \left[\frac{\kappa(0)^2+1}{\kappa(t)^2+1}\right]^{\lambda\xi(1-\phi_0)},$$

which is plotted in Figure 8 for $|\kappa(0) = 4\pi$.

Figure 8 shows that perturbations at angles greater than 50° eventually dominate the system, whereas in experiments (Figure 5), bands are typically oriented at about 20°. While our model predicts growth of high-porosity bands, it also predicts that they will appear at a high angle to the shear plane. What might be missing that would correct this? One possibility is that our viscosity formulation (58) was too simple, in that it neglected non-Newtonian effects.

4.4 Solutions for non-Newtonian viscosity

A viscosity formulation that captures the strain-rate dependence of viscosity is given by

$$\eta(\phi, \mathbf{v}_m) = \eta_0 \mathrm{e}^{-\lambda(\phi-\phi_0)}\dot{\epsilon}_{II}^{(1-n)/n}. \tag{69}$$

In this equation, $\dot{\epsilon}_{II}$ is the second invariant of the strain-rate tensor, $\dot{\epsilon}_{II} = \sqrt{\dot{\epsilon}_{ij}\dot{\epsilon}_{ij}}$, and n is a constant the represents the sensitivity of viscosity to changes in stress or strain rate (we reuse the variable n here to follow convection, but note that this n and the n used in the porosity–permeability relationship are independent). When $n = 1$, we return to the Newtonian behaviour that we used previously, when $n > 1$, larger stress or strain-rate gives smaller viscosity. The second invariant of the strain rate tensor can be expressed in terms of the velocity expansion given in equation (55c). It can then be linearised and introduced into the equations (57) to obtain an expression for $\dot{s}$ analogous to (67) that reads

$$\frac{\mathrm{d}s}{\mathrm{d}t} = 2\frac{\lambda}{n}\xi(1-\phi_0)\frac{\kappa_x\kappa_y\kappa^4}{(\kappa^2+1)\left[\kappa^4+\frac{1-n}{n}\left(\kappa_x^2-\kappa_y^2\right)^2\right]+4\frac{1-n}{n}\xi\kappa_x^2\kappa_y^2\kappa^2}, \tag{70}$$

which reduces to equation (66) in the Newtonian limit, $n = 1$. For $\kappa^2 \ll 1$ (wavelengths greater than the compaction length), the growth rate of bands approaches zero. For $\kappa^2 \gg 1$ (wavelengths smaller than the compaction length), we can rewrite (70) as a function of perturbation angle $\theta(t)$ as

$$\frac{\mathrm{d}s}{\mathrm{d}t} = \frac{(\lambda/n)\xi(1-\phi_0)\sin 2\theta}{1+\frac{1-n}{n}\left[\cos^2 2\theta + \xi \sin^2 2\theta\right]}. \tag{71}$$

Note that this equation has the same $\sin 2\theta$ term in the numerator, indicating a tendency for bands to grow at 45° to the shear plane. This behaviour is modified for $n > 1$, however, by the term in the denominator that is multiplied by $(1-n)/n$. This term is negative, and reduces the size of the denominator, leading to larger growth rates. The effect of shear-strain weakening is represented by the cosine term in the denominator; it has maxima at 0 and 90 degrees, corresponding with porosity bands that are parallel or perpendicular to the shear plane, as these orientations can most efficiently localise strain (for an infinite domain). The sine term in the denominator represents compaction-strain weakening, but because it is multiplied by ξ, which is probably a small number, its effect is less important.

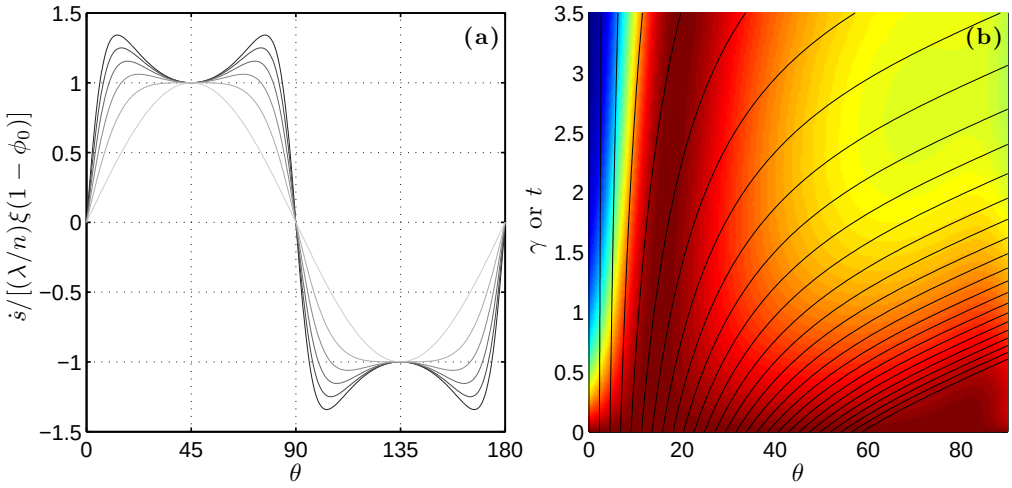

Figure 9: Results for a stability model with non-Newtonian viscosity. **(a)** Normalised growth rate of bands as a function of angle to the shear plane for $\xi \ll 1$. Lines for $n = 1, 2, 3, 4, 5, 6$ are shown, with larger values of n corresponding to darker shades of grey. **(b)** Normalised amplitude $\exp[s(t)]$ for $n = 6$, where $s(t)$ has been computed by integrating (71) over time for a range of initial angles, and then normalising the angular distribution of amplitude at each time by the maximum amplitude at that time.

Figure 9a is a plot of equation (71) as a function of θ. It shows that for larger values of n, the peak in growth rate at 45° splits into two peaks, at low and high angle to the shear plane. Performing an integration of equation (71) gives $s(t)$, which can then be exponentiated to obtain the perturbation amplitude as a function of angle. This is shown in Figure 9b, for $n = 6$. Smaller values of n are a poor fit to data. Note that there is initially growth of bands at angles $\sim 70°$, but these bands are rapidly rotated out of an orientation that is favourable for growth. In contrast, the bands that start at $\sim 15°$ grow rapidly and rotate very slowly. Hence they continue to accumulate porosity and soon dominate the distribution.

Stability analysis is great for studying the onset of instability and in this case, by allowing the perturbation to be advected by the background flow, we have extended it to larger values of strain. But the experiments are clearly in a nonlinear regime, and are characterised by a range of band angles, rather than just one. To extend our investigation, we need solutions to the full, non-linear system of equations. These can only be obtained with numerical methods.

The details of the numerics is beyond the scope of the present notes, but we'll discuss the broad outlines.

4.5 Numerical simulation of porosity bands

The system of non-dimensional governing equations have $\Gamma = 0$ and neglect all buoyancy terms. They are written as follows

$$\frac{\partial \phi}{\partial t} - \boldsymbol{\nabla}\cdot(1-\phi_0\phi)\mathbf{v}_m = 0, \tag{72a}$$

$$\boldsymbol{\nabla}\cdot\mathbf{v}_m = \frac{\mathcal{P}}{\xi}, \tag{72b}$$

$$-\boldsymbol{\nabla}\cdot(\phi^n\boldsymbol{\nabla}\mathcal{P}) + \frac{\mathcal{P}}{\xi} = \boldsymbol{\nabla}\cdot(\phi^n\boldsymbol{\nabla}P)\,, \tag{72c}$$

$$\boldsymbol{\nabla}P = \boldsymbol{\nabla}\cdot\eta\left(\boldsymbol{\nabla}\mathbf{v}_m + \boldsymbol{\nabla}\mathbf{v}_m^T\right). \tag{72d}$$

We will prescribe a non-Newtonian viscosity law (i.e. eqn. (69)) for the shear viscosity, and can take the bulk viscosity to be constant or porosity dependent. The latter choice has important consequences for the calculation results, but the simple choice of a constant bulk viscosity produces results that are reasonably close to experiments.

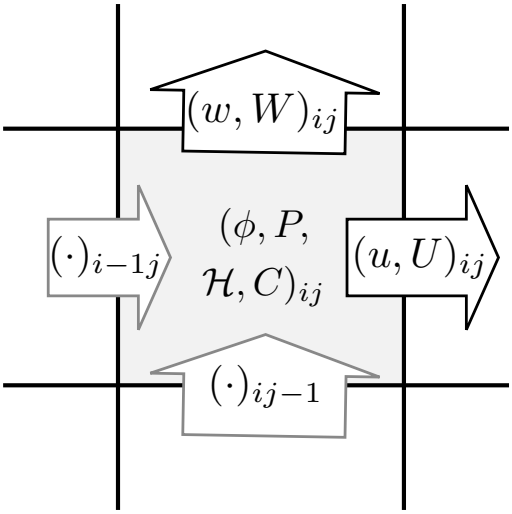

Figure 10: One cell from the middle of a staggered grid in two-dimensions. It is the ith cell in the x-direction and the jth cell in the y-direction. Magma and matrix velocities (denoted here by $\mathbf{v}_m = U\hat{\mathbf{i}} + W\hat{\mathbf{j}}$ and $\mathbf{v}_f = u\hat{\mathbf{i}} + w\hat{\mathbf{j}}$) are stored on the faces of the finite volume, while pressure, porosity (and other variables that will become relevant below) are stored at the cell centre.

The equations are broken into two blocks, the *hyperbolic* block, which consists of all the explicitly time-dependent equations (in this case, just (72a)), and the *elliptic* block, which consists of the rest of the equations. These blocks are discretised using a *finite volume* approach, which breaks the independent variables $(\mathbf{x}, t)$ into finite intervals of constant size $\Delta x, \Delta y, \Delta t$, and uses the fluxes across the faces of those intervals to update the values in the interiors. Fluxes are therefore stored on the faces of the finite volume, while variables such as pressure and porosity are stored at the cell centres, as shown in Figure 10. This is known as a *staggered grid* approach. The finite-volume discretisation is fairly straightforward, though tedious to write out in full. As a demonstration, consider the discretisation of equation (72b) in two dimensions, which is relatively compact:

$$\frac{U^n_{ij} - U^n_{i-1j}}{\Delta x} + \frac{U^n_{ij} - W^n_{ij-1}}{\Delta y} - \frac{\mathcal{P}^n_{ij}}{\xi^n_{ij}} = 0. \tag{73}$$

There is an entire field of research devoted to finding efficient, accurate, and stable methods for solving systems of non-linear, algebraic equations on computers, and it is not possible to

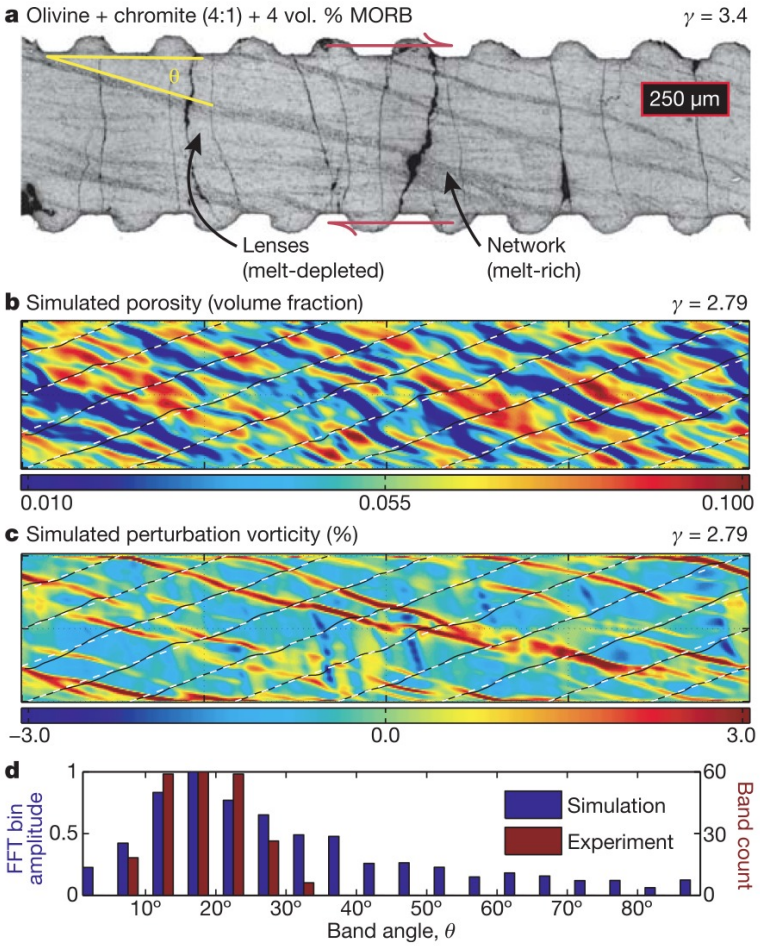

Figure 11: Comparison of high-porosity bands in an experiment and a numerical simulation. **(a)** Experiment to strain $\gamma = 3.4$ **(b)** Porosity field (colour) from a simulation with $n = 6$ and $\lambda = 27$ at a shear strain of 2.79. **(c)** The perturbation vorticity from the same numerical simulation. Perturbation vorticity is the percent deviation from simple shear, $\boldsymbol{\nabla}\times[\mathbf{v}_m - \dot{\gamma}y\hat{\mathbf{i}}]/\dot{\gamma} \times 100$. Black lines in (b) and (c) show the position of passive tracer particles that were arrayed in vertical lines at $\gamma = 0$; white dotted lines show the expected position of the tracers due only to simple shear. The linear, low-angle red bands in (c) are weak regions associated with high porosity and enhanced shear, while the linear, sub-vertical blue regions are regions of reversed shear. **(d)** Histograms comparing band-angle distributions in experiments and the numerical solution from (b). Figure from Katz et al. [2006].

convey any reasonable amount in these notes, so the numerical solution of these equations will have to remain a "black-box" for the present.

Figure 11 shows the result of a numerical simulation with $n = 6$ and $\lambda = 27$ at a shear strain of 2.79, as compared to an experiment. The domain is one compaction length high, and five compaction lengths wide. The initial porosity was 4%. With progressive shear strain, porosity localised into low-angle bands that are evident as red streaks. These bands shift and reconnect with progressive strain to maintain low angle. They also localise strain, as shown in panel (c), where strain rates exceeding that expected for simple shear are show by warm colours. Note the existence of a conjugate set of high angle bands of diminished strain rate. The deviation of the black lines shows the accumulated strain deviation from simple shear. Panel (d) shows a histogram of band angles from experiments compared with an angular power spectrum of the porosity field from panel (b).

Although numerical simulations and stability analysis with non-Newtonian viscosity and large n both show a good agreement with experimental results, there are two key issues that must be noted. Firstly, experimenters have confirmed that not all of their experiments that produce bands are in the deformation regime where non-Newtonian viscosity is expected. Their experiments with Newtonian viscosity produce the same distribution of low-angle bands. Secondly, olivine grains in deformation by dislocation creep have a non-Newtonian viscosity, but with a value of $n \approx 3.5$. So the requirement of large n seems problematic. In this context, however, the non-Newtonian viscosity effectively means that weak zones at a low angle to the shear plane can concentrate strain and hence become even weaker. It has been recently shown that the same directionally-variable behaviour arises from anisotropic Newtonian viscosity. If the pores between grains align at low angle to the shear plane, they can lead to a preferential grain-sliding direction that represents a weak plane. This is predicted to lead to rapid growth

of low-angle bands. See references for more information.

Further reading The instability was discovered by Stevenson [1989], who considered a 1D model of an extending, partially molten system with porosity weakening viscosity. It was later produced in experiments, leading to a series of papers that are reviewed by Kohlstedt and Holtzman [2009]. The latest experiments use torsional deformation and larger samples [King et al., 2010].

The theoretical development progressed with papers by Richardson [1998], who considered the influence of buoyancy, Hall and Parmentier [2000], who added water to the problem, and Spiegelman [2003], who sought to analyse the experiments in simple shear geometry. The non-Newtonian analysis was developed by Katz et al. [2006]. More recent work by Butler [2009] has reexamined how buoyancy-driven flow changes the system, and considered the instability under pure shear rather than simple shear [Butler, 2010]. The porosity-banding instability was not observed to occur in mid-ocean ridge simulations by Katz [2010].

5 Tectonic-scale models with constant porosity and no melting

To make a preliminary investigation into magmatic flow at mid-ocean ridges and subduction zones, we can make some rather severe assumptions that allow for an analytical solution. We assume

No melting We assume that magma enters our model from outside the domain, and that there is no melting internal to the domain.

Constant porosity We assume that the porosity is independent of space and time.

Constant mantle viscosity We assume that $\eta = \eta_0$, constant.

No matrix buoyancy We assume that the mantle flow is driven entirely by the boundary conditions (kinematically prescribed plates).

With these assumptions, the conservation of mass equations become $\boldsymbol{\nabla}\cdot\mathbf{v}_m = \boldsymbol{\nabla}\cdot\mathbf{v}_f = 0$. We can therefore define two stream-functions as

$$\mathbf{v}_m = \boldsymbol{\nabla}\times\psi_m\hat{\mathbf{j}}, \tag{74a}$$

$$\mathbf{v}_f = \boldsymbol{\nabla}\times\psi_f\hat{\mathbf{j}}. \tag{74b}$$

The matrix stream-function is driven by the boundary conditions (spreading plates in ridge setting, down-going and overlying plates in subduction zone), while the magmatic stream-function is driven by buoyancy and the fluid pressure gradient set up by solid flow.

The momentum equation for the matrix with constant viscosity, no buoyancy, and no compaction is given by

$$\boldsymbol{\nabla}P_f = \eta_0\nabla^2\mathbf{v}_m.$$

Taking the curl of this equation (to eliminate the pressure gradient) and substituting (74a) gives the biharmonic equation,

$$\nabla^4\psi_m = 0. \tag{75}$$

We need a solution to equation (75), subject to the boundary conditions illustrated in Figure 12. The solution can be obtained in polar coordinates, and the mantle velocity is then given by

$$\mathbf{v}_m = \frac{1}{r}\frac{\partial\psi_m}{\partial\theta}\hat{\mathbf{r}} - \frac{\partial\psi_m}{\partial r}\hat{\boldsymbol{\theta}}, \tag{76}$$

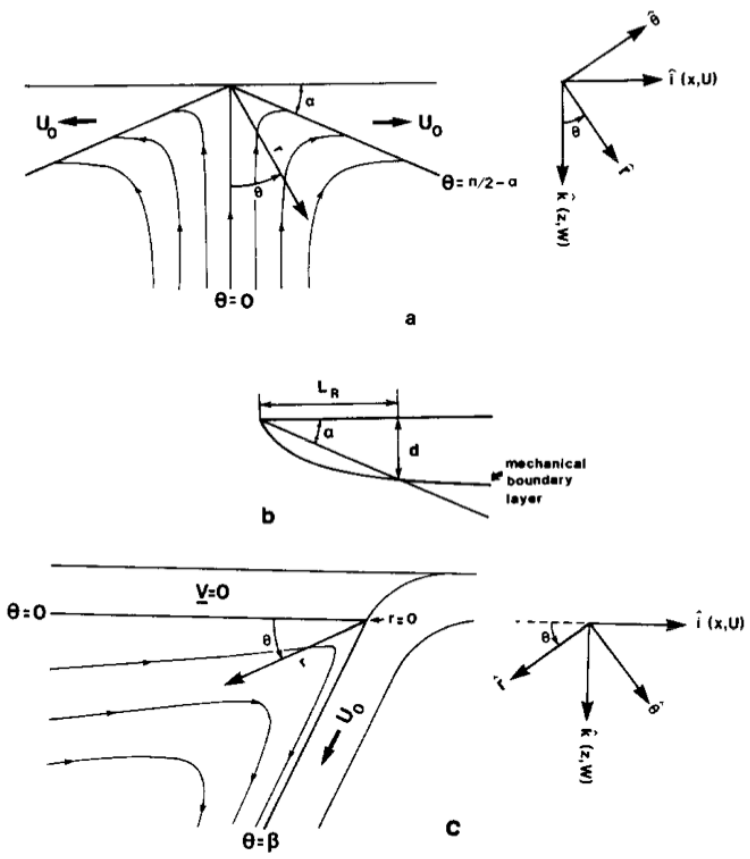

Figure 12: Domain and boundary conditions for the constant-porosity models of a mid-ocean ridge and subduction zone. **(a)** The mid-ocean ridge domain. Plates spread with half-rate U_0 and have a sloping bottom boundary. The solution lives in the region below the plates, and is symmetrical across the ridge axis. The polar coordinate system is shown on the right side of the diagram. **(b)** Comparison of a thermally-induced lithospheric boundary for an oceanic plate, and the approximated linear boundary. **(c)** Geometry and boundary conditions for a subduction zone model. The overriding plate is fixed and the down-going slab converges with rate U_0 and dip β. The solution lives in the wedge above the slab and below the overriding plate. The polar coordinate system is given at right. Figure from Spiegelman and McKenzie [1987].

where $\hat{\mathbf{r}}$ and $\hat{\boldsymbol{\theta}}$ are the polar basis vectors. The dimensionless matrix stream-function can be obtained as

$$\psi_m = r f(\theta) = \begin{cases} r(A\sin\theta + B\theta\cos\theta) & \text{for the mid-ocean ridge} \\ r[C(\sin\theta - \theta\cos\theta) + D\theta\sin\theta] & \text{for the subduction zone} \end{cases} \tag{77}$$

where

$$A = \frac{2\sin^2\alpha}{\pi - 2\alpha - \sin 2\alpha} \qquad B = \frac{2}{\pi - 2\alpha - \sin 2\alpha}$$
$$C = \frac{\beta\sin\beta}{\beta^2 - \sin^2\beta} \qquad D = \frac{\beta\cos\beta - \sin\beta}{\beta^2 - \sin^2\beta}.$$

This is known as the *corner flow* solution, because it produces streamlines that turn the corner that is imposed by the boundary conditions, as shown in Figure 12. The intense shear at the apex of the corner leads to a negative singularity of pressure there. This negative pressure establishes a pressure gradient (suction) that, in the present model, extends out into the mantle and draws magma toward it.

Using the matrix stream-function from equation (77), the magmatic stream-function can be obtained as

$$\psi_f = \psi_m - \frac{w_0}{U_0} \times \begin{cases} \left(\frac{2B}{r} + r\right)\sin\theta & \text{for the mid-ocean ridge,} \\ \left[\frac{2}{r}(C\sin\theta + D\cos\theta) - r\cos\theta\right] & \text{for the subduction zone,} \end{cases} \tag{78}$$

where

$$w_0 = \frac{K_0(1-\phi_0)\Delta\rho g}{\mu\phi_0},$$

is the buoyancy-driven flow rate. Equation (78) shows that if $w_0 \ll U_0$, $\psi_f \approx \psi_m$ and the magma moves with the mantle flow. If, on the other hand, $w_0 \gg U_0$, the magma is dominantly driven

by buoyancy and pressure gradients arising from the mantle deformation, and the matrix flow becomes irrelevant to the magma. If $K_0 = 1 \times 10^{-13}$ m^2, $\Delta\rho g = 5000$ kg/m^2/sec^2, $\mu = 1$ Pa sec, $\phi = 0.01$, and $U_0 = 3$ cm/yr then w_0/U_0 is of order 10. It would have been an unpleasant surprise to find that our model predicted that magma would travel with the mantle flow!

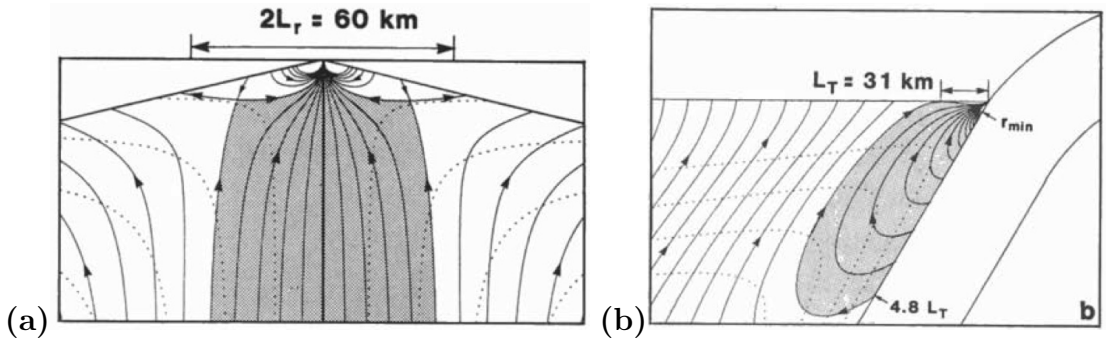

Figure 13: Solutions for the constant-porosity magmatic flow problem with $U_0 = 7.5$ cm/yr, $\eta_0 = 10^{21}$ Pa-sec, and $\phi_0 = 1.5\%$. Dotted lines are mantle streamlines and solid lines are magmatic streamlines. L_R and L_T are calculated using equation (79). **(a)** The ridge case with $\alpha = 13°$. Grey region is the predicted ridge focusing region for magma generated at depth. **(b)** The subduction case, with $\beta = 60°$. Grey region is the predicted arc focusing region for magma from the slab. Figure from Spiegelman and McKenzie [1987].

Figure 13 shows two example calculations, one ridge and one subduction zone, for parameters as given in the figure caption. The dotted lines are matrix streamlines and the solid lines are magmatic streamlines. Magma flows upward under buoyancy; if it near the ridge axis, it is sucked toward it by the dynamic pressure gradient (grey region); if it rises further away from the axis, its trajectory is bent away from the axis by mantle flow (white regions on the flanks).

What is the length-scale for focusing of magmatic streamlines to the ridge axis? This depends on the relative importance of the dynamic suction that arises from the shear flow compared to the buoyancy force, as a function of distance. A dimensional analysis of the solution for the fluid pressure P_f indicates that the pressure gradient arising from mantle shear has a length-scale given by

$$L = \left[\frac{\eta_0 U_0}{(1-\phi_0)\Delta\rho g} \right]^{1/2}. \tag{79}$$

This indicates that the pressure gradient is more important if the mantle viscosity is large (the other parameters are relatively well constrained). If $\eta_0 = 10^{21}$ Pa-sec, then the L is about 10 km, whereas if $\eta_0 = 10^{19}$ Pa-sec, L is about 1 km. In the former case, we'd expect magmatic streamlines to be significantly bent by the dynamic pressure gradient, driving flow into the corner. In the latter case, we'd expect buoyancy to dominate and give magmatic streamlines that are generally vertical. Given our current understanding of mantle rheology at plate boundaries, it is unlikely that the suction effect due to mantle corner-flow is a driver of melt focusing toward the ridge axis or volcanic arc.

Further reading The analysis above was developed by Spiegelman and McKenzie [1987], and closely parallels a similar analysis by Phipps Morgan [1987].

6 Governing equations: thermodynamics and chemistry

So far, we've focused on problems in coupled magma/mantle dynamics where there is no melting. But it is melting that produces magma in the first place, and links mantle convection

and plate tectonics with magmatism and volcanism. So it is important to put melting into our models!

Melting is a thermodynamic process of phase-change whereby solid grains of rock reach their melting temperature and some of their mass is converted from the solid state to the liquid state. The full thermodynamics of mantle melting are horrendously complicated, requiring more than 10 thermochemical components (and a similar number of mineral phases) to accurately describe the system. Dynamical models of magma/mantle interaction require a simpler approach, but one the preserves the basic features of more sophisticated models, and is consistent with conservation of mass and energy. Hence the foundation of our theoretical model should include a PDE representing conservation of energy, as well as other representing conservation of mass for each of the chemical species that we wish to include in the model.

6.1 Conservation of energy

To derive a conservation of energy equation, we begin by considering the same representative volume element that was introduced in section 2.1 above. Within the RVE there is a mass of magma and mantle; there is also some quantity of energy, which we now seek to constrain. Let's define H as the enthalpy per unit volume within the RVE. Recall that enthalpy is the sum of internal energy (energy stored as sensible or latent heat) plus energy stored as compressional work plus chemical potential energy (though we neglect this last contribution). The total energy stored in the RVE is the sum of the enthalpy, the potential energy, and the kinetic energy. This latter contribution can be neglected, because the mantle is moving extremely slowly. Hence we can write the total energy contained with the RVE as

$$\int_{\mathrm{RVE}} (H - \overline{\rho}\mathbf{g}\cdot\mathbf{x})\mathrm{d}V, \tag{80}$$

where the second term in the integral represents the potential energy. If the axes are aligned such that $\hat{\mathbf{k}}$ points in the direction opposite gravity (i.e. upward), we find that the potential energy is $-\overline{\rho}\mathbf{g}\cdot\mathbf{x} = \overline{\rho}gz$.

The total energy within the RVE changes according to fluxes of energy into/out of the RVE, as well as sources or sinks of energy within it. There are three fluxes to consider: (a) fluxes of enthalpy carried by the magma or matrix; (b) fluxes of potential energy carried by the magma or matrix; and (c) fluxes of sensible heat by diffusion. These can be represented by an integral over the surface of the RVE,

$$\int_{\partial\mathrm{RVE}} \left(\overline{\rho h\mathbf{v}} - \overline{\rho\mathbf{v}}\mathbf{g}\cdot\mathbf{x} - \overline{k}\boldsymbol{\nabla}T\right)\cdot\mathbf{dS}, \tag{81}$$

where h is the enthalpy per unit mass, k is the thermal conductivity, and T is the temperature. Recall that an overbar represents a phase-averaged quantity, $\overline{\rho h\mathbf{v}} = \rho_f h_f \mathbf{v}_f \phi + \rho_m h_m \mathbf{v}_m (1-\phi)$. The first term is the enthalpy flux out of the RVE, the second term is the potential energy flux, and the third term is the diffusive heat flux. We have assumed that both the magma and the matrix have the same temperature when they are in contact at a point; hence there is a single temperature field $T(\mathbf{x}, t)$.

There are two source terms that we could consider within the RVE, radiogenic heat production by decay of Uranium, Thorium, and Potassium, as well as heating by frictional dissipation. This latter is the irreversible conversion of mechanical work into heat through friction (such as what happens when you rub your hands together vigorously). For simplicity, and because these terms are relatively small in the contexts that will concern us here, we neglect these sources of energy. We can therefore write a conservation equation for the RVE as

$$\frac{\mathrm{d}}{\mathrm{d}t}\int_{\mathrm{RVE}} (H - \overline{\rho}\mathbf{g}\cdot\mathbf{x})\mathrm{d}V = -\int_{\partial\mathrm{RVE}} \left(\overline{\rho h\mathbf{v}} - \overline{\rho\mathbf{v}}\mathbf{g}\cdot\mathbf{x} - \overline{k}\boldsymbol{\nabla}T\right)\cdot\mathbf{dS}, \tag{82}$$

where the negative sign on the RHS ensures that a flux out of the RVE *reduces* the energy within the RVE.

To convert this to a PDE we apply Gauss' theorem to the RHS and allow our RVE to shrink to the infinitesimal limit. We obtain

$$\frac{\partial H}{\partial t} - \mathbf{g}\cdot\mathbf{x}\left(\frac{\partial \overline{\rho}}{\partial t} + \boldsymbol{\nabla}\cdot\overline{\rho\mathbf{v}}\right) + \boldsymbol{\nabla}\cdot\overline{\rho h\mathbf{v}} - \mathbf{g}\cdot\overline{\rho\mathbf{v}} = \boldsymbol{\nabla}\cdot\overline{k}\boldsymbol{\nabla}T. \tag{83}$$

Our job is now to simplify this equation using judicious assumptions and other conservation laws. The sum of conservation of mass equations (8) and (9) tells us that

$$\left(\frac{\partial \overline{\rho}}{\partial t} + \boldsymbol{\nabla}\cdot\overline{\rho\mathbf{v}}\right) = 0. \tag{84}$$

Expanding the divergence of the enthalpy flux term in (83) and using (84) leads to

$$\frac{\partial H}{\partial t} + h_m\boldsymbol{\nabla}\cdot\rho_m(1-\phi)\mathbf{v}_m + h_f\boldsymbol{\nabla}\cdot\rho_f\phi\mathbf{v}_f + \rho_m(1-\phi)\mathbf{v}_m\cdot\boldsymbol{\nabla}h_m + \rho_f\phi\mathbf{v}_f\cdot\boldsymbol{\nabla}h_f - \mathbf{g}\cdot\overline{\rho\mathbf{v}} = \boldsymbol{\nabla}\cdot\overline{k}\boldsymbol{\nabla}T. \tag{85}$$

Expanding and rearranging (84) we can write

$$\boldsymbol{\nabla}\cdot\rho_f\phi\mathbf{v}_f = -\boldsymbol{\nabla}\cdot\rho_m(1-\phi)\mathbf{v}_m + \Delta\rho\frac{\partial\phi}{\partial t}. \tag{86}$$

Substituting this into (85) and taking $\overline{k} = k$ to be constant gives

$$\frac{\partial H}{\partial t} + h_f\Delta\rho\frac{\partial\phi}{\partial t} - L\boldsymbol{\nabla}\cdot\rho_m(1-\phi)\mathbf{v}_m + \rho_m(1-\phi)\mathbf{v}_m\cdot\boldsymbol{\nabla}h_m + \rho_f\phi\mathbf{v}_f\cdot\boldsymbol{\nabla}h_f - \mathbf{g}\cdot\overline{\rho\mathbf{v}} = k\nabla^2 T, \tag{87}$$

where $L = h_f - h_m$ is the latent heat of melting, assumed to be constant.

Standard thermodynamic relations tell us how the enthalpy density changes with temperature and pressure,

$$\mathrm{d}h = c_P\mathrm{d}T + \rho^{-1}(1-\alpha T)\mathrm{d}P, \tag{88}$$

where c_P is the specific heat capacity, and α is the coefficient of thermal expansion. Hence we can write that

$$\begin{aligned}\boldsymbol{\nabla}h &= c_P\boldsymbol{\nabla}T + \rho^{-1}(1-\alpha T)\boldsymbol{\nabla}P,\\ &= c_P\boldsymbol{\nabla}T + (1-\alpha T)\mathbf{g},\end{aligned} \tag{89}$$

where we have assumed that the thermodynamic pressure is the static pressure, given by $\boldsymbol{\nabla}P = \rho\mathbf{g}$.

Substituting (89) into (87) for h_f and h_m, assuming $\alpha_f = \alpha_m = \alpha$, $c_P^f = c_P^m = c_P$, and extending the Boussinesq approximation such that $\rho_m = \rho_f = \rho$ we can write

$$\frac{\partial H}{\partial t} - \rho L\boldsymbol{\nabla}\cdot(1-\phi)\mathbf{v}_m + \rho c_P\overline{\mathbf{v}}\cdot\boldsymbol{\nabla}T - \rho\alpha T\mathbf{g}\cdot\overline{\mathbf{v}} = k\nabla^2 T. \tag{90}$$

This equation states that changes in the volumetric enthalpy are due to advection of latent heat, advection of sensible heat, changes in PV work by pressurisation, and diffusion of sensible heat.

Recall from your study of mantle convection that adiabatic flow creates a temperature gradient in the mantle that is given by

$$\frac{\mathrm{d}T}{\mathrm{d}z} = \frac{\alpha g T}{c_P}. \tag{91}$$

Let us therefore define a mantle potential temperature $\mathcal{T}$ as

$$T = \mathcal{T}\exp(\alpha g z/c_P). \tag{92}$$

Using this definition and neglecting terms containing $(\alpha g z_{\max}/c_P)^2 \ll 1$ we can rewrite equation (87) as

$$\boxed{\frac{\partial H}{\partial t} + \rho c_P \mathrm{e}^{\alpha g z/c_P}\overline{\mathbf{v}}\cdot\boldsymbol{\nabla}\mathcal{T} = \rho L\boldsymbol{\nabla}\cdot(1-\phi)\mathbf{v}_m + k\mathrm{e}^{\alpha g z/c_P}\nabla^2\mathcal{T}.} \tag{93}$$

This is the equation governing the evolution of volumetric enthalpy. We will see its use below.

We can write (93) in a more familiar form with a bit more work. First note that the definition of enthalpy tells us that

$$h = c_P(T - T_0) + P\left(\frac{1}{\rho} - \frac{1}{\rho_0}\right) + h_0, \tag{94}$$

where h_0 is the enthalpy density at $T = T_0, \rho = \rho_0$. The volumetric enthalpy can be written as

$$\begin{aligned} H &= \overline{\rho h} \\ &= \rho(\phi L + h_m). \end{aligned} \tag{95}$$

Combining (95) and (94), taking the time-derivative, and substituting for $\partial H/\partial t$ in equation (93) gives

$$\rho c_P\left(\frac{\partial \mathcal{T}}{\partial t} + \overline{\mathbf{v}}\cdot\boldsymbol{\nabla}\mathcal{T}\right) = -\mathrm{e}^{-\alpha g z/c_P}L\Gamma + k\nabla^2\mathcal{T}, \tag{96}$$

where we have simplified the latent heat term using the conservation of mass equation (9).

6.2 Conservation of species mass

Suppose that our thermochemical system is composed of N chemical components, each of which is a fundamental constituent with a conserved mass. Indexing these components with $i \in [1, N]$ we can represent the volume concentration of component i in phase j as $C_{i,j}$, where j can take values of f or m. Since the concentrations must sum to unity we can write:

$$\sum_{i=1}^{N-1} C_{i,j} + C_{N,j} = 1, \tag{97}$$

which shows that if we know the concentration of any $N-1$ components, we can obtain the last one by algebra. Hence, at most, we need $2(N-1)$ PDEs to enforce conservation of component mass.

The integral form of a pair of these equations reads

$$\frac{\mathrm{d}}{\mathrm{d}t}\int_{\mathrm{RVE}} \rho_f\phi C_{i,f}\mathrm{d}V = -\int_{\partial\mathrm{RVE}} \rho_f\phi\left(C_{i,f}\mathbf{v}_f - \mathcal{D}_i\boldsymbol{\nabla}C_{i,f}\right)\cdot\mathbf{dS} + \int_{\mathrm{RVE}} X_i\mathrm{d}V \tag{98a}$$

$$\frac{\mathrm{d}}{\mathrm{d}t}\int_{\mathrm{RVE}} \rho_m(1-\phi)C_{i,m}\mathrm{d}V = -\int_{\partial\mathrm{RVE}} \rho_m(1-\phi)C_{i,m}\mathbf{v}_m\cdot\mathbf{dS} - \int_{\mathrm{RVE}} X_i\mathrm{d}V, \tag{98b}$$

where X_i is the rate of mass-transfer of component i from the matrix to the magma and $\mathcal{D}_i$ is the diffusivity of component i in the magma. Mass transfer occurs through melting/freezing, as well as through reactive equilibration. For each component, there is separate melting rate Γ_i such that

$$\sum_{i=1}^{N} \Gamma_i = \Gamma.$$

Each component also has an equilibrium coefficient K_i, which relates the concentration in the fluid phase to the concentration in the matrix phase as

$$C_{i,m} = K_i C_{i,f}. \tag{99}$$

This coefficient may be a function of pressure and temperature. The reaction caused by disequilibrium is then written as

$$X_{R,i} = R_i(C_{i,m} - K_i C_{i,f}), \tag{100}$$

where R_i is a reaction-rate constant that could depend on porosity, pressure, and temperature, and we have assumed linear reaction kinetics. Since we interpret these reactions to be mass neutral, unlike the melting reactions, we require that

$$\sum_{i=1}^{N} R_i = 0.$$

Combining reaction and melting we have

$$X_i = \Gamma_i + R_i(C_{i,m} - K_i C_{i,f}). \tag{101}$$

Returning to equation (98) and using the usual technique, we can rewrite as a set of PDEs

$$\frac{\partial \phi C_{i,f}}{\partial t} + \boldsymbol{\nabla}\cdot \phi \mathbf{v}_f C_{i,f} = \frac{1}{\rho}\left[\Gamma_i + R_i(C_{i,m} - K_i C_{i,f})\right] + \mathcal{D}_i \boldsymbol{\nabla}\cdot \phi \boldsymbol{\nabla} C_{i,f}, \tag{102a}$$

$$\frac{\partial (1-\phi) C_{i,m}}{\partial t} + \boldsymbol{\nabla}\cdot (1-\phi) \mathbf{v}_m C_{i,m} = -\frac{1}{\rho}\left[\Gamma_i - R_i(C_{i,m} - K_i C_{i,f})\right], \tag{102b}$$

where we have made the Boussinesq approximation and taken the densities to be equal. Using the conservation of mass equations (8) and (9) we can simplify this as

$$\frac{\partial C_{i,f}}{\partial t} + \mathbf{v}_f \cdot \boldsymbol{\nabla} C_{i,f} = \frac{1}{\phi\rho}\left[\Gamma\left(C_{i,\Gamma} - C_{i,f}\right) + R_i(C_{i,m} - K_i C_{i,f})\right] + \mathcal{D}_i \boldsymbol{\nabla}\cdot \phi \boldsymbol{\nabla} C_{i,f}, \tag{103a}$$

$$\frac{\partial C_{i,m}}{\partial t} + \mathbf{v}_m \cdot \boldsymbol{\nabla} C_{i,m} = -\frac{1}{(1-\phi)\rho}\left[\Gamma\left(C_{i,\Gamma} - C_{i,m}\right) + R_i(C_{i,m} - K_i C_{i,f})\right], \tag{103b}$$

where $C_{i,\Gamma} = \Gamma_i/\Gamma$ is the mass-fraction of component i in the mass that is subtracted from the solid during melting (or added to it during freezing). These two equations state the changes in the composition of a phase at a point in space are due to advection of different composition onto that point, interphase transfer of mass by melting or freezing, and reactive equilibration between phases (and diffusion, for the liquid phase).

6.3 Thermodynamic equilibrium in a two-component system

Two key assumptions will allow us to simplify the rather complicated equations for conservation of components. They are rather restrictive in terms of limiting the realism of our petrological model, but they allow us to write down a system that is straightforward, if not easy, to solve. These assumptions are

Two components Although it is almost absurd, we assume that the mantle is composed of two components. There is really no way to map these onto real, chemical entities, so we'll simply refer to them as an *enriched* and a *depleted* end-member. A rock containing a more enriched composition (more of the enriched end-member) will melt at lower temperature than a less enriched (or more depleted) composition. Because we have only two components, we need only one equation per phase.

Thermodynamic equilibrium We also assume that the grain-scale reaction process between the melt and the matrix phases is sufficiently fast that the system is in thermodynamic equilibrium everywhere. This means that the fluid composition and the solid composition are always in a relationship that is given by the equilibrium distribution coefficient, K_i (or some other algebraic rule). Hence we only need to track the composition of one of the two phases. Or, equivalently, we can track the bulk composition. Another result of the assumption of thermodynamic equilibrium is that the phase fraction of melt (i.e. the porosity) is determined entirely by the local enthalpy and composition. Although we used the conservation of mass equations to derive our thermochemical PDEs, above, we will not be able to use them to model the evolution of porosity.

Applying these two assumptions, we can sum equations (102) and define $C = \phi C_{1,f} + (1-\phi) C_{1,m}$ as the bulk composition, giving

$$\boxed{\frac{\partial C}{\partial t} + \boldsymbol{\nabla} \cdot \overline{\mathbf{v} C} = \mathcal{D} \boldsymbol{\nabla} \cdot \phi \boldsymbol{\nabla} C_f.} \tag{104}$$

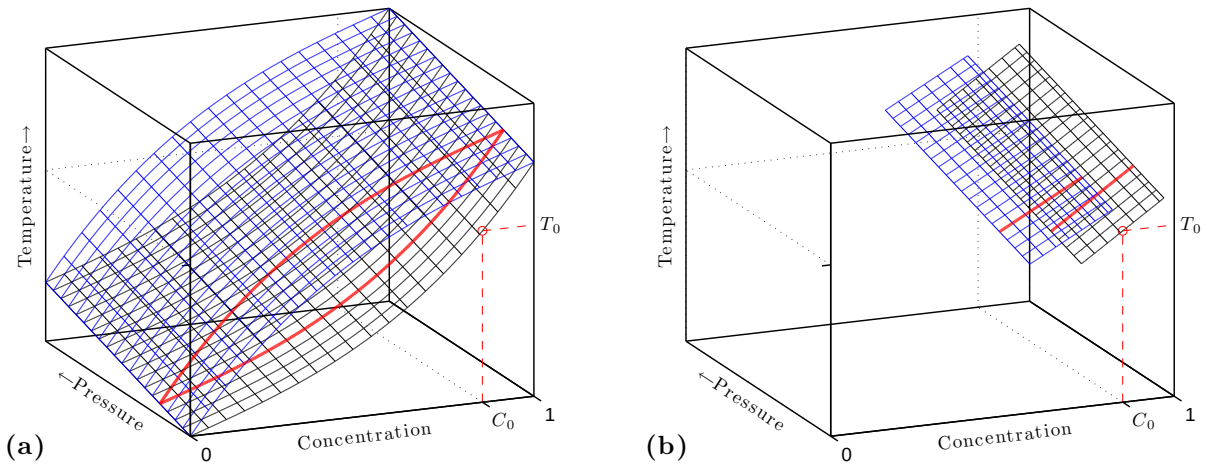

Figure 14: Phase diagrams for a binary system. Enriched compositions have low values of C, depleted compositions have high values of C. **(a)** Phase loop in the T–C-plane with a constant Clapeyron slope ($\gamma = \partial P / \partial T$). The solid red lines show a loop at constant pressure. **(b)** The phase loop has been linearised about some reference composition. Figure from Katz [2010].

Equations (93) and (104) provide a theoretical framework for conservation of energy and species mass in a two-phase, two-component system. Note, however, that to solve them, we need a means to calculate the temperature, porosity, and phase compositions as a function of the volumetric enthalpy H and the bulk composition C. This calculation must be based on a *phase diagram*, which shows the pressure–temperature–composition stability regions of different phases. A simple phase diagram, relevant for a two-component system, is shown in Figure 14a, and is simplified by linearising the compositional dependence, as shown in Figure 14b. We need

four equations to solve for the four unknowns (T, ϕ, C_f, C_m). One of these is the definition of bulk composition,

$$C = \phi C_f + (1-\phi)C_m; \tag{105}$$

a second one is the definition of bulk, volumetric enthalpy,

$$\begin{aligned} H &= \rho[\phi h_f + (1-\phi)h_m] \\ &= \rho\phi L + \rho c_P(T - T_0). \end{aligned} \tag{106}$$

In writing this definition of the bulk enthalpy, we have assumed that density is constant, and hence $1/\rho - 1/\rho_0 = 0$. We have also taken the reference enthalpy at T_0 to be zero, which we can do without loss of generality. The last two equations are the definitions of the liquidus and solidus. The solidus is the surface in P–T–C space across which the system goes from a purely solid system (below the solidus), to a partially molten system (above the solidus). The liquidus is the surface in the same space across which the system goes from partially molten to completely molten. The liquidus is at higher temperature than the solidus, and is represented by a blue mesh in Figure 14. The linearised surfaces in Figure 11b provide the simplest instance of these surfaces, given by

$$T = T_0 + M_S C_S + \gamma^{-1} P_l \tag{107a}$$

$$T = T_0 + M_L(C_L - \Delta C) + \gamma^{-1} P_l, \tag{107b}$$

where subscripts S, L represent the solidus and liquidus surfaces, respectively, M is the slope along the composition axis, and γ^{-1} is the slope along the pressure axis, which is given by the inverse of the Clausius-Clapeyron parameter. We assume that the pressure variation is controlled by the lithostatic pressure, $P_l = -\rho g z$, taking the z-direction as upward (i.e. $\hat{\mathbf{k}} \cdot \hat{\mathbf{g}} = -1$).

Equations (105), (106), and (107) are four equations for the four thermochemical unknowns, as a function of H and C. Determining their values by solving this set of equations is sometimes known as the Enthalpy method. Before finding the solutions, however, it is helpful to non-dimensionalise variables.

6.4 Entropy formulation and the melting rate

In assuming thermodynamic equilibrium, the melting rate is no longer explicit in our formulation. In fact, it is given implicitly by the system of PDEs and the phase constraints. It is possible unravel this implicit dependence and obtain an approximate expression for the melting rate. To do so, we return to equation (90), which reads

$$\frac{\partial H}{\partial t} - \rho L \boldsymbol{\nabla} \cdot (1-\phi)\mathbf{v}_m + \rho c_P \overline{\mathbf{v}} \cdot \boldsymbol{\nabla} T - \rho \alpha T \mathbf{g} \cdot \overline{\mathbf{v}} = k \nabla^2 T,$$

and seek to convert it to an equation for entropy, rather than enthalpy or temperature. Substituting for $\partial H/\partial t$, as we did above to obtain (96), neglecting diffusion, and rearranging gives

$$\rho c_P \frac{\partial T}{\partial t} + L\Gamma + \rho \overline{\mathbf{v}} \cdot [c_P \boldsymbol{\nabla} T - \alpha T \mathbf{g}] = 0. \tag{108}$$

To bring the thermodynamic entropy into this equation, we use $L = T\Delta S = T(S_f - S_m)$ and the relationship

$$\begin{aligned} \mathrm{d}S &= \frac{c_P}{T}\mathrm{d}T - \frac{\alpha}{\rho}\mathrm{d}P \\ &= \frac{c_P}{T}\mathrm{d}T + \alpha g \mathrm{d}z, \end{aligned} \tag{109}$$

where S is the specific entropy, with units of J/kg/K, and we have assumed a lithostatic pressure with $\hat{\mathbf{k}} \cdot \hat{\mathbf{g}} = -1$. Now we can treat each term of (108) separately,

$$\rho c_P \frac{\partial T}{\partial t} = \rho T \left[(1-\phi) \frac{\partial S_m}{\partial t} + \phi \frac{\partial S_f}{\partial t} \right], \tag{110a}$$

$$\rho \overline{\mathbf{v}} \cdot [c_P \boldsymbol{\nabla} T - \alpha T \mathbf{g}] = \rho T \left[(1-\phi) \mathbf{v}_m \cdot \boldsymbol{\nabla} S_m + \phi \mathbf{v}_f \boldsymbol{\nabla} S_f \right], \tag{110b}$$

$$L\Gamma = \rho T \left[S_f \left(\frac{\partial \phi}{\partial t} + \boldsymbol{\nabla} \cdot \phi \mathbf{v}_f \right) - S_m \left(\frac{\partial (1-\phi)}{\partial t} + \boldsymbol{\nabla} \cdot (1-\phi) \mathbf{v}_m \right) \right], \tag{110c}$$

where we have used (109) and the conservation of mass equations (8) and (9). Substituting each of these back into equation (108) and rearranging gives us

$$\frac{\partial}{\partial t} \left[(1-\phi) S_m + \phi S_f \right] + \boldsymbol{\nabla} \cdot \left[(1-\phi) \mathbf{v}_m S_m + \phi \mathbf{v}_f S_f \right] = 0, \tag{111}$$

which shows that the bulk entropy is conserved (as long as we neglect irreversible processes such as diffusion). More importantly, however, is that since $S_m = S_f - \Delta S$, and $\partial(\Delta S)/\partial t = 0$, we can also write (108) as

$$\Gamma \Delta S + \rho \frac{\partial S_m}{\partial t} + \rho \overline{\mathbf{v}} \cdot \boldsymbol{\nabla} S_m = 0. \tag{112}$$

Similarly, since $C_m = C_f - \Delta C$, we can rewrite equation (104) as

$$-\Gamma \Delta C + \rho \frac{\partial C_m}{\partial t} + \rho \overline{\mathbf{v}} \cdot \boldsymbol{\nabla} C_m = 0. \tag{113}$$

To complete this calculation, we will need one more equation: the solidus phase-constraint (107a), cast in terms of entropy. To obtain it, we integrate (109) with $T \approx \mathcal{T}_0$ and rearrange to give

$$T - T_0 = \frac{\mathcal{T}_0}{c_P} \left(S_m - S_{m0} + \frac{\alpha}{\rho} P_l \right),$$

where $\mathcal{T}_0$ is the mantle potential temperature before melting begins, and S_{m0} is a reference entropy at $T = T_0$ and $P_l = 0$. Combining this with (107a) and taking the slopes of the solidus and liquidus as $M_S = M_L = M$ gives

$$S_m = S_{m0} + \frac{M c_P}{\mathcal{T}_0} C_m + \left(\frac{\gamma^{-1} c_P}{\mathcal{T}_0} - \frac{\alpha}{\rho} \right) P_l. \tag{114}$$

Finally, combining equations (112), (113), and (114) and rearranging we obtain

$$\boxed{\Gamma = \rho \overline{\mathbf{v}} \cdot \hat{\mathbf{k}} \left(\frac{\gamma^{-1} \rho g - \alpha g \mathcal{T}_0 / c_P}{M \Delta C + L / c_P} \right).} \tag{115}$$

Note that melting is driven by the *mean* upwelling rate times a constant coefficient. That coefficient increases with the Clapeyron slope γ^{-1}, and has a minor reduction due to adiabatic decompression. A steeper solidus slope, or larger difference between liquid and solid reduce the melting rate, as does the latent heat of melting.

6.5 Non-dimensionalisation

The temperature and composition variables are shifted and renormalised to give a clean-looking system of dimensionless equations. Their corresponding non-dimensional variables are

$$\theta = \frac{\mathcal{T} - T_0}{\Delta T}, \qquad \tilde{\theta} = \frac{T - T_0}{\Delta T}, \qquad \Theta = \frac{C}{\Delta C}, \tag{116}$$

where ΔC is the difference in composition between the liquidus and the solidus at the reference temperature and pressure ($T = T_0, P = 0$). The temperature difference is defined as $\Delta T = M_S \Delta C$. Then, to the scaling in (32), we add

$$[H] \sim \rho c_P \Delta T, \qquad [\overline{\mathbf{v}}] \sim \phi_0 w_0. \tag{117}$$

Substituting equation (116) and scaling variables using (32) and (117), the conservation of energy (93) and composition (104) equations become

$$\frac{\partial H}{\partial t} + \phi_0 \mathrm{e}^{\mathcal{A}z} \boldsymbol{\nabla} \cdot \overline{\mathbf{v}} \theta = \phi_0 \mathcal{S} \boldsymbol{\nabla} \cdot (1 - \phi_0 \phi) \mathbf{v}_m + \mathrm{Pe}_T^{-1} \mathrm{e}^{\mathcal{A}z} \nabla^2 \theta \tag{118}$$

$$\frac{\partial \Theta}{\partial t} + \phi_0 \boldsymbol{\nabla} \cdot \overline{\mathbf{v}\Theta} = \phi_0 \mathrm{Pe}_C^{-1} \boldsymbol{\nabla} \cdot \phi \boldsymbol{\nabla} \Theta_f, \tag{119}$$

where we have introduced four new dimensionless numbers: $\mathcal{A} = \alpha g \delta / c_P$ is the adiabatic parameter and controls the adiabatic gradient, $\mathcal{S} = L/(c_P M_S \Delta C)$ is the Stefan number and controls the importance of changes in latent heat, $\mathrm{Pe}_T = w_0 \delta / \kappa$ is the thermal Peclet number and controls the importance of thermal diffusion, and $\mathrm{Pe}_C = w_0 \delta / \mathcal{D}$ is the compositional Peclet number and controls the importance of chemical diffusion.

Non-dimensionalising equations (105), (106), and (107) gives

$$\Theta = \phi_0 \phi \Theta_f + (1 - \phi_0 \phi) \Theta_m, \tag{120}$$

$$H = \phi_0 \mathcal{S} \phi + \tilde{\theta}, \tag{121}$$

$$\Theta_S = \tilde{\theta}_S + G^{-1} z, \tag{122}$$

$$\Theta_L = \mathcal{M} \left(\tilde{\theta}_L + G^{-1} z \right) - 1. \tag{123}$$

In this set of equations we have introduced another two dimensionless parameters: $G = \gamma M_S \Delta C / (\rho g \delta)$ is the dimensionless variation in solidus pressure with temperature, and $\mathcal{M} = M_S / M_L$ is the ratio of the solidus and liquidus slopes. Taking $\mathcal{M} = 1$, we can combine these four equations to obtain

$$\phi = \frac{H - \Theta + G^{-1} z}{\phi_0 (1 + \phi_0 \mathcal{S})}, \tag{124}$$

which applies when $0 < (H - \Theta + G^{-1} z) < 1 + \phi_0 \mathcal{S}$, i.e. when the system is partially molten. The other thermochemical variables, $\theta, \Theta_f, \Theta_m$, can be calculated by substituting equation (153a) into equations (121)–(123). The relationship between non-dimensional temperature $\tilde{\theta}$ and non-dimensional potential temperature θ is given by

$$\tilde{\theta} + \theta^* = (\theta + \theta^*) \mathrm{e}^{\mathcal{A}z}, \tag{125}$$

where $\theta^* = T_0 / (M_S \Delta C)$.

Further reading As with much of this subject, nearly everything was laid out in McKenzie [1984]. After that, few authors touched the energy equation until recently. A derivation in concert with the damage formulation of two-phase mechanics was produced in Bercovici and Ricard [2003]. The enthalpy method was adapted from metallurgy to magma dynamics by Katz [2008], though it is not different from the approach used by Ribe [1985a] in column models. Other authors have re-derived the energetics of magma/mantle dynamics in the context of column models. These include Sramek et al. [2007] and Hewitt and Fowler [2008]. The entropy formulation that is given above comes from Hewitt [2010].

7 Melting column models

Our goal, in this section, is to develop simple, one-dimensional solutions to the governing equations for a vertical column of mantle that is upwelling toward the surface. In this column, the magma and mantle upwelling rates will be represented as $w(z)$ and $W(z)$, respectively. At some depth z_0 representing the base of the melting region, where the porosity is zero, the mantle upwells with speed W_0. Since $\hat{\mathbf{k}}$ points upward, all of these speeds are positive. Using this information, and making the Boussinesq approximation $\rho_f = \rho_m = \rho$ we can sum the conservation of mass equations and integrate to obtain

$$\phi w + (1-\phi)W = W_0, \tag{126}$$

which states that the mass flux through the column at any depth is equal to the mass flux into the base of the column.

Since the rates of thermal and chemical diffusion in the mantle are rather small, we can ignore them and simplify the dimensional conservation of energy and composition equations to

$$\rho c_P \left(\frac{\partial T}{\partial t} + [\phi w + (1-\phi)W] \frac{\partial T}{\partial z} \right) = -L\Gamma - \rho \alpha g [\phi w + (1-\phi)W] \mathcal{T}_0, \tag{127}$$

$$\frac{\partial}{\partial t}[\phi C_f + (1-\phi)C_m] + \frac{\partial}{\partial z}[\phi w C_f + (1-\phi) W C_m] = 0, \tag{128}$$

where $\mathcal{T}_0$ is the potential temperature of the mantle column before it begins to melt. Under this simplification, the adiabatic temperature profile beneath the melting region is given by

$$T_a(z) = \mathcal{T}_0 - \frac{\alpha g \mathcal{T}_0}{c_P} z. \tag{129}$$

For simplicity we'll assume the linearised solidus and liquidus, with the same slope for both, $\mathcal{M} = 1$. Thus we can write

$$T_S = T_0 - \gamma^{-1} \rho g z + M C_S, \qquad C_L = C_S - \Delta C. \tag{130}$$

The depth of initial melting is then computed by finding the depth z_0 at which the adiabatic temperature is equal to the solidus temperature. Equating T_S and $T_a(z)$ gives

$$z_0 = \frac{T_0 + M C_0 - \mathcal{T}_0}{\gamma^{-1} \rho g - \alpha g \mathcal{T}_0 / c_P}. \tag{131}$$

Having obtained this depth, we can restrict our domain of interest to the range $z_0 \le z \le 0$.

Let's seek a steady-state solution for the column ($\partial \cdot / \partial t = 0$), applying the boundary conditions

$$W = W_0,\ C = C_0,\ \phi = 0, \text{ and } T = \mathcal{T}_0 + \frac{\alpha g \mathcal{T}_0}{c_P} z, \quad \text{at } z = z_0. \tag{132}$$

Integrating equation (128) gives

$$\phi w C_f + (1-\phi) W C_m = W_0 C_0. \tag{133}$$

Combining equations (126) and (133) gives an equation for the magmatic flux ϕw at any height in the column,

$$\phi w = W_0 F = W_0 \frac{C_m - C_0}{C_m - C_f} = W_0 (C_m - C_0)/\Delta C, \tag{134}$$

where F is defined to be the *degree of melting*. It can be graphically interpreted using the lever rule: the numerator is the distance between the initial bulk composition and the current

solid composition, the denominator is the distance between the solid and liquid compositions. Conservation of fluid mass at steady state gives us $\Gamma = \rho W_0 \mathrm{d}F/\mathrm{d}z$. To calculate $F(z)$, we substitute this expression for Γ along with equation (126) into the temperature equation (127) to obtain

$$c_P \frac{\partial T}{\partial z} + L \frac{\partial F}{\partial z} + \alpha g \mathcal{T}_0 = 0,$$

which can be integrated with the boundary condition for T in (132) to give

$$LF + c_P(T - \mathcal{T}_0) + \alpha g \mathcal{T}_0 z = 0. \tag{135}$$

Now we can combine equations (135), (132), (130), and the definition $F = (C_m - C_0)/\Delta C$, and with some laborious algebra we obtain

$$F(z) = \frac{\gamma^{-1}\rho g - \alpha g \mathcal{T}_0 / c_P}{L/c_P + M\Delta C}(z - z_0), \tag{136}$$

an equation that bears a close resemblance (unsurprisingly) with (115).

We can see from equation (136) that the degree of melting increases linearly with distance up the melting column $z - z_0$. In the denominator, the first term represents the latent-heat cost of melting, while the second term represents the change increase in solidus temperature with progressive melting. Increasing the latent heat and the compositional dependence of the solidus both produce lower degrees of melting. In the numerator, the first term represents the decreasing solidus temperature with distance up the column, while the second term represents the decrease in temperature due to adiabatic decompression. The former drives melting while the latter reduces it.

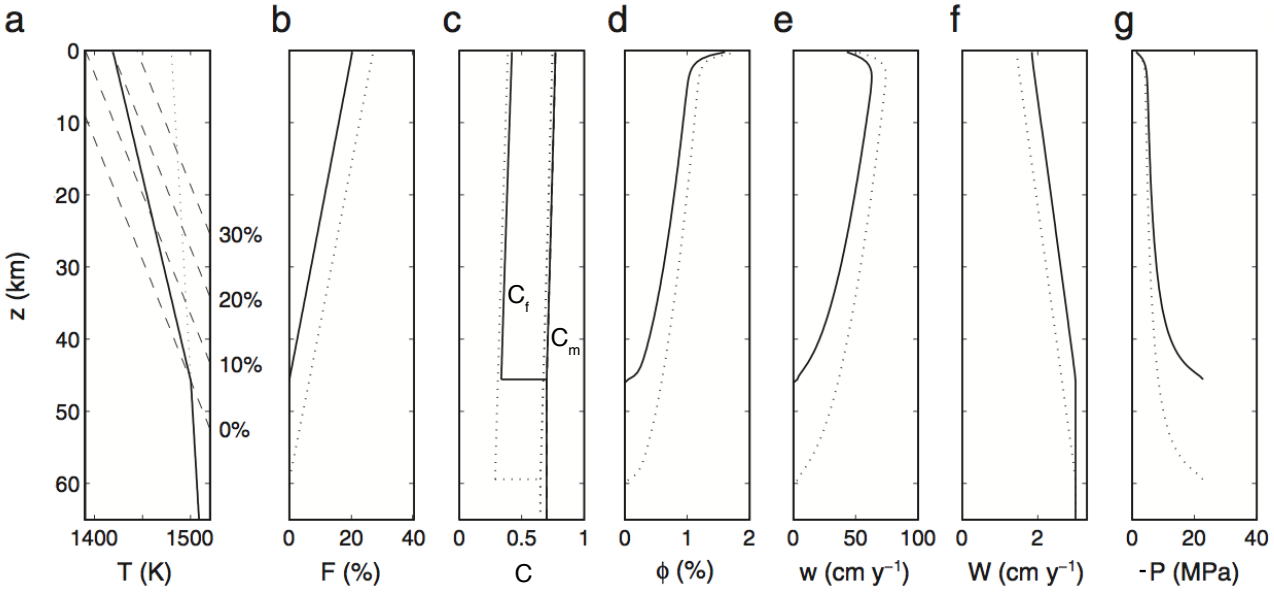

Figure 15: Numerical solution for a one-dimensional column of mantle that is upwelling and melting. Each panel shows a different variable. Parameter values are $W_0 = 3.2$ cm/yr, $\mathcal{T}_0 = 1480$ K, $C_0 = 0.7$, $\rho = 3000$ kg/m^3, $\Delta\rho = 500$ kg/m^3, $K_0 = 4 \times 10^{-9}$ m^2, $\mu = 10$ Pa-sec, $\eta = 10^{19}$ Pa-sec, $L = 3 \times 10^5$ J/kg, $c_P = 1000$ J/kg/K, $\alpha = 3 \times 10^{-5}$ K^{-1}, $\gamma = 10^{-7}$ K/Pa, and $M = 600$ K. Dotted line in (b)–(g) has $C_0 = 0.65$. **(a)** Temperature as a function of depth. Dashed lines are contours of F. Dotted line is adiabatic trajectory without melting. **(b)** Degree of melting. **(c)** Solid and liquid composition. **(d)** Porosity. **(e)** Magma flow speed. **(f)** Matrix flow speed. **(g)** Compaction pressure. Figure from Hewitt [2010].

Approximate solutions can be found for other variables by noticing that in most of the upwelling column $W \ll w$, and by assuming that melt extraction is dominantly driven by

buoyancy, rather than gradients in the compaction pressure. Starting with the dimensional equation of momentum conservation for the fluid in one dimension,

$$\phi(w - W) = \frac{K_0 \phi^n}{\mu} \left(\frac{\partial \mathcal{P}}{\partial z} + \Delta \rho g \right),$$

where we have taken $K = K_0 \phi^n$, and applying these assumptions gives

$$\phi w \approx \frac{K_0 \Delta \rho g \phi^n}{\mu}. \tag{137}$$

We can use $\phi w = W_0 F$ to obtain

$$\phi \approx \left[\frac{\mu}{K_0 \Delta \rho g} \right]^{1/n} (W_0 F)^{1/n}, \tag{138}$$

$$w \approx \left[\frac{\mu}{K_0 \Delta \rho g} \right]^{1/n} (W_0 F)^{(n-1)/n}, \tag{139}$$

$$W \approx W_0 (1 - F). \tag{140}$$

If we take $n = 3$, we see that porosity increases up the column, but only proportional to $z^{1/3}$, and the melt flow speed increases with $z^{2/3}$, even though the melt fraction increases with z. This is because of the nonlinear relationship between porosity and permeability, which allows for the rapid extraction of melt. These relationships are illustrated in more detail in Figure 15, which shows two numerical solutions to the governing equations. Parameter values are given in the figure caption.

It is worth looking at the 1D porosity profile (Figure 15d) in more detail, and thinking a bit about scaling. Note that it has three distinct segments: one at the bottom, where porosity increases sharply, one in the middle, where it increases gradually, and one at the top, where it again increases sharply. Recall that the compaction length is the length-scale over which perturbations in the compaction pressure decay; this is what sets the size of the upper and lower boundaries. Let's consider the bottom boundary. Here the porosity grows by melting, and is transported upward by advection. The compaction pressure transmits the "information" about this porosity gradient, and the impermeable barrier at its base, upward through the column, for about one compaction length. In that distance, the compaction pressure gradient balances the buoyancy force driving segregation, so $\partial \mathcal{P}/\partial z \approx 1$, from the compaction equation (37). Then, from Darcy's law (39), these two forces cancel and there is no driving force for segregation! Hence the compaction rates is $\partial W/\partial z \approx 0$, and we can rewrite the steady-state mass conservation equation (35) as

$$\frac{\partial \phi}{\partial z} \approx \frac{\Gamma}{\phi_0 W},$$

so the change in porosity with height in this boundary layer is simply due to melting, with no melt segregation.

Above this boundary layer, far from the impermeable barrier and the rapid change in porosity, the balance shifts. The gradient in compaction pressure becomes small, and no longer balances the buoyancy force. So the buoyancy force drives segregation of magma. This segregation is resisted by the Darcy drag on the grains (the interphase force $\mathbf{I}$). So the balance in the bulk of the column is given by Darcy's law; melt segregates under buoyancy, the porosity is roughly constant, and the melting rate balances the compaction rate,

$$\frac{\partial W}{\partial z} \approx -\frac{\Gamma}{(1 - \phi_0 \phi)}.$$

Not much can happen in one dimension, due to the constraint that all the mass in the column must travel vertically. The consequence of this is that the degree of melting at the top of the column is equal to what would be predicted by the batch melting equation. Adding magma transport apparently didn't gain much! But things get more interesting next.

Further reading Melting column models go back at least to Turcotte and Ahern [1978], Ahern and Turcotte [1979] and McKenzie [1984], with excellent treatment by Ribe [1985a]. More recently, Sramek et al. [2007] developed sophisticated treatment for a one-component system, as did Hewitt and Fowler [2008]. This was extended by Hewitt [2010], which is the basis for much of the discussion in the section above.

8 Disequilibrium reactive flow and channellisation

What are we missing if we just study the one dimensional melting column? One indication comes from observations of the Oman ophiolite, a vast exposure of rocks that were previously in the mantle, beneath a spreading centre. The ophiolite is primarily composed of dunites (almost pure olivine), and harzburgites (orthopyroxene and olivine). Interesting, the dunites form tabular bands that seem to align with the contemporaneous direction of gravity. Figure 16 is a photo-mosaic of an outcrop showing dunite bands.

Figure 16: A photo-mosaic of an outcrop of the Oman ophiolite. Light coloured bands are dunite; dark coloured bands are harzburgite. Image from Braun and Kelemen [2002].

The geological interpretation is that magma ascending through the mantle from deeper depths reacts as it rises, dissolving harzburgite and precipitating olivine. This can be understood by considering the linearised solidus (107a) and assuming constant temperature; there is then a relationship between pressure and concentration that melts coexisting with solid mantle must follow. Decreasing pressures mean increasing solubility of SiO_2 in the melt. Since harzburgite is a more silica-rich mineral than Olivine, the melting occurs by the following melting reaction

$$\text{Melt}_1 + \text{Pyroxene} + \text{Spinel} \Rightarrow \text{Melt}_2 + \text{Olivine}. \tag{141}$$

We won't be worried here about the spinel contribution to this reaction, and we won't focus on the chemical details, but will rather use this reaction to motivate a simple model of *reactive flow* with disequilibrium melting. In this model, the porosity will not be computed by assuming thermodynamic equilibrium, but rather with the conservation of mass equation (9), where Γ is given by the reactive melting rate (also called the dissolution rate). We can guess that this rate would be related to the distance from thermodynamic equilibrium: how *undersaturated* is the magma in SiO_2 as it rises. A simple assumption is that the melting rate is linearly proportional to this undersaturation. Hence we can write it as

$$\Gamma = RA(C_f^{eq} - C_f), \tag{142}$$

where R is a reaction-rate coefficient, and A represents the surface area per unit volume on which reaction can occur. More about these coefficients later. We have assumed a two-component system in writing (142), where SiO_2 is one of the components (the one represented by C_f), and the other component, representing all the other stuff in the magma, is given by $1 - C_f$.

In the model of reactive flow that we develop here, we neglect to solve for conservation of energy, and assume that within the melting region, the temperature is approximately isothermal (which we saw in the previous section is not the case). The important equations are the statements of conservation of species mass, which now take the dimensionless form

$$\frac{\partial C_m}{\partial t} + \mathbf{v}_m \cdot \boldsymbol{\nabla} C_m = \frac{-\phi_0}{1 - \phi_0 \phi}(C_R - C_m)\Gamma, \tag{143a}$$

$$\frac{\partial C_f}{\partial t} + \mathbf{v}_f \cdot \boldsymbol{\nabla} C_f = \frac{1}{\mathrm{Pe}_C}\nabla^2 C_f + \frac{1}{\phi}(C_R - C_f)\Gamma, \tag{143b}$$

where C_R is the concentration of SiO_2 in the product of the melting reaction, the magma that gets generated by reactive melting. In general C_R is not equal to either C_f or C_m. These equations state that changes in concentration of a phase are due to advection by that phase and reactive melting; diffusion also causes changes to the liquid phase. Note that there is a singularity in the magma concentration equation at $\phi = 0$. Note also that we have approximated $\boldsymbol{\nabla} \cdot \phi \boldsymbol{\nabla} C_f$ as $\phi \nabla^2 C_f$.

In this model we'll assume that the mantle matrix is static (not upwelling) except for compaction, and hence we can use the Helmholtz decomposition of equation (56), but throw out ψ and retain just $\mathbf{v}_m = \boldsymbol{\nabla}\mathcal{U}$. With this restriction, non-dimensional governing equations for the mechanics are written as

$$\frac{\partial \phi}{\partial t} - \phi_0^{-1} \boldsymbol{\nabla} \cdot (1 - \phi_0 \phi)\mathbf{v}_m = \Gamma, \tag{144a}$$

$$\nabla^2 \mathcal{U} = \frac{\mathcal{P}}{\xi}, \tag{144b}$$

$$-\boldsymbol{\nabla} \cdot (\phi^n \boldsymbol{\nabla} \mathcal{P}) + \frac{\mathcal{P}}{\xi} = -\boldsymbol{\nabla} \cdot \phi^n \hat{\mathbf{k}}, \tag{144c}$$

$$\phi \mathbf{v}_f = \phi \mathbf{v}_m - \phi^n \left[\boldsymbol{\nabla} \mathcal{P} - (1 - \phi_0 \phi)\hat{\mathbf{k}}\right], \tag{144d}$$

where $\xi = \zeta + 4\eta/3$ and $\hat{\mathbf{k}}$ points upward (opposite the direction of gravity), as usual.

To complete the model, we need to specify the equilibrium solubility as a function of pressure C_f^{eq}, and the concentration of SiO_2 in the reaction product C_R. The former can be approximated as a linear profile, given in dimensionless terms as

$$C_f^{eq}(z) = \beta z, \tag{145}$$

where we have taken the pressure to be lithostatic and replaced it with height through the domain. $\beta = b\rho g \delta$ is the dimensionless change in solubility per compaction length, and b is

the change in solubility per Pascal of pressure. One choice for concentration in the reaction product is as follows

$$C_R = C_f^{eq} + \alpha, \tag{146}$$

where α is an offset from the equilibrium solubility.

We can gain some insight into the reactive flow process by considering a steady-state version of equation (143b) with no diffusion ($\mathrm{Pe}_C \to \infty$), and approximating $C_R - C_f \approx \alpha$ and $\boldsymbol{\nabla} C_f \approx \beta \hat{\mathbf{k}}$. Substituting and rearranging gives

$$\Gamma \sim \frac{\phi w \beta}{\alpha}. \tag{147}$$

This shows that the reactive melting rate is driven by the flux of magma ϕw up a solubility gradient β. A larger α, equivalent to a greater compositional difference between the fluid concentration and the reaction-product concentration, means that less melt must be produced to reattain equilibrium. This shows why reactive melting is sometimes called *flux melting*—it is driven by the flux of magma from below. This also suggests the possibility of an instability: if the flux is higher at a point in the domain, more melting will occur there, and in the column above it. This melting will lead to a higher magmatic flux through the column above. Below we demonstrate the existence and nature of this channellisation instability using linearised stability analysis and numerical simulations.

8.1 Linearised stability analysis

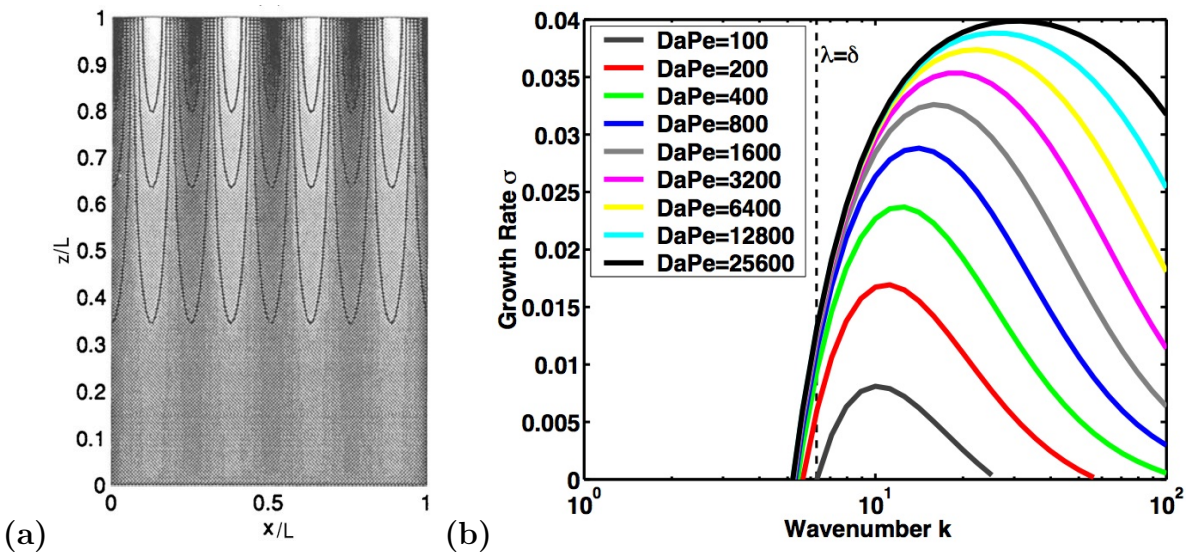

Figure 17: Linearised stability analysis of the reactive flow problem. **(a)** Example perturbation solution for porosity. The domain is one compaction length along each side, and hence the dimensionless wavelength is $\lambda = 1/4$, and the wavenumber is $k = 2\pi/\lambda = 8\pi$. Panel from Aharonov et al. [1995]. **(b)** The growth rate of perturbations in a linearised stability analysis of the reactive flow problem. Panel from Spiegelman et al. [2001].

As we hinted at above, there is a feedback between porosity, flux, and melting: a region of higher porosity has higher permeability, and can therefore accommodate a greater flux; a larger flux leads to more rapid reactive melting according to equation (147), and this leads to higher porosity. This feedback causes an instability, called the Reactive Infiltration Instability, that we will consider now.

Consider a set of high and low porosity bands that are oriented along the direction of gravity, as a perturbation to a uniform porous flow in a 2D domain, as shown in Figure 17a. The high porosity bands will have more reactive melting, and hence a higher flux, and should grow. The low porosity bands will have lower flux, and should shrink. Assuming an approximate ("quasi") steady-state, and that the porosity everywhere is rather small, we can write the conservation of mass equation as $\boldsymbol{\nabla}\cdot\mathbf{v}_m \approx -\Gamma$. Then, using $\boldsymbol{\nabla}\cdot\mathbf{v}_m = \nabla^2\mathcal{U}$, we can write the continuity equation as

$$\frac{\mathcal{P}}{\xi} \approx -\Gamma. \tag{148}$$

This means that where the melting rate is high, the compaction pressure will be low; magma should flow out of the low porosity areas into the high porosity areas... if the gradient is on the scale of the compaction length! So this helps us to explain the existence of an instability.

What is the growth rate of the instability? A linearised stability analysis (not shown here) predicts the curves in Figure 17b. The wavenumber k is the number of full wavelengths in the x-direction, *per compaction length*. The vertical dashed line indicates the wavenumber $k = 2\pi$ corresponding to a wavelength that is equal to the compaction length. Wave-numbers larger than 2π (wavelengths smaller than the compaction length) grow, those smaller than 2π do not. So again we see that the compaction length controls the length-scale of magmatic processes.

8.2 Numerical models

Numerical solutions provide a more detailed picture of the reactive flow process. Figure 18a shows a schematic diagram of the computational domain. Melt flows into the bottom with dimensionless flux of $\phi w = 1$, and passes through an unreactive zone before entering the reactive zone. The solid composition is initially set to $C_m = 0.95$ with a very small white noise on the grid scale (this is not a realistic representation of the SiO_2 content, obviously!). Melt is free to flow out of the top of the domain. Panel (b) shows the equilibrium solubility C_f^{eq} as a function of height through the domain.

To obtain the full, dimensionless model, we must write the non-dimensional form for the melting rate. Using the scalings proposed above this becomes

$$\Gamma = \mathrm{Da}A(C_f^{eq} - C_f), \tag{149}$$

where

$$\mathrm{Da} = \frac{R\delta}{\phi_0 w_0 \rho} \tag{150}$$

is the Damköhler number, the ratio of the advective time-scale for melt to travel across one compaction length to the reaction time-scale. Large Damköhler numbers mean that the system advects rapidly and is hence further from equilibrium, small Damköhler number means that the system reacts rapidly and is close to equilibrium. Substituting the reaction rate, equilibrium profile, and $C_R = 1$ into (143) gives

$$\frac{\partial C_m}{\partial t} + \mathbf{v}_m\cdot\boldsymbol{\nabla}C_m = \frac{-\phi_0\mathrm{Da}}{1-\phi_0\phi}(1-C_m)A(\beta z - C_f), \tag{151a}$$

$$\frac{\partial C_f}{\partial t} + \mathbf{v}_f\cdot\boldsymbol{\nabla}C_f = \frac{1}{\mathrm{Pe}_C}\nabla^2 C_f + \frac{\mathrm{Da}}{\phi}(1-C_f)A(\beta z - C_f), \tag{151b}$$

where the non-dimensional area of reaction is

$$A = \frac{C_m(1-\phi_0\phi)}{(1-\phi_0)}.$$

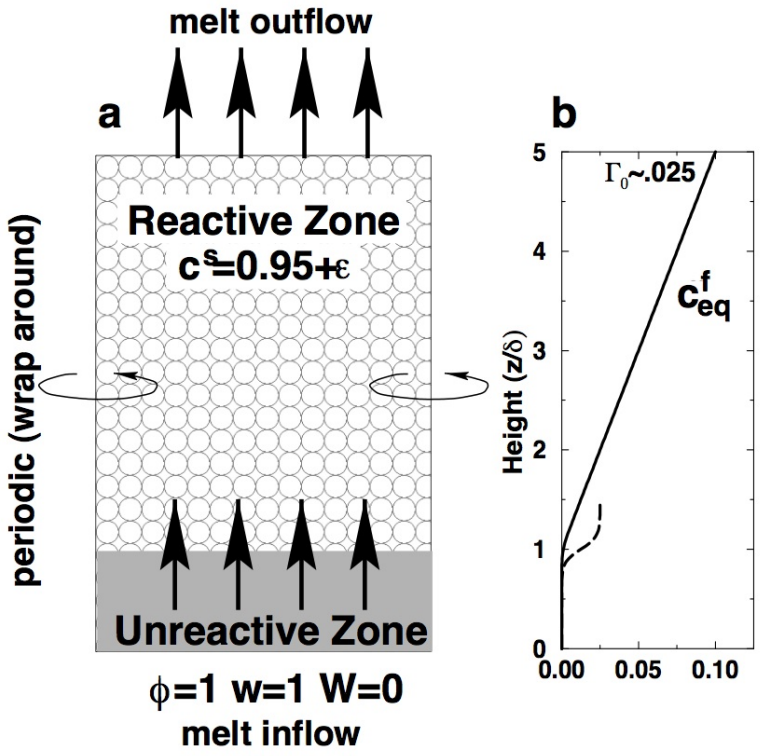

Figure 18: Reactive flow domain and solubility gradient. **(a)** A schematic diagram of the computational domain with an unreactive zone of one compaction length in height at the base. The side boundaries are periodic. **(b)** The imposed solubility gradient in the domain. Equilibrium concentration is on the x-axis. Figure from Spiegelman et al. [2001].

These equations (151), for the concentration of the soluble component in the liquid and solid, combined with equations (144), are solved numerically to produce simulations of reactive flow.

The details of the numerical solution are not considered here, but we will discuss the results. The model has two important control parameters, that determine the character of the solution: the Damköhler number and the compositional Peclet number. The former determines the rate of reaction relative to advection; large Da means the system rapidly reacts to restore equilibrium, and hence is never far from equilibrium. The latter determines the rate of diffusion relative to advection; large Pe_C means that chemistry does not diffuse rapidly, and effectively follows the magmatic flow. To begin our discussion, we consider a set of $\mathrm{Da}, \mathrm{Pe}_C$ that are large enough to produce dissolution channels.

Figure 19 shows the evolution of porosity for a simulation in which $\mathrm{Da} = 40$ and $\mathrm{Pe}_C = 40$. Channels form after a rather long initial phase when porosity remains stable (t is the non-dimensional time, with 1 time-unit corresponding to the time for a parcel of magma to traverse the domain vertically). Channels emerge from the background at about $t = 44$ and then evolve more rapidly into a coalescing network. By $t = 116$, channels have reached a porosity near 4 per cent, while the interchannel regions have compacted down to 0.1%. Melt from the interchannel regions is mostly extracted laterally into the channels, where it rises rapidly through the domain.

The porosity result at $t = 116$ is repeated in Figure 20, along with contemporaneous plots of the dissolution rate Γ, the solid concentration C_m, and the fluid concentration C_f. The dissolution rate is largest in the channels, where the flux is high, and smallest between channels, where the flux is nearly zero. This leads to the chemical depletion of the channels, as shown in the solid concentration field. The fluid concentration appears nearly uniform in the x-direction, and mirrors the gradient in the equilibrium concentration in z. Close inspection reveals vertical streaks where advection in the channels has smeared the vertical concentration upward, leading

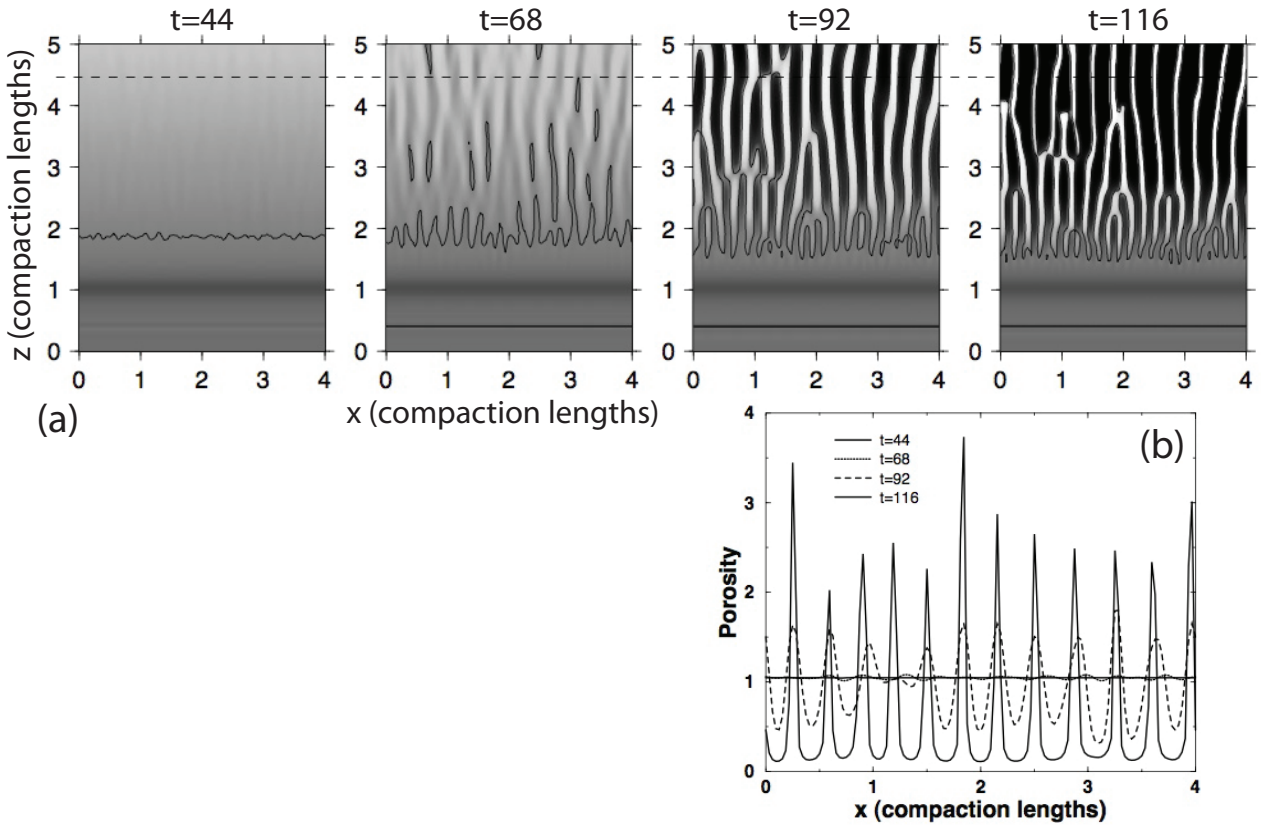

Figure 19: Porosity evolution in a reactive flow simulation with $\mathrm{Da} = \mathrm{Pe}_C = 40$. **(a)** The evolution of the porosity field through time. t is the non-dimensional time, equal to the time required to traverse the box once at the background porosity ϕ_0. The black line is a contour of porosity corresponding to 1% enhancement over the background. At $t = 116$, the maximum porosity is 3.9% while the minimum porosity is 0.1%, corresponding to a flux-difference of ∼1500 between channels and interchannels. **(b)** Cross section of porosity at $z = 4.5$ (dashed line in panel (a)). Interchannel regions decrease in porosity due to compaction; channels increase due to reactive melting. Adapted from Spiegelman et al. [2001].

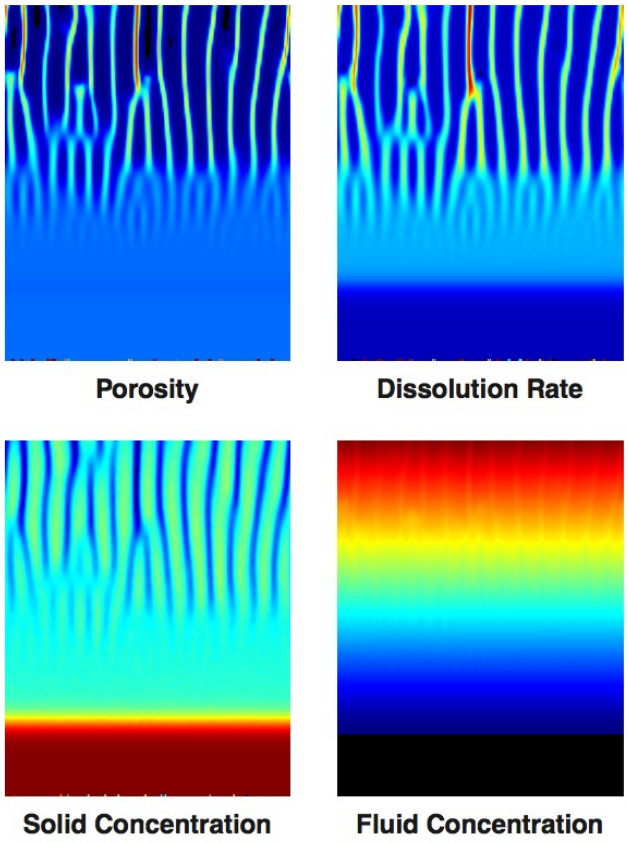

Figure 20: A snapshot from a simulation of reactive flow with $\mathrm{Da} = \mathrm{Pe}_C = 40$ at $t = 116$. Porosity as in Figure 19. Dissolution rate Γ is high in the channels, where the melt flux is high (see equation (147)). Solid concentration is lowest in the channels, where dissolution has depleted it. The fluid concentration is, to leading order, equal to the equilibrium concentration. It differs noticeably in the channels, where rapid advection drags fluid upward faster than it can react back to equilibrium, leading to rapid dissolution. Figure from Spiegelman et al. [2001].

to larger disequilibrium and higher dissolution rates.

What then, is the effect of varying the control parameters Da and Pe_C? As shown by the linearised stability analysis, to leading order their effects are the same, and what actually controls the system is the product DaPe_C. Figure 21 shows results from a suite of simulations with different values of the Da and Pe_C.

Is this a good model for the dunite bands that are observed in the Oman ophiolite? What other observational constraints can be brought to bear? What are the consequences for geochemistry? All of these questions have been addressed, to some extent, in the published literature. See below for references.

Further reading There is a large literature on the observational evidence for reactive flow in the mantle. Two early and oft-cited papers are Kelemen et al. [1992] and Kelemen et al. [1995a], regarding the ophiolite in Oman. More recent surveying of the Oman ophiolite by Braun and Kelemen [2002] and Braun and Kelemen [2002] has documented the spatial distribution of dunite bands.

The theoretical and computational literature on reactive flow as related to the mantle begins with Aharonov et al. [1995] (stability analysis) and Aharonov et al. [1997] (simulations). Spiegelman et al. [2001] produced more advanced numerical models, and revised the linearised stability analysis. Spiegelman and Kelemen [2003] explored the geochemical consequences of channelised melt transport, and this was extended to the uranium-series elements in Elliott and Spiegelman [2003]. Recently there has been some work coming out of the group of Yan Liang, such as Liang et al. [2010]. Liang and Parmentier [2010] represents a different approach, that takes channels for granted and parameterises them as a second porosity field with different permeability properties. This is somewhat similar to the work of Jull et al. [2002].

There are also some laboratory experiments that are relevant here. Analogue experiments include Kelemen et al. [1995b], and experiments on real rocks include Morgan and Liang [2003]

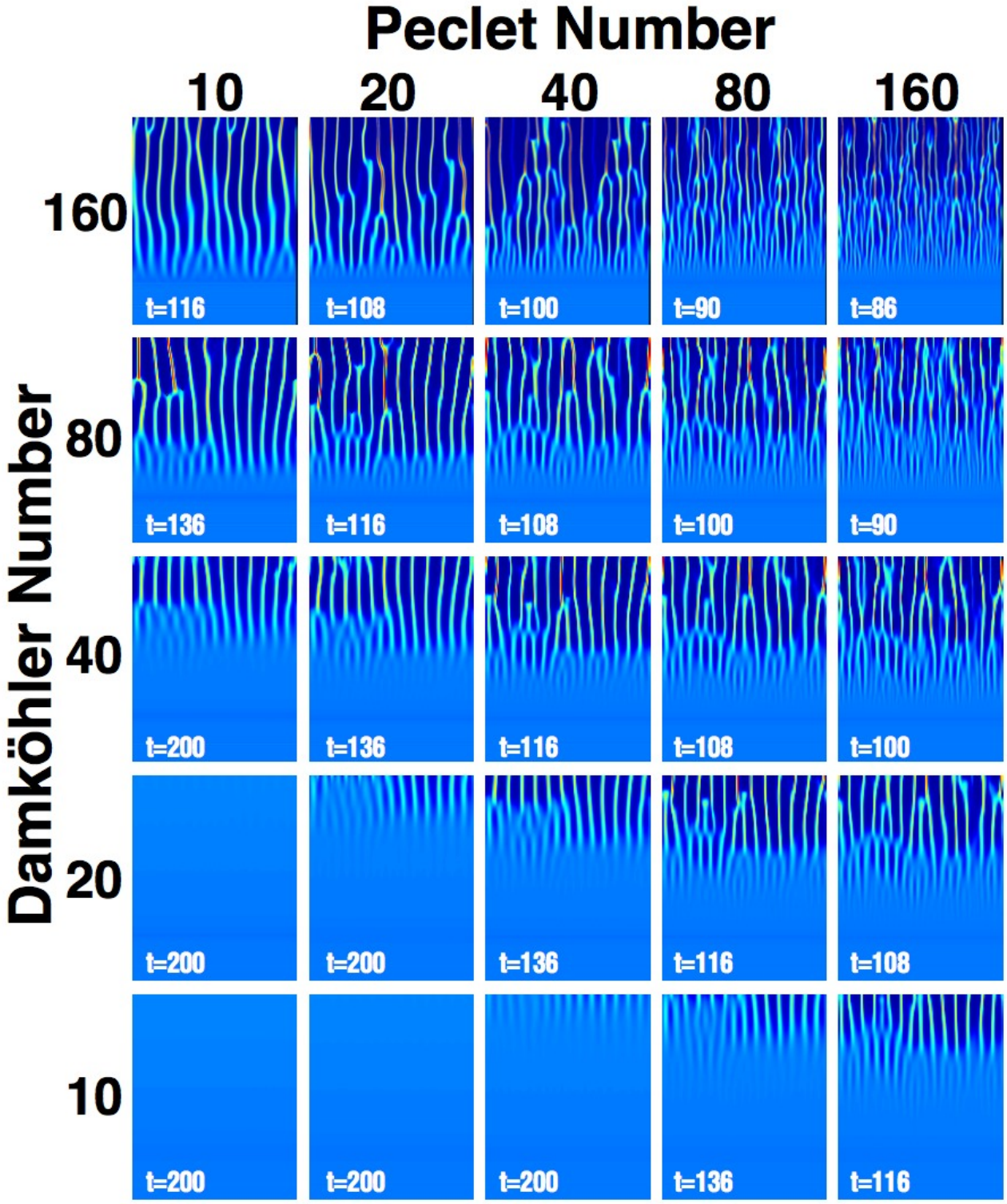

Figure 21: A suite of simulations for different values of Da and Pe_C. Times are shown for each panel. NW-SE diagonals on this figure have equal values of DaPe_C. Figure from Spiegelman et al. [2001].

and Morgan and Liang [2005].

9 Tectonic-scale models with equilibrium thermochemistry

We began these notes with a discussion of plate-boundary volcanism and asked about the source regions that feed magma to these volcanos. So far, however, our models haven't looked much like plate-tectonic boundaries. To come back to our initial goal, we return to the familiar ground of thermodynamic equilibrium. We'll make use of the Enthalpy method to calculate melting and porosity in a two-phase model of a mid-ocean ridge. In this section we will rely heavily on numerical models, the implementation of which will not be discussed. Further details can be found in the references. Dimensional values of model parameters are given in Table 1.

Quantity	symbol	range considered	preferred value	units
Half-spreading rate	U_0	0.5 – 7	3	cm/yr
Ridge-migration rate	U_m	0.5 – 7	U_0	cm/yr
Permeability const.	K_0	10^{-8} – 10^{-6}	10^{-7}	m^2
Permeability exponent	n		3	
Mantle shear visc. const.	η_0	5×10^{17} – 8×10^{19}	10^{18}	Pa-s
Reference viscous temp.	T_{η_0}		†	°C
Activation energy	E^*		3×10^5	J-mol.$^{-1}$
Viscosity constant	λ		27	
Mantle bulk visc. const.	ζ_0	10^{18} – 4×10^{19}	2×10^{19}	Pa-s
Magma viscosity	μ		1	Pa-s
Boussinesq density	ρ		3000	kg-m^{-3}
Boussinesq density diff.	$\Delta\rho$		500	kg-m^{-3}
Spec. heat capacity	c_P		1200	J-kg^{-1}-K^{-1}
Thermal diffusivity	κ		10^{-6}	m^2-s^{-1}
Coef. thermal exp.‡	α		3×10^{-5}	K^{-1}
Latent heat	L		4×10^5	J-kg^{-1}
Chemical diffusivity	$\mathcal{D}$		10^{-8}	m^2-s^{-1}
Potential temperature	$\mathcal{T}_0$		1375	°C
Reference melting temp.	T_0		1292	°C
Clapeyron slope	γ		60^{-1}	GPa-K^{-1}
Composition diff.	ΔC		0.1	wt. frac.
Solidus, liquidus slope	M_S, M_L		400	K-(wt. frac.)$^{-1}$

Table 1: Dimensional parameters used in the model and their preferred values. Footnotes: †The value of this parameter is chosen such that $\eta = \eta_0$ for potential temperature $\mathcal{T}_m$, composition C_0, and zero porosity, at the depth given by eq. (131). ‡The coefficient of thermal expansion is used to calculate the adiabatic temperature gradient but is not used in calculating variations in density for buoyancy terms.

To model melting and melt transport at a mid-ocean ridge, we need employ the full system of partial differential equations, with few or no further simplifications. Putting these together

into one system, in non-dimensional form we have

$$\boldsymbol{\nabla}\cdot\mathbf{v}_m = \frac{\mathcal{P}}{\xi}, \qquad \text{Continuity equation,} \tag{152a}$$

$$-\boldsymbol{\nabla}\cdot\left(\phi^n\boldsymbol{\nabla}\mathcal{P}\right) + \frac{\mathcal{P}}{\xi} = \boldsymbol{\nabla}\cdot\left[\phi^n(\boldsymbol{\nabla}P - \hat{\mathbf{k}})\right], \qquad \text{Compaction equation,} \tag{152b}$$

$$\boldsymbol{\nabla}P = \boldsymbol{\nabla}\cdot\eta\left(\boldsymbol{\nabla}\mathbf{v}_m + \boldsymbol{\nabla}\mathbf{v}_m^T\right) + \phi\hat{\mathbf{k}}, \qquad \text{Stokes equation,} \tag{152c}$$

$$\frac{\partial H}{\partial t} + \mathrm{e}^{\mathcal{A}z}\boldsymbol{\nabla}\cdot\overline{\mathbf{v}}\theta = \mathcal{S}\boldsymbol{\nabla}\cdot(1-\phi)\mathbf{v}_m + \mathrm{Pe}_T^{-1}\mathrm{e}^{\mathcal{A}z}\nabla^2\theta, \qquad \text{Conservation of energy,} \tag{152d}$$

$$\frac{\partial\Theta}{\partial t} + \boldsymbol{\nabla}\cdot\overline{\mathbf{v}\Theta} = \mathrm{Pe}_C^{-1}\boldsymbol{\nabla}\cdot\phi\boldsymbol{\nabla}\Theta_f, \qquad \text{Conservation of species mass.} \tag{152e}$$

And we have an algebraic relation for the magma velocity,

$$\phi(\mathbf{v}_f - \mathbf{v}_m) = -\phi^n\left(\boldsymbol{\nabla}\mathcal{P} + \boldsymbol{\nabla}P - \hat{\mathbf{k}}\right), \qquad \text{Darcy's law.} \tag{152f}$$

In this system of equations, we have taken $\phi_0 = 1$ for simplicity of presentation, and without loss of generality.

This is a system of $4 + 2N_D$ equations for $4 + 2N_D$ principle variables,

$$\text{Principle variables: } \mathcal{P}, P, H, \Theta, \mathbf{v}_m, \mathbf{v}_f.$$

We need closure conditions for the rest of the symbols, including

$$\text{Closure variables: } \phi, \theta, \Theta_m, \Theta_f, \xi, \eta$$

and, of course, there is a set of dimensionless numbers that come from our choice of problem parameters

$$\text{Dimensionless numbers: } \mathcal{A}, \mathcal{S}, \mathrm{Pe}_T, \mathrm{Pe}_C.$$

The thermodynamic closure variables $\phi, \theta, \Theta_f, \Theta_m$ come from the Enthalpy method, and depend only on dimensionless enthalpy H, bulk composition Θ, and lithostatic pressure $G^{-1}z$. The Enthalpy method is given by the algebraic system

$$\phi = \begin{cases} 0 & \text{when } H \le \Theta - G^{-1}z \text{ (subsolidus),} \\ 1 & \text{when } H \ge \Theta - G^{-1}z + 1 + \mathcal{S} \text{ (superliquidus),} \\ \frac{H-\Theta+G^{-1}z}{1+\mathcal{S}} & \text{otherwise.} \end{cases} \tag{153a}$$

$$\tilde{\theta} = H - \phi\mathcal{S} \qquad \text{using the porosity from above,} \tag{153b}$$

$$\Theta_m = \Theta + \phi \qquad \text{solidus constraint,} \tag{153c}$$

$$\Theta_f = \mathcal{M}(\Theta + \phi) - 1 \qquad \text{liquidus constraint,} \tag{153d}$$

$$\theta = \mathrm{e}^{-\mathcal{A}z}(\tilde{\theta} + \theta^*) - \theta^* \quad \text{definition of potential temperature.} \tag{153e}$$

Here we have added the additional dimensionless numbers $\mathcal{M}$, θ^*, and G.

The viscosities are calculated with constitutive relations (in dimensional form)

$$\eta = \eta_0 \exp\left[\frac{E^*}{R}\left(\frac{1}{T} - \frac{1}{T_{\eta_0}}\right) - \lambda\phi\right], \tag{154a}$$

$$\zeta = \zeta_0\phi^{-1}\exp\left[\frac{E^*}{R}\left(\frac{1}{T} - \frac{1}{T_{\eta_0}}\right)\right], \tag{154b}$$

$$\xi = \zeta - 2\eta/3. \tag{154c}$$

Here both the bulk and shear viscosity obey an Arrhenius law in their dependence on temperature; A is an amplitude coefficient, E^* is an activation energy, R is the universal gas constant, T is temperature. λ is a porosity weakening coefficient. The ϕ^{-1} can be obtained through a variety of different lines of reasoning, none of which are explained here (but see references). Examination of these constitutive laws for viscosity indicates that both η and ζ decrease sharply with temperature, and both decrease with increasing porosity. When $\phi \approx 0.01$, we can see that $\zeta \gg \eta$.

9.1 Magma genesis and transport beneath mid-ocean ridges

We solve the assembled system of equations numerically, on a rectangular domain that is oriented vertically, perpendicular to the ridge axis. The domain can encompass both flanks of the ridge or, if we assume symmetry between the flanks, it can include just one of them. In this case, all variables have *reflection* boundary conditions (e.g. $\partial H/\partial x = 0$) on the left side of the domain, as indicated in Figure 22. On the top surface of the domain, we impose the plate spreading velocity $\mathbf{v}_m = U_0\hat{\mathbf{i}} + 0\hat{\mathbf{k}}$, with temperature $T = 0°\text{C}$. The right boundary is an outflow boundary, which uses a mixture of reflection and *dirichlet* conditions (e.g. $P = 0$). On the bottom boundary we impose zero shear stress, $\sigma_{xz} = \eta(\partial W/\partial x + \partial U/\partial z)$, and give inflowing mantle a chosen composition C_0 and mantle potential temperature $\mathcal{T}_0$. The temperature conditions are imposed by calculating the corresponding dimensionless bulk enthalpy H with $\phi = 1$.

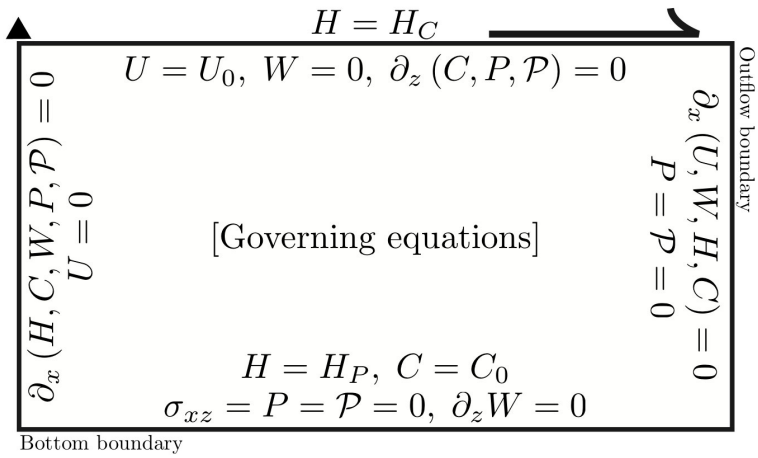

Figure 22: Schematic illustration of the computational domain for a half-ridge simulation. The ridge axis is above the top-left corner of the domain. The left boundary has reflection boundary conditions, based on the assumed symmetry across the ridge axis. The right boundary has outflow conditions, the bottom boundary has inflow conditions fixed mantle potential temperature. The top boundary has the imposed plate velocity and cold surface temperature. [Katz, 2008]

Figure 23 shows a representative example of a mid-ocean ridge simulation after 1 Ma of simulated time. The half-spreading rate, in this case, was $U_0 = 4$ cm per year, which is moderate to fast, in terms of the global range of spreading rates. The inverted white triangle on the top of each panel shows the distance the plate has moved since the beginning of the simulation. The simulation has reached an approximate steady state.

Panel (a) shows the temperature field in colour. Note the usual $t^{1/2}$ thickening of the thermal boundary layer as the plate moves away from the ridge axis. The white line is the outline of the partially molten region. Here the mantle is upwelling and above its pressure-dependent solidus temperature. As it upwells, it melts to progressively large degree. The black lines are contours of melt fraction $F = (C_m - C_0)/(C_m - C_f)$, going from 1% at the bottom of the melting region upward with an interval of 2.5%, up to around 23% melting at the top of the melting region, and spreading outward due to advection of the residue of melting by mantle flow.

Panel (b) show streamlines of the mantle flow, indicating upwelling beneath the ridge, that turns into lateral spreading with distance. The is a small downwelling component visible in

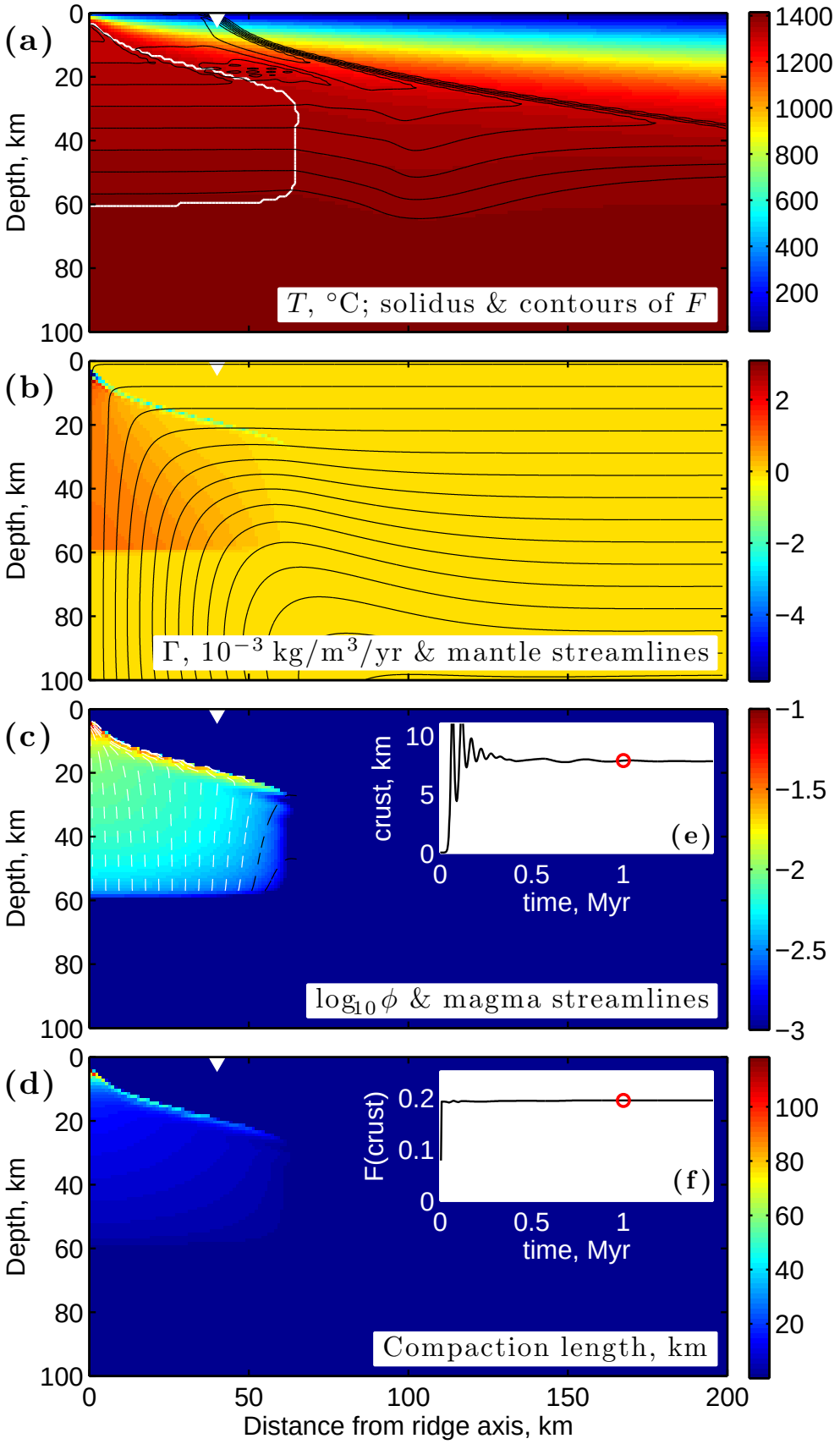

Figure 23: Output from a representative mid-ocean ridge simulation after 1 Ma. The half-spreading rate is 4 cm/yr, the permeability is given by $K = 10^{-7}\phi^3$, viscosity parameters are $\eta_0 = 10^{18}$, $\zeta_0 = 10^{19}$ Pa-sec, the potential temperature is 1375° C, and melting begins at about 60 km depth. Other parameter as in Table 1. The white triangle shows the spreading distance since $t = 0$. Panel contents as labeled; see main text for further details. Figure from Katz [2010].

the streamlines, making it different from the canonical corner-flow solution; this is due to the contribution of buoyancy forces ($\overline{\rho} g \hat{\mathbf{k}}$ in equation (20)) that drive convective upwelling within the melting region, and downwelling on its flank. This contribution is examined in more detail below. The upwelling drives melting, and colours in this panel show the melting rate, which is largest where upwelling is strongest. At the top of the melting region there is a strip of blue colours, indicating freezing of magma. This occurs as the rising magma interacts with the cold thermal boundary layer in the lithosphere. The freezing closes the pore-space and creates a *permeability barrier*.

Panel (c) shows the effect of this permeability barrier on the flow of magma. Dashed lines are magmatic streamlines. Magma rises vertically through the melting region under the force of buoyancy, through most of the melting region. Note that the viscous shear stresses that we considered in section 5 are ineffective at focusing the magma to the ridge axis because η is much smaller than 10^{21} Pa-sec. The streamlines are bent toward the ridge axis as they approach the permeability barrier. There, compaction stresses deflect the magma and cause it to rise "uphill" along the barrier, as hot air would rise along the underside of a sloped roof. The colours in this panel show the $\log_{10}$ of porosity. Dark blue represents porosities of $10^{-3} = 0.1\%$ or smaller. Dark red represents $\phi = 10^{-1}$ or 10% porosity. It is evident that the channel beneath the permeability barrier is high porosity. This is because it is being fed by the broad melting region below, and because the melt moving through is driven only by the component of gravity that is resolved onto the channel slope, which is relatively small. All of the white streamlines are focused to the ridge axis, while the black streamlines are not. This indicates that melt focusing along the permeability barrier may efficiently transport magma from far out on the flanks of the melting region; only the most distal melts are frozen back into the mantle.

Panel (d) shows the compaction length, as computed with dimensional variables, at each grid point in the domain, according to

$$\begin{aligned} \delta &= \sqrt{\frac{K(\zeta + 4\eta/3)}{\mu}}, \\ &\approx \left\{ \frac{\zeta_0 K_0 \phi^{n-1}}{\mu} \exp\left[\frac{E^*}{R} \left(\frac{1}{T} - \frac{1}{T_0} \right) \right] \right\}, \end{aligned} \tag{155}$$

when $\phi \ll 1$ and $\zeta_0 \gtrsim \eta_0$. Using $\phi \approx 0.01$, $T \approx T_0$, and $\zeta_0 = 10^{19}$ we find that $\delta \approx 10$ km. As the porosity increases with height through the melting region, the associated increase in permeability dominates over the decrease in bulk viscosity, and the compaction length increases.

Panels (e) and (f) show characteristics of the magma extracted from the domain through a "dike" beneath the ridge axis, as a function of simulated time. The crustal thickness is simply calculated as the volume-flux of magma through the sub-ridge dike, divided by the half-spreading rate. There is a transient phases at the beginning of the simulation, when the system "spins up" and adjusts to the initial condition. It then settles into a stable crustal thickness of about 7 km. This is consistent with mid-ocean ridges at this spreading rate (but the phase diagram and Clapeyron slope are calibrated to achieve this). The crustal degree of melting is computed using the aggregated melt composition as it enters the dike: $F_{\text{crust}} = (C_{\text{crust}} - C_0 + \Delta C)/\Delta C$. It reaches its steady value of ∼20% rapidly and remains there with time, showing little or no correlation with the fluctuations in crustal thickness.

The discussion above considered a "representative" simulation, but just how representative is it? How does the system behave under different parameter values, that are still within the limits of our uncertainty of their value within the Earth? The parameter space of the model is very large, but some simple and interesting behaviour can observed with a couple of key parameters. To explore the effects of these parameters, we simplify the above model by discarding the buoyancy term in the Stokes equation (152c). Mantle flows calculated without

this term are called "passive," while those calculated with buoyancy are called "active." The example in Figure 23 is an active flow.

Permeability The permeability law that is used in the current simulations contains two parameters, K_0 and n; here we consider the effect of K_0. K_0 is a scale factor that is proportional to the square of the grain size. Grain size is highly uncertain for the mantle, and hence we have rather broad bounds on K_0. One of them comes from seismic tomography (e.g. the MELT survey): we expect that the porosity in the mantle beneath ridges is of order 1%. Hence our choice of permeability should be roughly consistent with this estimate. Crustal thickness provides another bound: we know the approximate melt fraction and productivity beneath ridges; given this, too small a permeability would lead to crustal thickness that is smaller than expected. Figure 24 shows the effect of variations in permeability in panels (b), (c), and (d). Panel (b) examines the travel-time of magma to the ridge axis as a function of lateral distance, for different values of K_0; (c) plots the variation in porosity at 30 km depth as a function of K_0, and (d) illustrates the dependence of melt-focusing efficiency on K_0.

Bulk viscosity The bulk viscosity is very poorly constrained parameter that plays an important role in determining the style and efficiency of melt extraction. It sets the compaction length, and affects the way that melts interact with the cold thermal boundary layer above the melting region. In the simulations that are analysed in Figure 24, the bulk viscosity is given by the function $\zeta = \zeta_R \eta_0/\phi$, where ζ_R is the ratio of the reference bulk viscosity to the shear viscosity. Panel (a) compares two runs with different values of ζ_R that are otherwise identical, and shows that qualitatively, the bulk viscosity plays an important role is the deflection of magmatic streamlines to the ridge axis. When it is small, magma can modify the thermal structure of the lithosphere, and pool along the permeability barrier. This magma will eventually freeze into the lithosphere, leaving its trace in the fertility of the rock. Panel (c) shows that far from the permeability barrier, the bulk viscosity plays almost no role in determining the porosity. Panel (d) shows that the fraction of melt that arrives at the ridge axis is a strong function of the bulk viscosity, which can be understood in terms of the processes evident in the bottom part of (a).

9.2 Porosity-driven convection

In our exploration of the effect of varying permeability and bulk viscosity pre-factors, we considered only passive mantle flow, explicitly excluding the effects of buoyancy driven convection. We now return buoyancy to its rightful place, and consider the possibility that the porosity created by melting could drive convection beneath a mid-ocean ridge. Magma is less dense than the mantle, which is why it rises; a partially molten chunk of mantle should therefore be less dense than an unmolten one, all else (temperature, composition) being equal. We see this in the buoyancy term of dimensionless equation (152c), $\phi\hat{\mathbf{k}}$. Larger porosity means more buoyancy. We can generalise this by returning to the dimensional equation (20) and considering the body-force term, $-\overline{\rho} g \hat{\mathbf{k}}$. Expanding $\overline{\rho}$,

$$\begin{aligned} \overline{\rho} &= (1-\phi)\rho_m + \phi\rho_f, \\ &= (1-\phi)\rho_{m0}(1-B_m) + \phi\rho_{f0}(1-B_f), \end{aligned} \tag{156}$$

where ρ_{m0}, ρ_{f0} are reference densities, and B_m, B_f are buoyancy terms given by the linear density model of thermal and solutal expansion,

$$B_i = \alpha(T - T_0) + \beta(C_i - C_0), \tag{157}$$

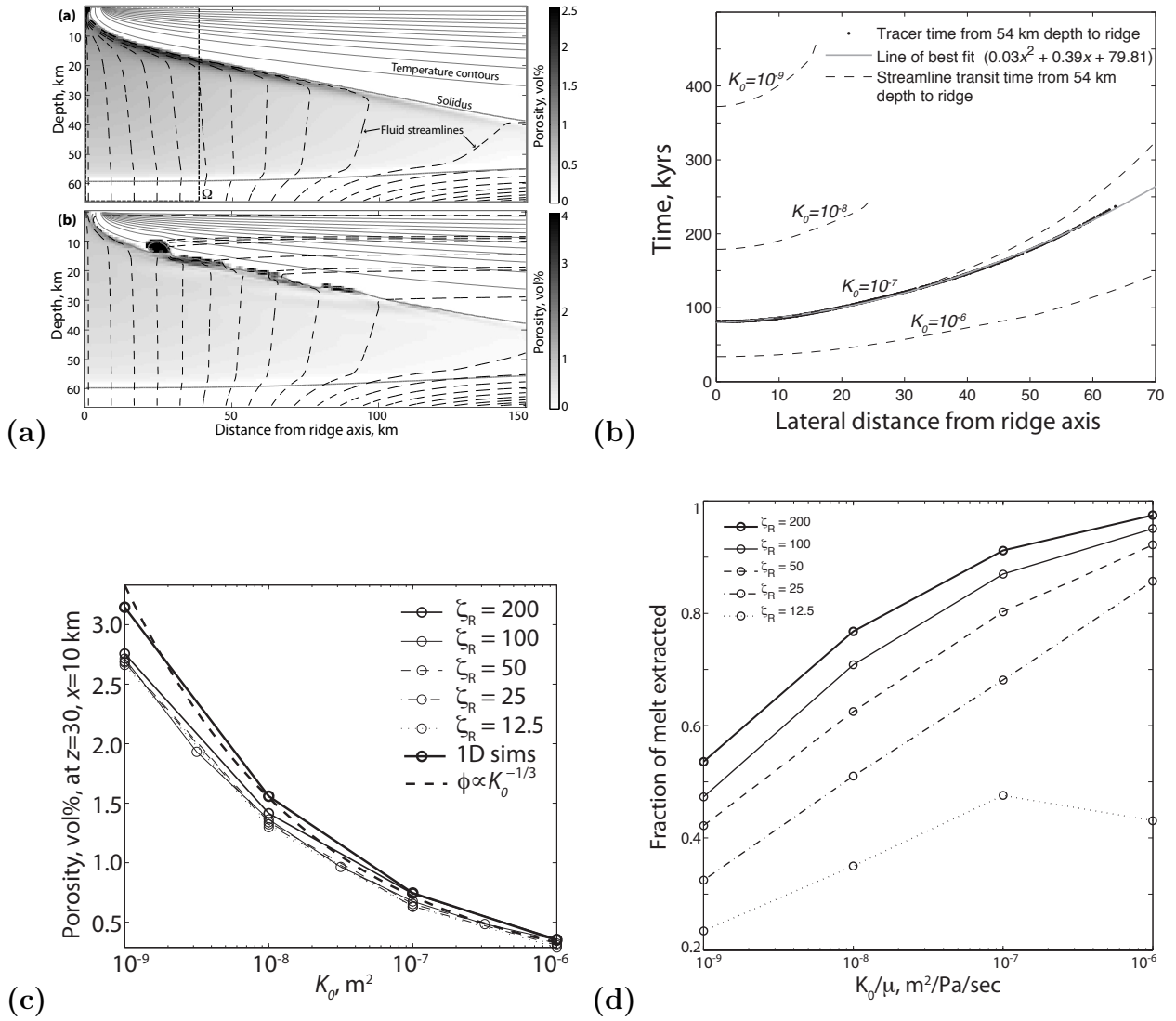

Figure 24: Figures showing the effect of varying the permeability and bulk viscosity pre-factors ($\zeta_R = \zeta_0/\eta_0$). **(a)** Steady state conditions for two simulations with $K_0 = 10^{-7}$ m^2 and different values of ζ_0. In the top panel, $\zeta_R = 100$, while in the bottom panel, $\zeta_R = 25$. The porosity scale is clipped; $\phi = 9\%$ within the pool of melt that has formed beneath the lithosphere. **(b)** Travel time of magma to the ridge axis from 54 km depth, as a function of the lateral distance from the ridge axis, from a simulation with $K_0 = 10^{-7}$ m^2 and $\zeta_R = 100$. Dashed lines are travel times along instantaneous streamlines, which should approximate the paths of magma parcels, if the solution is in steady state. **(c)** The porosity at 30 km depth in 1D column models, as a function of K_0, for different values of ζ_0. The heavy dashed curve is a theoretical prediction from equation (138). **(d)** The efficiency of focusing for a suite of 2D models with various K_0 and ζ_0. Efficiency is the fraction of melt extracted at the ridge axis divided by the fraction produced by melting. Each point is an average over time. Panels from Katz [2008]

where i can take values of m or f for the matrix or magma. Equation (157) states that both phases individually vary in density according to their temperature and composition relative to some reference value. Equation (156) states that these density variations combine in proportion to the phase fraction to give the bulk density. Various authors (see references) have considered the effect of thermal and compositional buoyancy; we leave those aside for the moment, take the phase densities to be constant ($B_i = 0$), and investigate the role of porosity acting on a constant density difference $\rho_m - \rho_f = \Delta\rho$.

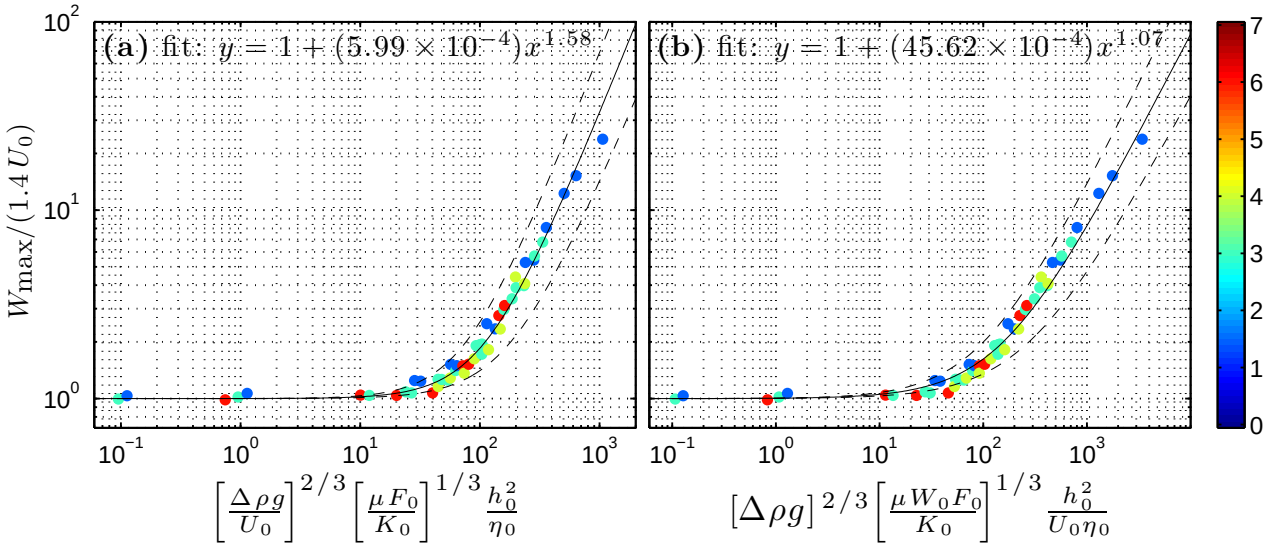

Figure 25: Convective vigour as a function of the vigour parameter(s). The y-axis represents the enhancement to upwelling caused by buoyancy. A value of $y = 1$ represents unenhanced, pure passive flow. Each point represents a single simulation that was run to steady-state. Point colour represents half-spreading rate. Lines are fit by finding the nonlinear least-square error over parameters a and b of $y = 1 + ax^b$. **(a)** Data plotted in terms of the approximated vigour parameter $\mathcal{V}_U$. The agreement between the fit and the data indicates that this approximation is valid over a broad range of $\mathcal{V}_U$, though it modifies the exponent b in the fit. **(b)** Data plotted in terms of the full vigour parameter $\mathcal{V}$. The upwelling rate W_0 has been obtained from the simulations themselves, after the fact. Figure from Katz [2010].

This assumption brings us back to the Stokes equation as written above in (24). Let's conceptually divide our domain into two regimes: the plate regime, where viscosity is high enough to suppress deformation; and the mantle regime, where viscosity is low enough to promote it. If we assume that the viscosity is approximately constant within the mantle regime, we can bring η outside of the divergence operator,

$$\boldsymbol{\nabla} P = \eta \nabla^2 \mathbf{v}_m - \phi \Delta\rho \hat{\mathbf{g}}.$$

Defining a mantle vorticity as $\omega\hat{\mathbf{j}} = \boldsymbol{\nabla} \times \mathbf{v}_m$ and taking the curl of this equation gives

$$\eta_0 \nabla^2 \omega = \Delta\rho g \frac{\partial \phi}{\partial x}, \tag{158}$$

which states that lateral gradients in porosity place a torque on the mantle and represent an internal source of vorticity (i.e. convection). There is an important external source of vorticity: the boundary condition of spreading plates. To determine the relative importance of these two effects, we can perform a scaling analysis on (158). First rescale variables with characteristic scales

$$[x] = h_0, \qquad [\phi] = \phi_0, \qquad [\omega] = U_0/h_0, \tag{159}$$

where h_0 is the height of the melting column. Substitution and reshuffling gives, in terms of dimensionless variables

$$\nabla^2\omega = \mathcal{V}\frac{\partial\phi}{\partial x}, \qquad \text{with} \qquad \mathcal{V} = \frac{\Delta\rho g\phi_0 h^2}{\eta_0 U_0}, \tag{160}$$

where $\mathcal{V}$, the *vigour* parameter, is a dimensionless number analogous to the Rayleigh number in thermal convection. We can use our solution for ϕ from the 1D column model (eqn. (138)) to obtain an estimate for ϕ_0 in terms of other parameters,

$$\phi(z) \approx \left[\frac{\mu W_0 F}{K_0\Delta\rho g}\right]^{1/n}. \tag{161}$$

Taking F_0 as some representative value of the degree of melting, and for $n = 3$, and substituting back into (160) gives

$$\mathcal{V} = [\Delta\rho g]^{2/3}\left[\frac{\mu W_0 F_0}{K_0}\right]^{1/3}\frac{h_0^2}{U_0\eta_0}. \tag{162}$$

Unfortunately, the upwelling rate at the base of the melting column W_0 is determined by the vigour of convection, and hence we don't know it *a priori*. We can estimate $W_0 \approx U_0$, which will only be true for moderate to small values of $\mathcal{V}$, but allows us to move forward. Doing so gives

$$\mathcal{V}_U = \left[\frac{\Delta\rho g}{U_0}\right]^{2/3}\left[\frac{\mu F_0}{K_0}\right]^{1/3}\frac{h_0^2}{\eta_0}. \tag{163}$$

This dimensionless number predicts how the relative importance of active upwelling scales with problem parameters. When $\mathcal{V} \ll 1$, we'd expect the mantle flow to be driven mostly by plate spreading, whereas when $\mathcal{V} \gg 1$, we'd expect a significant contribution from buoyancy. It is important to note that upwelling will occur regardless of the size of the vigour parameter, because it will be driven by the larger-scale convection of the mantle, which drives plate tectonics and hence the divergence of plates at a mid-ocean ridge.

The utility of the vigour parameter for describing the dynamics of simulations can be demonstrated without difficulty. A suite of simulations with values for U_0, η_0, K_0, and $\Delta\rho$ are summarised in Figure 25. They are plotted on the basis of their predicted vigor parameter ($\mathcal{V}_U$ in panel (a) and $\mathcal{V}$ in panel (b)) on the x-axis, and the enhancement to upwelling on the y-axis. The enhancement to upwelling is computed as the maximum upwelling rate in the domain (which is always found beneath the ridge axis), divided by the upwelling rate that would be expected for passive spreading (which is given by $1.4U_0$). Evidently, for small values of $\mathcal{V}, \mathcal{V}_U$, there is no enhancement by buoyancy, while for large values, buoyancy becomes increasingly important. In fact, the contribution of buoyancy scales almost linearly with $\mathcal{V}$, as shown by the fit in panel (b), which is given as $y = 1 + ax^b$, with a and b constants that are given in the figure caption.

What effect does active flow have on crustal production and melt fraction? An answer is given in Figure 26. Panel (a) plots crustal thickness as a function of half-spreading rate, compared with a global data set. The data show a sharp increase for small values of spreading rate, then a slight decline with spreading rate. The curves are simulation results, coloured by the viscosity pre-factor that was imposed. Since the vigor parameter depends on both η_0 and U_0, there are variations in the vigor of convection between and within these curves (the latter is shown in panel (c)). Larger viscosity leads to passive-like flow, and these curves are marked by a gradual increase with spreading rate, and no decrease. Conversely, for smaller values of η_0, we see a sharp increase that mirrors the data, then a gradual decrease that may also be consistent. The trend with spreading rate is more important than the absolute value of the

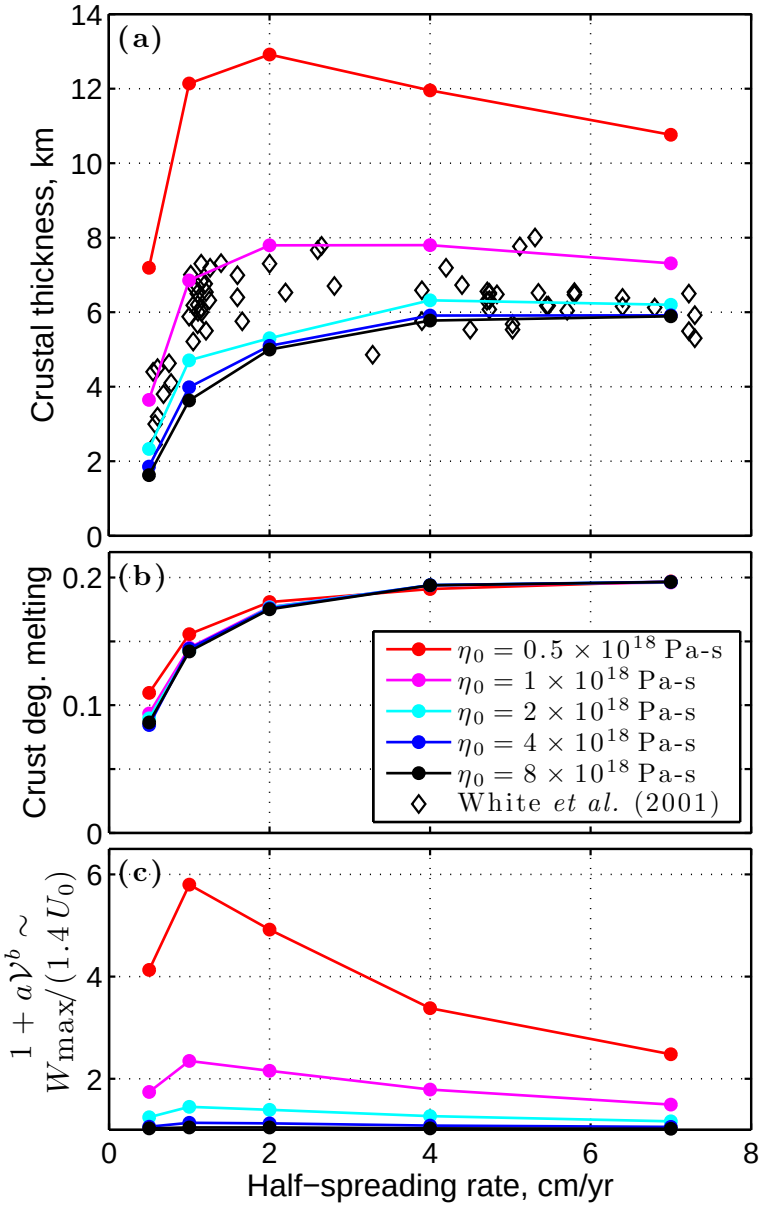

Figure 26: Output from ridge models that have reached steady state, as a function of the half-spreading rate and the viscosity pre-factor. **(a)** Crustal thickness predicted by a variety of model runs. The diamonds are observational data of the global ridge system, compiled by White et al. [2001]. **(b)** Crustal degree of melting, computed as $F_{\text{crust}} = (C_{\text{crust}} - C_0 + \Delta C)/\Delta C$. **(c)** The upwelling enhancement factor over passive flow. Figure from Katz [2010].

curves, as they can shift up and down depending on other uncertain parameters, such as the potential temperature and fertility of the mantle.

Panel (b) shows that although the volume of melt produced may change with the vigor of convection, the degree of melting remains nearly constant. This is because degree of melting is primarily sensitive, in this model, to the height of the melting column (see eqn. (136)), whereas the melting rate is sensitive to the mean upwelling rate (see eqn. (115)).

Panel (c) plots the enhancement of upwelling over passive flow. There is little or no enhancement when the viscosity is large (and the vigor parameter is small). At smaller viscosities, we see an increase in $W_{\max}/(1.4U_0)$ with spreading rate, then a gradual decrease. The decrease is unsurprising, given the way that U_0 enters into the expression for $\mathcal{V}$; the increase is due to an implicit effect: the height of the melting column h_0 depends strongly on U_0 for small spreading rates.

9.3 Reactive and mechanical instabilities in equilibrium ridge models?

We saw that reactive flow in disequilibrium models leads to channelised melt flow under some circumstances, and we saw geological evidence of channelised melt flow in the mantle, from the Oman ophiolite. The simulations in this section, however, haven't produced channels. Why not?

The reasons for this are only becoming clear now, but it appears that there is an important difference when models include conservation of energy. It turns out that channellisation is still possible, but it requires a melt-supply from below to become active. But if the bottom of the melting column is where melting begins, how could there be melting from below? Well, in a homogeneous mantle, there wouldn't be any melt introduced from below. But in a heterogeneous mantle, fertile blobs of recycled continental crust may upwell beneath ridges and hot-spots, and melt at much greater depths than the ambient mantle. So when the ambient mantle begins to melt, it could receive be fed from below by pulses of magma coming from highly molten fertile blobs. This would nucleate channels, as we shall see in the slides.

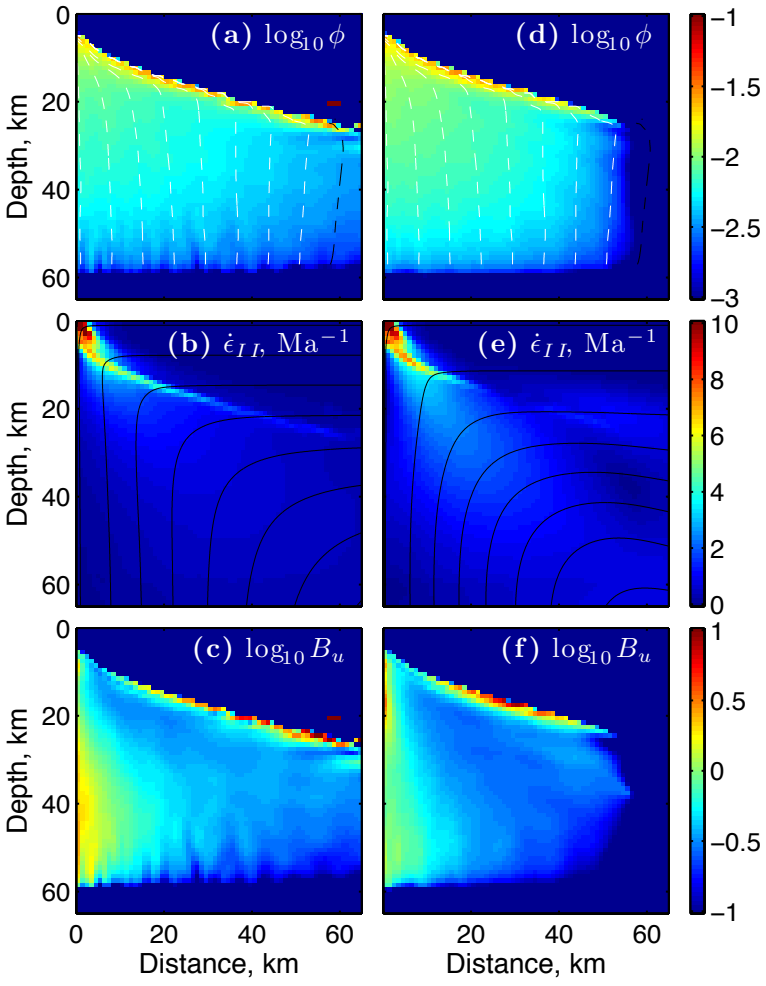

Figure 27: Two ridge simulations with ±0.6% white noise in the bulk composition field, $\lambda = 90$, and $\xi_0 = 10^{19}$ Pa-sec. The left column has $\eta_0 = 10^{19}$ Pa-sec ($\mathcal{V} = 10$) and the right column has $\eta_0 = 10^{18}$ Pa-sec ($\mathcal{V} = 96$). **(a) and (d)** show the log of porosity in colour and magmatic streamlines. **(b) and (e)** show the second invariant of the strain rate tensor $\dot{\epsilon}_{II}$ and the mantle streamlines. **(c) and (f)** show the log value of a dimensionless number that represents the ratio of buoyancy forces to compaction stresses, $B_u = \Delta\rho g\delta/[(\zeta + 4\eta/3)\dot{\gamma}]$. Figure from Katz [2010].

What about porosity bands caused by shearing of the mantle? Just because these form under the very high strain rates in the laboratory ($\sim 1 \times 10^{-4}$ sec^{-1}) doesn't necessarily mean that they will form under the lower strain rates in the mantle ($\sim 1 \times 10^{-14}$ sec^{-1}), where there are other forces at play. In the mantle, gravity (and buoyancy) is expected to dominate over other stresses in driving melt flow. Furthermore, the total strain accumulated by a parcel of mantle as it flows through a ridge system is of order 1, not clearly enough to produce banding. The ridge model shown above uses a shear-viscosity law that is porosity weakening (eqn. (154)),

and hence does not exclude the possibility of porosity band formation, yet bands do not appear in simulations with a homogeneous mantle.

To probe further, we can consider a slightly heterogeneous mantle, and exaggerate the sensitivity of viscosity to porosity by choosing $\lambda = 90$, a factor of three larger than empirical estimates. The results of two ridge models with these parameter are shown in Figure 27. Clearly no porosity bands have developed due to shear.

Further reading There isn't much of a literature on tectonic-scale solutions to the full, two-phase dynamics with energy. Recent work is limited to Ghods and Arkani-Hamed [2000], Katz [2008], and Katz [2010], though a related set of papers by Šrámek et al. [2010] and Ricard et al. [2009] on molten metal segregation from the mantle into the core are relevant. There is also Spiegelman [1996] and Spiegelman and Reynolds [1997], which examine ridge-scale convection driven by buoyancy, and the consequences for geochemical transport.

Other work on ridge-scale convection includes Buck and Su [1989], Scott and Stevenson [1989], Parmentier and Morgan [1990], Su and Buck [1993], Sparks and Parmentier [1993], Jha et al. [1994], Choblet and Parmentier [2001].

A very important paper on magmatic focusing through a sub-lithospheric channel beneath mid-ocean ridges is Sparks and Parmentier [1991]. An excellent discussion of channellisation in equilibrium and disequilibrium models is given by Hewitt [2010].

References

E. Aharonov, J. Whitehead, P. Kelemen, and M. Spiegelman. Channeling instability of upwelling melt in the mantle. *J. Geophys. Res.*, 100(B10):20433–20450, 1995.

E. Aharonov, M. Spiegelman, and P. Kelemen. Three-dimensional flow and reaction in porous media: implications for the earth's mantle and sedimentary basins. *J. Geophys. Res.*, 102 (B7):14821–14833, 1997.

J. Ahern and D. Turcotte. Magma migration beneath an ocean ridge. *Earth Plan. Sci. Lett.*, 45:115–122, 1979.

V. Barcilon and O. Lovera. Solitary waves in magma dynamics. *J. Fluid Mech.*, 204:121–133, 1989.

V. Barcilon and F. M. Richter. Non-linear waves in compacting media. *J. Fluid Mech.*, 164: 429–448, 1986.

D. Bercovici and Y. Ricard. Energetics of a two-phase model of lithospheric damage, shear localization and plate-boundary formation. *Geophysical Journal International*, 152(3):581–596, 2003.

D. Bercovici, Y. Ricard, and G. Schubert. A two-phase model for compaction and damage 1. general theory. *J. Geophys. Res.-Solid Earth*, 106(B5):8887–8906, 2001a.

D. Bercovici, Y. Ricard, and G. Schubert. A two-phase model for compaction and damage 3. applications to shear localization and plate boundary formation. *J. Geophys. Res.-Solid Earth*, 106(B5):8925–8939, 2001b.

M. Braun and P. Kelemen. Dunite distribution in the Oman ophiolite: Implications for melt flux through porous dunite conduits. *Geochem. Geophys. Geosys.*, 3(8603), 2002.

W. Buck and W. Su. Focused mantle upwelling below mid-ocean ridges due to feedback between viscosity and melting. *Geophys. Res. Letts.*, 16(7):641–644, 1989.

S. Butler. The effects of buoyancy on shear-induced melt bands in a compacting porous medium. *Phys. Earth Planet. In.*, 173(1-2):51–59, 2009. doi: 10.1016/j.pepi.2008.10.022.

S. L. Butler. Porosity localizing instability in a compacting porous layer in a pure shear flow and the evolution of porosity band wavelength. *Phys. Earth Planet. In.*, 182:30–41, 2010. doi: 10.1016/j.pepi.2010.06.004.

G. Choblet and E. M. Parmentier. Mantle upwelling and melting beneath slow spreading centers: effects of variable rheology and melt productivity. *Earth Plan. Sci. Lett.*, 184: 589–604, jan 2001.

T. Elliott and M. Spiegelman. Melt migration in oceanic crustal production: A U-series perspective. In R. Rudnick, editor, *The Crust*, volume 3 of *Treatise on Geochemistry*. Elsevier, 2003.

A. Fowler. A mathematical model of magma transport in the asthenosphere. *Geophys. Astrophys. Fluid Dyn.*, 33:63–96, 1985.

A. Ghods and J. Arkani-Hamed. Melt migration beneath mid-ocean ridges. *Geophys. J. Int.*, 140(3):687–697, 2000.

C. Hall and E. Parmentier. Spontaneous melt localization in a deforming solid with viscosity variations due to water weakening. *Geophys. Res. Letts.*, 27(1):9–12, 2000.

I. Hewitt. Modelling melting rates in upwelling mantle. *Earth Plan. Sci. Lett.*, 300:264–274, 2010. doi: 10.1016/j.epsl.2010.10.010.

I. Hewitt and A. Fowler. Partial melting in an upwelling mantle column. *Phil. Trans. R. Soc. London A*, 2008. doi: doi:10.1098/rspa.2008.0045.

S. Hier-Majumder, Y. Ricard, and D. Bercovici. Role of grain boundaries in magma migration and storage. *Earth Plan. Sci. Lett.*, 248:735–749, 2006. doi: 10.1016/j.epsl.2006.06.015.

B. Holtzman, N. Groebner, M. Zimmerman, S. Ginsberg, and D. Kohlstedt. Stress-driven melt segregation in partially molten rocks. *Geochem. Geophys. Geosyst.*, 4, 2003. Art. No. 8607.

K. Jha, E. Parmentier, and J. Phipps Morgan. The role of mantle-depletion and melt-retention buoyancy in spreading-center segmentation. *Earth Plan. Sci. Lett.*, 125:221–234, 1994.

M. Jull, P. Kelemen, and K. Sims. Consequences of diffuse and channelled porous melt migration on Uranium series disequilibria. *Geochim. Cosmochim. Acta*, 66(23):4133–4148, 2002.

R. Katz. Magma dynamics with the enthalpy method: Benchmark solutions and magmatic focusing at mid-ocean ridges. *J. Petrology*, 49:2099–2121, 2008. doi: 10.1093/petrology/egn058.

R. Katz, M. Spiegelman, and B. Holtzman. The dynamics of melt and shear localization in partially molten aggregates. *Nature*, 442(7103), 2006.

R. Katz, M. Knepley, B. Smith, M. Spiegelman, and E. Coon. Numerical simulation of geodynamic processes with the Portable Extensible Toolkit for Scientific Computation. *Phys. Earth Planet. In.*, 163:52–68, 2007. doi: 10.1016/j.pepi.2007.04.016.

R. F. Katz. Porosity-driven convection and asymmetry beneath mid-ocean ridges. *Geochem. Geophys. Geosys.*, 11, 2010. doi: 10.1029/2010GC003282.

P. Kelemen, H. Dick, and J. Quick. Formation of harzburgite by pervasive melt rock reaction in the upper mantle. *Nature*, 358(6388):635–641, 1992.

P. Kelemen, N. Shimizu, and V. Salters. Extraction of mid-ocean-ridge basalt from the upwelling mantle by focused flow of melt in dunite channels. *Nature*, 375(6534):747–753, 1995a.

P. Kelemen, J. Whitehead, E. Aharonov, and K. Jordahl. Experiments on flow focusing in soluble porous-media, with applications to melt extraction from the mantle. *J. Geophys. Res.*, 100(B1):475–496, 1995b.

D. King, M. E. Zimmerman, and D. L. Kohlstedt. Stress-driven Melt Segregation in Partially Molten Olivine-rich Rocks Deformed in Torsion. *Journal Of Petrology*, 51(1-2):21, 2010. doi: 10.1093/petrology/egp062.

D. L. Kohlstedt and B. K. Holtzman. Shearing Melt Out of the Earth: An Experimentalist's Perspective on the Influence of Deformation on Melt Extraction. *Ann. Rev. Earth Plan. Sci.*, 37:561–593, 2009. doi: 10.1146/annurev.earth.031208.100104.

Y. Liang and E. M. Parmentier. A Two-Porosity Double Lithology Model for Partial Melting, Melt Transport and Melt-rock Reaction in the Mantle: Mass Conservation Equations and Trace Element Transport. *Journal Of Petrology*, 51(1-2):125, 2010. doi: 10.1093/petrology/egp086.

Y. Liang, A. Schiemenz, M. A. Hesse, E. M. Parmentier, and J. S. Hesthaven. High-porosity channels for melt migration in the mantle: Top is the dunite and bottom is the harzburgite and lherzolite. *Geophysical Research Letters*, 37(15):L15306, 2010. doi: 10.1029/2010GL044162.

D. McKenzie. The generation and compaction of partially molten rock. *J. Petrol.*, 25(3): 713–765, 1984.

Z. Morgan and Y. Liang. An experimental and numerical study of the kinetics of harzburgite reactive dissolution with applications to dunite dike formation. *Earth Plan. Sci. Lett.*, 214 (1-2):59–74, 2003. doi: 10.1016/S0012-821X(03)00375-3.

Z. Morgan and Y. Liang. An experimental study of the kinetics of lherzolite reactive dissolution with applications to melt channel formation. *Contrib. Mineral. Petrol.*, 150(4):369–385, 2005.

E. M. Parmentier and J. Morgan. Spreading rate dependence of 3-dimensional structure in oceanic spreading centers. *Nature*, 348(6299):325–328, 1990.

J. Phipps Morgan. Melt migration beneath mid-ocean spreading centers. *Geophys. Res. Letts.*, 14(12):1238–1241, 1987.

N. Ribe. The generation and composition of partial melts in the earth's mantle. *Earth Planet Sc Lett*, 73:361–376, 1985a.

N. Ribe. The deformation and compaction of partial molten zones. *Geophys J Roy Astr S*, 83: 487–501, Jan 1985b.

Y. Ricard, D. Bercovici, and G. Schubert. A two-phase model for compaction and damage 2. Applications to compaction, deformation, and the role of interfacial surface tension. *Journal Of Geophysical Research*, 106:8907–8924, 2001.

Y. Ricard, O. Šrámek, and F. Dubuffet. A multi-phase model of runaway core–mantle segregation in planetary embryos. *Earth Plan. Sci. Lett.*, 284(1-2):144–150, 2009. doi: 10.1016/j.epsl.2009.04.021.

C. Richardson. Melt flow in a variable viscosity matrix. *Geophys. Res. Letts.*, 25(7):1099–1102, 1998.

F. M. Richter, F. M. Richter, and D. Mckenzie. Dynamical Models for Melt Segregation from a Deformable Matrix. *Journal of Geology*, 92:729–740, 1984.

G. N. Riley and D. L. Kohlstedt. Kinetics of Melt Migration in Upper Mantle-Type Rocks. *Earth And Planetary Science Letters*, 105:500–521, 1991.

D. Scott and D. Stevenson. Magma solitons. *Geophys. Res. Letts.*, 11:1161–1164, 1984.

D. Scott and D. Stevenson. Magma ascent by porous flow. *J. Geophys. Res.*, 91:9283–9296, 1986.

D. Scott and D. J. Stevenson. A self-consistent model of melting, magma migration and buoyancy-driven circulation beneath mid-ocean ridges. *J. Geophys. Res.*, 94:2973–2988, 1989.

G. Simpson, M. Spiegelman, and M. I. Weinstein. Degenerate dispersive equations arising in the study of magma dynamics. *Nonlinearity*, 20:21–49, 2007. doi: 10.1088/0951-7715/20/1/003.

G. Simpson, M. Spiegelman, and M. Weinstein. A multiscale model of partial melts: 1. Effective equations. *Journal Of Geophysical Research*, 115, 2010. doi: 10.1029/2009JB006375.

D. Sparks and E. Parmentier. Melt extraction from the mantle beneath spreading centers. *Earth Plan. Sci. Lett.*, 105(4):368–377, 1991.

D. Sparks and E. M. Parmentier. The structure of 3-dimensional convection beneath oceanic spreading centers. *Geophys. J. Int.*, 112(1):81–91, 1993.

M. Spiegelman. Linear analysis of melt band formation by simple shear. *Geochem. Geophys. Geosys.*, 4(9), 2003. article 8615, doi:10.1029/2002GC000499.

M. Spiegelman. Flow in deformable porous-media. part 1. Simple analysis. *J. Fluid Mech.*, 247: 17–38, 1993a.

M. Spiegelman. Flow in deformable porous media. part 2. Numerical analysis—The relationship between shock waves and solitary waves. *J. Fluid Mech.*, 247:39–63, 1993b.

M. Spiegelman. Geochemical consequences of melt transport in 2-d: The sensitivity of trace elements to mantle dynamics. *Earth Planet Sc Lett*, 139:115–132, 1996.

M. Spiegelman and P. Kelemen. Extreme chemical variability as a consequence of channelized melt transport. *Geochem. Geophys. Geosys.*, 4, 2003.

M. Spiegelman and D. McKenzie. Simple 2-D models for melt extraction at mid-ocean ridges and island arcs. *Earth Plan. Sci. Lett.*, 83:137–152, 1987.

M. Spiegelman and J. Reynolds. Geochemistry in motion: Combined theoretical and observational evidence for convergent melt flow beneath the EPR. *Nature*, 402:282–285, 1997.

M. Spiegelman, P. Kelemen, and E. Aharonov. Causes and consequences of flow organization during melt transport: the reaction infiltration instability in compactible media. *J. Geophys. Res.*, 106(B2):2061–2077, 2001.

O. Sramek, Y. Ricard, and D. Bercovici. Simultaneous melting and compaction in deformable two-phase media. *Geophysical Journal International*, 168:964–982, 2007. doi: 10.1111/j.1365-246X.2006.03269.x.

O. Šrámek, Y. Ricard, and F. Dubuffet. A multiphase model of core formation. *Geophys. J. Int.*, 181(1):198–220, 2010. doi: 10.1111/j.1365-246X.2010.04528.x.

D. Stevenson. Spontaneous small-scale melt segregation in partial melts undergoing deformation. *Geophys. Res. Letts.*, 16(9):1067–1070, 1989.

D. Stevenson and D. Scott. Mechanics of fluid-rock systems. *Annu Rev Fluid Mech*, 23:305–339, 1991.

W. Su and W. Buck. Buoyancy effects on mantle flow under midocean ridges. *J. Geophys. Res.*, 98(B7):12191–12205, 1993.

Y. Takei and S. Hier-Majumder. A generalized formulation of interfacial tension driven fluid migration with dissolution/precipitation. *Earth Plan. Sci. Lett.*, 288:138–148, 2009. doi: 10.1016/j.epsl.2009.09.016.

D. L. Turcotte and J. L. Ahern. A Porous Flow Model for Magma Migration in the Asthenosphere. *Journal Of Geophysical Research*, 83(B2):767–772, 1978. doi: 10.1029/JB083iB02p00767.

R. White, T. Minshull, M. Bickle, and C. Robinson. Melt generation at very slow-spreading oceanic ridges: Constraints from geochemical and geophysical data. *J. Petrol.*, 42(6):1171–1196, 2001.

C. Wiggins and M. Spiegelman. Magma migration and magmatic solitary waves in 3-D. *Geophys. Res. Letts.*, 22(10):1289–1292, May 15 1995.